August 2022

Developing and Investigating a Fast and Controllable Prelithiation Method for Lithium-Ion Batteries

Huainan Qu
University of Wisconsin-Milwaukee

DEVELOPING AND INVESTIGATING A FAST AND CONTROLLABLE PRELITHIATION METHOD FOR LITHIUM-ION BATTERIES

by

Huainan Qu

A Dissertation Submitted in

Partial Fulfillment of the

Requirements for the Degree of

Doctor of Philosophy

in Engineering

at

The University of Wisconsin-Milwaukee

August 2022

ABSTRACT

DEVELOPING AND INVESTIGATING A FAST AND CONTROLLABLE PRELITHIATION METHOD FOR LITHIUM-ION BATTERIES

by

Huainan Qu

The University of Wisconsin-Milwaukee, 2022
Under the Supervision of Professor Deyang Qu

Prelithiation is to pre-load Li ions in a Li-ion electrode prior to a formation cycle. A chemical, roll-to-roll prelithiation method was developed in this thesis research. The method can be applied to different anode materials. The prelithiation compensated the initial loss of lithium during the formation cycles of a lithium-ion battery (LIB). Eventually, the initial coulombic efficiency (ICE) was significantly increased. In addition, the cyclability of a prelithiated battery was highly related to the quality of the solid electrolyte interface (SEI) on the anode surface. Electrochemical impedance spectroscopy (EIS) was a major technique to evaluate the difference of the SEI between a chemical lithiation and an electrochemical lithiation. An EIS analysis method was developed where the EIS data were transformed from a frequency domain into a time domain to identify the kinetics of each electrochemical process. An equivalent circuit to simulate the behavior of a battery is then created. By combining the simulation results and the cycling performance, a solid electrolyte interface was investigated quantitatively.

To

my family

TABLE OF CONTENTS

LIST OF FIGURES

LIST OF TABLES

LIST OF ABBREVIATIONS

LIB	Lithium-ion battery
ICE	Initial coulombic efficiency
SEI	Solid electrolyte interface
EIS	Electrochemical impedance spectroscopy
EV	Electric vehicles
NMC	Lithium nickel manganese cobalt oxide
HC	Hard carbon
EC	Ethylene carbonate
PC	Propylene carbonate
DEC	Diethylcarbonate
EMC	Ethylmethyl carbonate
DMC	Dimethyl carbonate
DOE	Design of experiments
VC	Vinylene carbonate
FEC	Fluoroethylene carbonate
LiBOB	Lithium bis(oxalate)borate
XPS	X-ray photoelectron spectroscopy
PES	Photoelectron spectroscopy
XRD	X-ray diffraction
CPE	Constant phase element

RC	Resistance and capacitor
DRT	Distribution of relaxation times
SOC	State of charge
SD	Standard deviations
FWHM	Full width at half maximum
CV	Cyclic voltammetry
Bp	Biphenyl
THF	Tetrahydrofuran
SEM	Scanning electron microscope
ICP-OES	Inductively coupled plasma-atomic emission spectrophotometry
NMP	*n*-methyl-2-pyrrolidone
PVDF	Poly(vinyl difluoride)
OD	Outer diameter
OCV	Open circuit voltage
Flr	9,9-dimethyl-9H-fluorene
Nap	Naphthalene
OCP	Open circuit potential
CE	Coulombic efficiency

ACKNOWLEDGEMENTS

Many people have helped me throughout my graduate study and all of them deserve my gratitude. Specifically, I would like to thank my supervisor and thesis advisor Professor Dr. Deyang Qu for providing the research ideas and guidance. When I was stuck in the middle of the project, he was always there instructing me with his wealth of knowledge and guiding me towards a solution. I would also like to thank Dr. Dong Zheng, Dr. Janak Kafle, Dr. Xiaoxiao Zhang and Dr. Weixiao Ji. They assisted me with using equipment, fabricating cells and making chemicals at the beginning of my project. Also, during my experiments, they always provided me guidance on both the operation and the principle, which allowed my project to move forward smoothly.

I wish to thank my thesis defense committee members, Prof. Ilya Avdeev, Prof. Prasenjit Guptasarma, Prof. Yin Wang and Prof. Yongjin Sung, for their suggestions on my thesis and future works.

I would like to thank the members of my research group, Alex Stephan, Caleb Abegglen, Dantong Qiu, Miao Liu, Suthan Prakashah and Tianyao Ding, for their help with my experiments and thesis. Without their support, I could hardly finish this project.

Last but not least, I wish to thank my family for their love and support throughout my education.

CHAPTER 1. BACKGROUND INTRODUCTION

1.1. Battery

A battery is an energy storage device that provides electric energy from chemical energy. Such energy conversion is driven by redox reactions within the battery. Unlike an internal combustion engine, a redox reaction in a battery is not governed by Carnot efficiency, so a battery converts the energy with much higher efficiency than an internal combustion engine.

The concept of a battery dated to the early 19th century when Italian physician Alessandro Volta obtained steady current by sandwiching a brine-soaked paper between a copper plate and a zinc plate. The pheromone was not immediate understood. The mechanism of the battery was gradually revealed that an electricity can only be produced when an oxidation and a reduction occur separately, which are connected both electrically and ionically. In a battery, a close circuit was generated with electrons moving through the external circuit and ions transporting through the internal electrolyte.

Many combinations of elements and their compounds may form a battery, but only limited materials are commercialized since an accessibility, safety, cost etc. need to be taken into consideration. Table 1-1 lists the typical batteries and their chemistries.

Batteries can be divided into two categories, primary and secondary batteries. In Table 1-1, an alkaline Zn-MnO_2 battery is a typical primary battery which is still powering various device nowadays for examples radio, toys, clocks. However, considering an increasing energy requirement and the needs for rechargeability of the emerging electronic devices and the electric machines, such as the electric vehicles, the primary battery can hardly fulfill all

the needs. Therefore, it boosts the development of secondary batteries and there is a trend that the secondary battery is taking care of most battery applications.

Table 1-1. Summary of different batteries [1].

Type	Anode reaction	Cathode reaction	Advantage	Disadvantage
Alkaline $Zn\text{-}MnO_2$	$Zn + 2OH^- = Zn(OH)_2 + 2e^-$	$MnO_2 + H_2O + 2e^- = MnOOH + OH^-$	Low cost	Low energy density
Lead acid	$Pb = Pb^{2+} + 2e^-$	$PbO_2 + 4H^+ + SO_4^{2-} + 2e^- = PbSO_4 + 2H_2O$	Low cost High-rate performance Wide temperature performance	Low cycle life Low energy density Large size
Nickel cadmium	$Cd + 2OH^- = Cd(OH)_2 + 2e^-$	$NiOOH + H_2O + e^- = Ni(OH)_2 + OH^-$	Long cycle life Low temperature performance Rapid charge capacity	Poor charge retention Low capacity Cadmium issue
Nickel metal hydride	$MH + OH^- = M + H_2O + e^-$	$NiOOH + H_2O + e^- = Ni(OH)_2 + OH^-$	High capacity Rapid charge capacity Long cycle life	High cost Poor charge retention Memory effect
Lithium ion	$Li_xC = C + xLi^+ + xe^-$	$Li_{1-x}MO_2 + xLi^+ + xe^- = LiMO_2$	Long cycle life Rapid charge capacity High power density High energy density	Failure at low temperature

1.2. Lithium-ion battery

Among the secondary batteries, a Lithium-ion battery (LIB) is currently the state-of-art energy storage device that supplies energy and power for various kinds of electronic devices and electric vehicles (EV) due to its high energy density and long cycle life. A report shows a possible growth of EV sales can be from 2% of global share in 2016 to 30% by 2030 [2]. It indicates that LIBs are most likely to benefit from this potential market thanks to the demonstration of its high performance in the current EV applications. The outstanding performance of the LIB can be evidenced from the Figure 1-1.

As shown in Figure 1-1, a comparison of power density and energy density shows that the LIB owns both a high specific power and a competitive specific energy among the available energy storage devices, especially overtakes the lead-acid battery and nickel–cadmium (NiCd) battery.

Although the first commercial LIB was released to public by Sony in 1991 [4], the revolutionary research of LIB dates to 1979 when the concept of lithium intercalation into a graphite was firstly demonstrated by Samar Basu [5]. Later in 1980, lithium cobalt dioxide ($LiCoO_2$) was used as the cathode in rechargeable lithium batteries by Ned A. Godshall at Stanford University [6]. According to their structural studies, the retention of the layered structure in $LiCoO_2$ was shown during the lithium extracting and intercalation, which marked a complete intercalation model for an LIB.

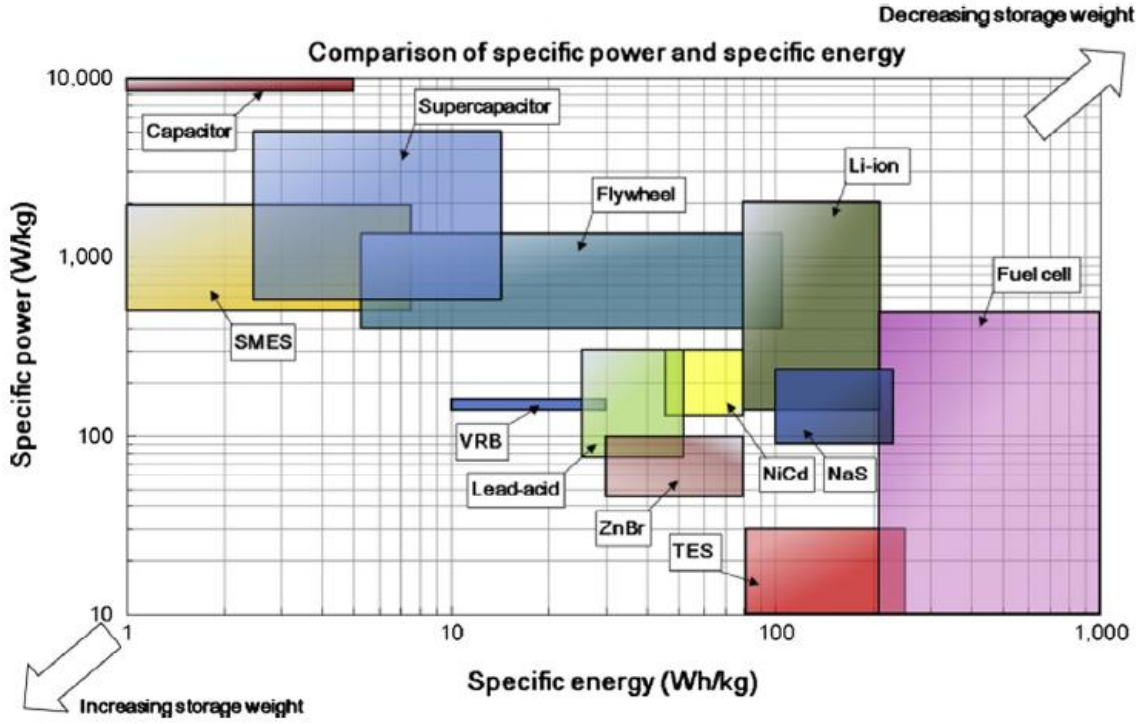

Figure 1-1. Comparison of specific power and specific energy of different energy devices [3].

1.2.1. Electrodes

A battery consists of an anode, a cathode and electrolyte. In a LIB, the cathode is the source of lithium. As a consequence, the overall capacity of a LIB is dependent on the maximum lithium loading of the cathode. During the development of the LIB, various cathode materials were commercialized and applied. Some typical ones are tabulated in Table 1-2.

As the earliest commercialized cathode material, LCO presents a moderately high energy density. However, because of the low thermal stability of the cobalt oxide, the LCO battery found a potential safety issue, which limited its application. LMO cathode was developed to solve the thermal runaway issue, while the specific energy was compromised. In order to extend the cycle life of the LIBs adapting to the EV applications, LFP was developed, nevertheless, it has a relatively low specific energy. Recently, a NCA cathode and a NMC cathode were developing. They balanced the cycle life and the energy density and became the first consideration in EV [7].

An anode in a LIB sinks the lithium during charging. Besides the capacity of the anode, its cycling stability is also a critical property which affects the lifetime of the battery. Other than a graphite anode, some other materials, such as carbon-based materials, silicon-based materials and metal oxides, were investigated as anode materials. Typical materials are tabulated in Table 1-3.

Table 1-2. Comparison of different cathodes of LIB [7].

Cathode material	Specific energy (Wh/kg)	Cycle life
$LiCoO_2$ (LCO)	150~190	500~1000
$LiMn_2O_4$ (LMO)	100~140	1000~1500
$LiFePO_4$ (LFP)	90~140	~2000
$LiNiCoAlO_2$ (NCA)	200~250	1000~1500
$LiNiMnCoO_2$ (NMC)	140~200	1000~2000

Table 1-3. Comparison of different anodes of LIB.

Anode material	Theoretical capacity/Empirical capacity (mAh/g)
Graphite	372
Hard Carbon (HC)	400~1000 [8]
Silicon (Si)	4200 [9]
Silicon monoxide (SiO)	1000~1400 [10], [11]
Tin Dioxide (SnO_2)	782~1494 [12], [13]

Graphite has been the state-of-art LIB anode material, owing to its technical mutuality and cycling stability. However, the limited capacity and low performance at a high rate of the graphite urge an alternative anode material. Hard carbon (HC), known as a non-graphitized carbon, provides a higher specific capacity and a higher rate capability than graphite [14]. However, the low ICE of the hard carbon results of a sever capacity loss during the first couples of cycles. A silicon has also been studied as the anode material for a LIB due to its high theoretical capacity based on the fully lithiated silicon, $Li_{4.4}Si$. However, it was found that the high lithiation capacity of the silicon led to a huge volume expansion. Therefore, other than the low ICE, which is in the range of 65%~85% [9], the degradation of the cell develops rapidly. SiO anode is an option that dramatically improves the cycling performance with a compromise of lithiation capacity. Although the volume change is marginally alleviated in the SiO anode, the ICE is lower than a Si due to the irreversible formation of the Li_4SiO_4 and Li_2O. Lithium alloys were also studied as potential anode materials. SnO_2 is an example, due to its high capacity and low cost. The total anode reaction involves two steps,

$$SnO_2 + 4Li^+ + 4e^- = Sn + 2Li_2O$$

$$Sn + 4.4Li^+ + 4.4e^- = Li_{4.4}Sn$$

The first conversion reaction is mostly irreversible. Therefore, the active Lithium from a cathode will be permanently consumed by forming non-rechargeable Li_2O during formation cycles. The irreversible capacity is 712 mAh/g. The reversible capacity (782 mAh/g) is from the second reaction. The theoretical ICE is a little higher than 50% [13].

1.2.2. Electrolyte system

An electrolyte serves as the medium for a charge transfer. It can be either at a solid state or at a liquid state. There is an increasing research and development on solid state electrolyte due to its high safety. However, considering the ionic conductivity, liquid electrolytes are still the first choice for a current commercial LIBs [15].

Lithium Salt

In a liquid electrolyte, a lithium salt provides the ions required for the transfer of charge between an anode and a cathode. Since a lithium ion has a small ionic radius, simple salts, such as LiCl, LiF, are not sufficiently soluble in a low dielectric media [16]. There is a limited selection of lithium salts that meet the minimum solubility requirement. The adequate lithium salts are usually with complexed anions, such as lithium bis(trifluoromethanesulfonyl)imide (LiIm), lithium trifluoromethanesulfonate (LiTf), and lithium hexafluorophosphate ($LiPF_6$) [17], [18]. It has been found that LiIm and LiTf have a higher dissociation constant and higher chemical stability than $LiPF_6$. However, considering the corrosion of current collectors and cell cases caused by the LiIm and LiTf [19], the $LiPF_6$ is a relatively ideal option after balanced all properties.

Solvent

A non-aqueous solvent must be used as a solvent in an LIB, since water reacts both lithium anode and many high potential cathodes e.g., NMC 811. In order to dissolve sufficient amounts of lithium salt and meet the concentration requirement, the solvent molecule must have high dielectric constant or be a polar molecular. Therefore, organic

solvents with carbonyl groups were often used [15]. A typical organic solvent involves some cyclic carbonates such as ethylene carbonate (EC), and propylene carbonate (PC), and some linear carbonates including diethylcarbonate (DEC), ethylmethyl carbonate (EMC), dimethyl carbonate (DMC) and so forth.

However, a solvent with a high dielectric constant has a high freezing point, for example, the EC's freeing point is 36.4ºC. A LIB using only high dielectric constant solvent would perform well at higher temperature but cease working a low or even room temperature due to the freezing solvent. In a practical lithium-ion battery, a dual- or tri-solvent electrolyte is always used to balance the salt dissolution and low temperature performance. The multiple solvent was investigated by Scrosati et al in 1970 when they mixed EC with 9% PC to lower the melting point of the solvent [20]. Dahn et al investigated the critical contribution of the EC on the SEI formation during lithium-ion intercalation into a graphite anode [21]. EC then became a major component of LIB electrolyte. Meanwhile, linear carbonates were brought into attentions. A formulation with EC and DMC mixed was proposed as high stability solvent [22]. Later, other linear carbonates were applied as co-solvents in the EC based electrolytes, such as DEC, and EMC [23], [24]. The previous work in our group was focused on multi-solvent electrolytes [25]. A high throughput statistical method was develop based on the design-of-experiment (DOE). EC, PC, EMC, DMC and DEC were mixed and test in various ratios using the statistical tool. The wide temperature cycling performance was tested. The best combination found through this high throughput screening was three times better at low temperature than the state-of-the-art electrolyte containing only EC and EMC.

Additives

Along with the engineering design and optimization of solvent combination, the performance of a LIB can be further improved by the introduction of sacrificial additives [26].

The additives generally get reduced (scarified or consumed) on an anode surface during formation cycles forming a stable protection layer, known as SEI, to prevent the reduction of the electrolyte. Such additives include vinylene carbonate (VC). A systematic study of VC was conducted by Xiong et al [27]. It was found that 1% VC contributes positively to the SEI formation without creating any significant negative impacts.

Fluoroethylene carbonate (FEC) is another additive proven to contribute a strong protective SEI on the anode surface in an LIB. Choi et al demonstrated a protection layer was formed on the graphite anode when 5% FEC added in the electrolyte, owning to the formation of a layer to the lower unoccupied molecular orbital energy of FEC, which sacrificed before the solvent molecules during the charging [28]. Not only on a graphite anode, Nakai et al found that FEC provided similar protection on a silicon anode of a LIB [29].

Lithium bis(oxalate)borate (LiBOB) has also been studied to improve the cycle life of a LIB at a high temperature [30]. It was found that LiBOB can prevent the exfoliation of a graphite anode when a PC based electrolyte was used [31]. Xu et al observed that the BOB anions decomposed on the graphite anode, which indicated that it might enhance the stability of the SEI [32].

1.3. Solid electrolyte interface

It has been learned that in a non-aqueous electrolyte, while the lithium ions are

accepting electrons at the surface of an anode, the organic solvent can also be reduced. The product of this reduction is a thin layer covering the surface of the anode. The thin layer is ionic conductive and acts as a solid electrolyte, called SEI. The evolution of the knowledge regarding the SEI is summarized in Figure 1-2 [33]. In early 1970, Dey et al. observed and concluded that lithium metal in a non-aqueous system was covered by a lithium ion conducting layer [34]. However, this layer was not well defined until Peled et al. first formally named it the SEI after investigating its chemical and physical properties in 1979 [35]. Firstly, the alkali metal electrode was covered by a dense SEI with a thickness of 20~40 Å. Secondly, the SEI was conductive for cation but insulating for electron. Finally, the thickness of SEI still increased with time of storage, even though it was a good electron insulator. The reason of the growth was that the inhomogeneous area was conductive towards electrons which would further reduce the solvent.

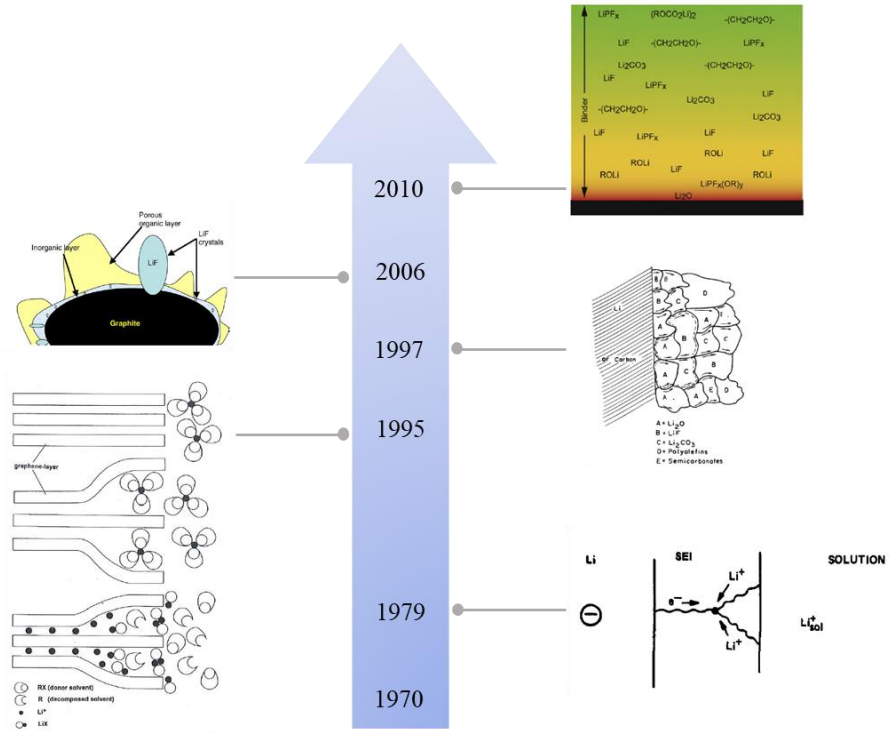

Figure 1-2. Evolution of knowledge of the SEI on the anode.

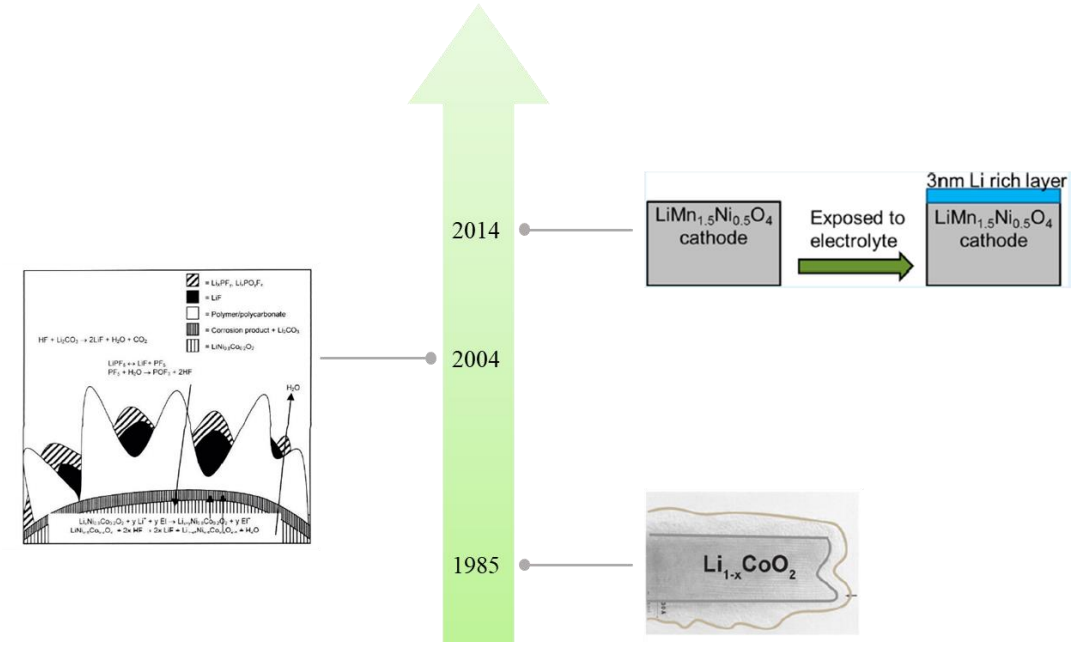

Figure 1-3. Evolution of investigation of SEI on the cathode.

One model to demonstrate the SEI formation on a graphite electrode was proposed by Besenhard et al. in 1995 [36]. It was found that the solvated graphite-intercalation compounds were $Li(solv)_yC_n$ which had a rather short lifetime, and the SEI was formed via the secondary reaction of the solvated compound. Moreover, according to the analysis, it was predicted that some of the electrolyte decomposition products were immobile and remained inside the graphite layer. Later, the SEI model was further refined by Peled et al. Combined with the systematic X-ray photoelectron spectroscopy (XPS) results by Kanamura et al [37]. and the EIS data, both the SEI components and the grain structure were predicted in their work [38]. A new insight of SEI by Edstrom et al indicated a two layers structure covering the electrode. With photoelectron spectroscopy (PES), it detected the SEI consists of a dense inorganic inner layer and the porous organic outer layer [39]. A different probing depth XPS on a lithiated graphite anode was conducted by Malmgren et al. With the chemical bond simulation on the XPS results, the depth profiling of the components was estimated [40].

Other than graphite anode, there is increasing SEI investigation on alloying electrode such as Si and Sn due to their competitive lithiation capacity as anode. Although some similar species was detected in the SEI of a Si anode, such as Li_2CO_3 and LiF, unique components such as siloxanes and SiO_xF_y were also found in the SEI [41] – [43].

In contrast to the anode, there is no thermodynamic driving force for electrolyte oxidation on most conventional cathode. However, a few studies reported that a SEI generated and grew on the cathode surface. An evaluation of the knowledge on cathode SEI can be summarized in Figure 1-3 [33]. The early research regarding to the cathode SEI dates

back to 1985 when Thomas et al detected the complex process on the cathode surface through ac impedance method, which indicated the oxidation of the electrolyte led a SEI formation on the cathode [44]. The detailed species of SEI on several cathode materials such as $LiCoO_2$, $LiMnO_2$, and $LiNi_{0.8}Co_{0.2}O_2$ were predicted by analyzing the XPS results [45]. Recently, an in-situ neutron reflectometry was conducted on $LiMn_{1.5}Ni_{0.5}O_4$ cathode by Browning et al. The thickness as well as the composition of the SEI on the cathode surface was predicted [46].

1.4. Electrochemical impedance spectroscopy

It has been shown in the previous paragraphs that various surface detection techniques contributed to understanding the SEIs on both the anodes and the cathodes in LIBs. Most of the ex-situ methods, such as X-ray diffraction (XRD), and XPS, rely on a direct detection of the sample recovered from a disassembled battery. However, during the processes of the sample disassembly, wash and transport, there were various chances for the sample to be exposed to an oxygen, moisture or other solvents, causing the changes of the sample surface either physically or chemically. Because of the high sensitivity of the SEI as well as the electrode materials, the sample under the detection may not represent at its original state anymore.

On the contrast, a non-destructive in-situ method keeps the integrity of a battery, where mostly eliminates the contamination and the exposure. Therefore, it provides a more reliable result. One of the techniques is the EIS. It has been a powerful tool since the early SEI research [44]. As the rapid development of the electronic devise, the efficiency and the accuracy of the EIS measurement are dramatically improved. An example of modern EIS was

conducted on graphite electrode by Chung et al [47]. The applications of EIS technique in the investigation of energy storage systems were recently reviewed by our group [48].

In an EIS, a sinusoid disturbance voltage at different ac frequency is applied to a battery. Based on the responded current, impedance can be calculated at each frequency. With frequency varying, an impedance spectroscopy can be obtained on a Nyquist plot.

In order to interpret the EIS result, it is necessary to simulate the data with an equivalent circuit. It has been evident that electric elements and their combination provide unique impedance profiles in the Nyquist plot, and an arbitrary impedance profile can be deconvoluted into a series of basic impedance profiles. Therefore, the EIS result from a battery can be presented with a series of electric elements. Once the certain equivalent circuit is found, the properties of the battery can be extracted through the parameters of the elements in the circuit.

In general, a double layer, interfacial reactions and mass diffusions are the three-major processes on the electrode surface. It can be mathematically proved that those electrochemical process can be represented by electric elements in an equivalent circuit

A double layer was formed due to a separation of charges on an electrode interface, when the electrode was immersed in an electrolyte, due to the difference of Gibbs free energy between the electrode and the electrolyte [48]. Equivalent amount of positive and negative charges was clustering parallel within the double layer; therefore, the double-layer behaved like a traditional capacitor. However, unlike a hard capacitor, the capacitance of the double layer is frequency dependent. In 1932, Frickee et al. first reported the constant phase element

(CPE) for modeling a distributed double layer behavior [49]. In 1994, Tamas Pajkossy et al. demonstrated that the CPE depended strongly on the state of the surface of the electrode. By comparing the electrodes with varying degrees of roughness, it was believed that the deviation from the ideal capacitance resulted from the inhomogeneity of the electrode surface [50].

The impedance expression for the double layer, Z_{CPE}, was summarized by Conway as [51],

$$Z_{CPE} = \frac{1}{Ti\omega^{p}} \tag{1-1}$$

Where T is the capacitance, and p is a factor representing the divergence from the ideal capacitor.

The electrochemical reaction on an electrode is governed by the Butler-Volmer equation. Taking a cathode as an example, the current density I can be expressed as,

$$I = i^{0} e^{-\frac{\alpha n F}{RT}\left(E-E^{0}\right)} \tag{1-2}$$

Where i^0 is the exchange current density, α is cathodic charge transfer coefficients, n is the number of moles of electrons, T is the temperature, E^0 is equilibrium potential, and E represents the potential of the electrode.

The Butler-Volmer equation gives the relationship between the operation voltage and current. Namely, it reflects the properties of the electrochemical reaction. A disturbance signal, ΔE, can be superimposed in the equation, and introduces the response, ΔI.

$$\Delta I = i^{0} e^{-\frac{\alpha n F}{RT}\left(E-E^{0}+\Delta E\right)} - i^{0} e^{-\frac{\alpha n F}{RT}\left(E-E^{0}\right)} \tag{1-3}$$

$$\therefore \Delta I = i^0 e^{-\frac{\alpha nF}{RT}(E-E^0)}\left(e^{-\frac{\alpha nF}{RT}\Delta E}-1\right) \tag{1-4}$$

Applying the Maclaurin series of an exponential function,

$$e^x = 1 + x + \frac{x^2}{2!} + \cdots + \frac{x^n}{n!} \tag{1-5}$$

the Butler-Volmer equation can be locally linearized with an assumption that the potential perturbation is significantly small,

$$\Delta I = -i^0 \Delta E \frac{\alpha nF}{RT} e^{-\frac{\alpha nF}{RT}(E-E^0)} \tag{1-6}$$

As a result, the electrochemical reaction at the electrode and electrolyte interface can be represented as a resistor R_F,

$$R_F = \frac{\Delta E}{\Delta I} = -e^{-\frac{\alpha nF}{RT}(E-E^0)} \frac{RT}{i^0 \alpha nF} = \text{const} \tag{1-7}$$

The impedance expression for a diffusion process derives from concentration gradient, which is governed by the Fick's second law,

$$\frac{\partial C}{\partial t} = D \frac{\partial^2 C}{\partial x^2} \tag{1-8}$$

Where C is the concentration, D is the diffusion coefficient.

Given an assumption that the consumption or the production of the charges in the electrochemical reaction is reasonably compensated by the mass transfer from or to the bulk electrolyte, the boundary condition at electrode surface can be expressed as,

$$\frac{\partial C}{\partial x}_{(x=0)} = \frac{I_0}{nFD} \sin \omega t \tag{1-9}$$

Assuming the scale where the concentration gradient is far less than that of the bulk

electrolyte, another boundary condition can be considered semi-infinite. Hence, as the distance reaching to the semi-infinite, the electrolyte concentration is close to the concentration of the bulk electrolyte, C_0. Therefore, the boundary condition of the other side can be expressed as,

$$C_{(x\to\infty)} = C_0 \tag{1-10}$$

The perturbation of the concentration at any location at any time can be analytically solved as [48],

$$\Delta C = C_0 - C = \frac{I_0}{nF\sqrt{\omega D}} e^{-\sqrt{\frac{2Dx}{\omega}}} \sin\left(\omega t - \sqrt{\frac{2Dx}{\omega}} - \frac{\pi}{4}\right) \tag{1-11}$$

From the expression, the solution near the electrode surface, ΔC_s, is the most significant aspect, which can obtain by substituting $x = 0$ into the equation.

$$\Delta C_s = \frac{I_0}{nF\sqrt{\omega D}} \sin\left(\omega t - \frac{\pi}{4}\right) \tag{1-12}$$

The relationship between the potential and the concentration is governed by Nernst equation. Assuming a constant bulk concentration of the reactant or product and a reversible electrochemical process, the Nernst equation can be simplified as,

$$\Delta E = \frac{RT}{nF} \ln\left(1 + \frac{\Delta C_s}{C_0}\right) \tag{1-13}$$

The expression can be linearized by assuming the concentration perturbation at the electrode surface is significantly smaller than the concentration in the bulk,

$$\Delta E = \frac{RT}{nF} \frac{\Delta C_s}{C_0} \tag{1-14}$$

Then, the impedance due to diffusion can be obtain by substituting equation (1-12) to

equation (1-14),

$$Z_D = \frac{\Delta E}{I_0} = \frac{RT}{n^2F^2C_0\sqrt{2\omega D}} - \frac{RT}{n^2F^2C_0\sqrt{2\omega D}}i \tag{1-15}$$

σ is defined as Warburg impedance,

$$\sigma = \frac{RT}{n^2F^2C_0\sqrt{2D}} \tag{1-16}$$

Therefore, the diffusion impedance can be written as,

$$Z_D = \frac{\sigma}{\sqrt{\omega}}(1-i) \tag{1-17}$$

The mathematical evidence indicates that each electrochemical process within a battery can be represented by a circuit element. Therefore, the EIS result of a battery can be simulated by an equivalent circuit. Then, the property of the electrode surface can be quantitatively evaluated from the parameters of the equivalent circuit.

A systematic EIS investigation on lithium-ion batteries was done by Nagasubramanian et al. in 1999 [52]. They conducted an experiment by using both electrodes from a commercial lithium-ion battery. EIS was taken in a two-electrode cell at different voltages and at different temperatures. A three-electrode cell was also tested with EIS. Without an equivalent circuit simulation, a direct summary from the result was the impedance of the cell grew significantly at low temperature. The three-electrode cell results yielded that the growth came mostly from the cathode part. Tetsuya et al. concentrated on the interpretation of EIS results with an improved equivalent circuit. A three-resistance and capacitor (RC) element-circuit was used in their EIS simulation. The result presented that the model fitted the experiment data well [53]. EIS investigations under different temperatures, from 20℃ to -20℃, was conducted by

the same group [54]. At high temperatures, the impedance from various components were found overlapped. However, at low temperature, each semicircle could be separated in the Nyquist plot.

Recent researchers also found EIS was a powerful method in the detailed investigation of the SEI. Miriam Steinhauer et al. studied the SEI formation on a graphite anode with EIS. In their research, a graphite/Li two-electrode half-cell and the same three-electrode cell with a Li as the reference were investigated. The in-situ EIS was taken during the first charge and the second charge for both cells. Simulating with the equivalent circuit, they summarized the process of SEI formation [55].

In terms of the EIS simulating, much of the existing work rely on an empirical circuit or an optimized circuit. However, due to the complexity of the electrochemical system, directly fitting the Nyquist plot from the frequency domain does not allow for the separation of the individual electrochemical process and makes the physical meaning of the results weak [56]. Therefore, in order to determine a more adequate equivalent circuit to suit for an individual battery, which reflects the genuine physical process, a distribution of relaxation times (DRT) transfers the impedance data from frequency domain to time domain.

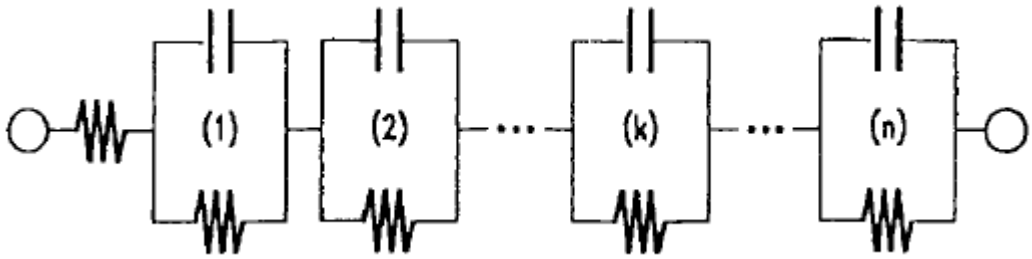

Figure 1-4. Finite Voigt circuit model [57].

In principle, a well-known electric system responding to a sinusoid signal can be modeled by a finite Voigt model which contains finite RC elements as shown in Figure 1-4. Each RC elements represents a specific process. The total impedance depending on the frequency is the sum of the individual RC elements.

For an electrochemical system, such as a battery, in order to identify each electrochemical process, using infinite Voigt model is necessary, because it reveals the distribution of the impedance along the relaxation time. It can be expressed as [58],

$$Z_{\mathrm{pol}}(\omega) = R_{\mathrm{pol}} \sum_{k=1}^{N} \frac{g_k}{1+i\omega\tau_k} = \sum_{k=1}^{N} \frac{R_k}{1+i\omega\tau_k} \tag{1-18}$$

Where $Z_{\mathrm{pol}}(\omega)$ is the impedance in frequency domain, R_k represents the relative share of the overall polarization resistance R_{pol} in vicinity of time-constant τ_k.

The impedance distribution in the time domain consists of peaks where represent the electrochemical processes. The x-axis location of the peak is the relaxation time which indicates the dynamic of the process. The height represents the impedance, and the width of the peak indicates the complexity of the process. As a result, each electrochemical process can be distinguished through DRT transform, then it provides guidance for creating an equivalent circuit to simulate the EIS data.

1.5. Prelithiation

Given the established knowledge for SEI in LIB, it has been realized that a well-generated SEI on the anode is the importance of a well-performing LIB. The reason is that the SEI prevents further decomposition of the electrolyte on the anode. Therefore, the quality of

the SEI determines the cycle efficiency, and the cycle life of a LIB. However, the research mentioned previously showed all the components in an anode SEI are lithium containing compounds. Namely, during the formation of the SEI, certain amount of lithium will be consumed. Therefore, a well-assembled battery is unavoidable to loss capacity during the formation cycles, which leads to a low ICE. One of the solutions is anode surface modification. An Al_2O_3 coated graphite anode was investigated by Feng et al. The testing results indicated a significant improvement in ICE due to a pre-formed SEI on the Al_2O_3 coated graphite [59]. In He et al work, Al_2O_3 was coated on a silicon anode through atomic layer deposition. The coated layer effectively alleviated the impact of the volume expansion and maintained the completeness of the SEI [60].

Prelithiation is another promising technique to solve the capacity loss problem as well as improving the cyclability. Prelithiation is defined as preloading lithium in an originally lithium-empty electrode before the battery assembly. For an LIB, it has been mentioned that the anode used to be the sink of lithium, therefore it is practical to prelithiate the anode and load up the lithium in the sink before making the battery.

As shown in Figure 1-5, the main reason to perform prelithiation on anode is compensating the lithium loss during the SEI formation. As mentioned, an SEI formed on the anode surface during the first couples of cycles in an LIB. Although, the electrolyte decomposition was the nature of the SEI formation, certain amount of lithium was also consumed and became irreversible in the subsequent cycles. The lithium loss during the first couples of cycles for an LIB was evident, the columbic efficiency, especially the ICE was

much lower than that in the following cycles. The lithium trapped in the SEI led to a permanently loss of the capacity of the battery. With the prelithiation, the SEI layer was formed chemically before the initial charge and discharge, and a certain amount of reversible lithium was loaded in the anode side chemically. During the initial formation cycles, the consumption of the lithium from the cathode side can be drastically reduced or even eliminated since the SEI layer was formed beforehand. During the discharging, the preloaded reversible lithium could compensate the overall cell capacity. As a result, the ICE improved and the overall capacity increased.

Besides, the prelithiation can artificially control the SEI formation. Instead of an accompanying reaction during the cycling, if the SEI can be formed during the prelithiation process, both the composition and the structure of the SEI can be engineered. As a consequence, it is possible to form a desired SEI in order to improve the performance of the LIB.

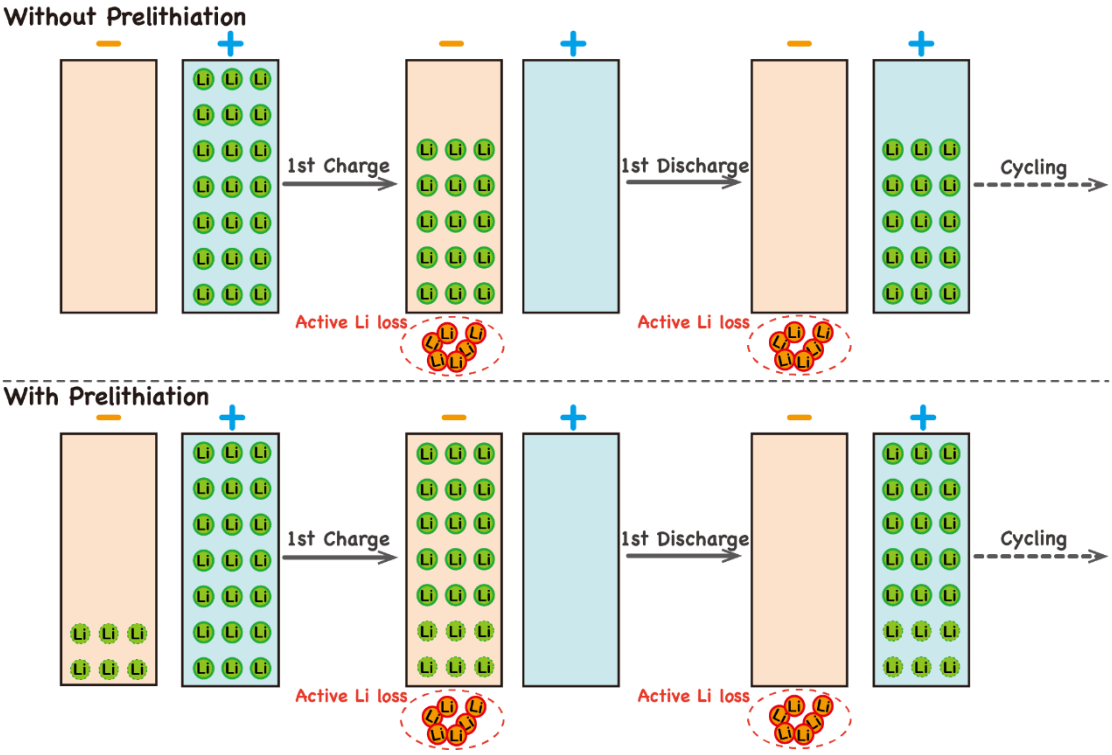

Figure 1-5. Schematic illustration of prelithiation for an LIB.

There are two major prelithiation methods, the electrochemical prelithiation and the chemical prelithiation. Electrochemical prelithiation generally involves a sacrificial metallic lithium electrode and an objective electrode. Through galvanostatic charge/discharge, the objective electrode can be lithiated to a precisely controlled lithiation stage. Abe et al conducted electrochemical prelithiation on a hard carbon anode. A half-cell containing a hard carbon electrode and a lithium metal was assembled. After charge/discharge on the half-cell, the prelithiated HC was rearranged in a full cell with NMC as the cathode. Although the cycle performance of the prelithiated cell slightly decreased, it was found the ICE was improved from 72% in the pristine cell to 85% in the prelithiated cell [61]. Holtstiege et al applied electrochemical prelithiation during the investigation of the carbon nanosphere anode. It was reported that the carbon nanosphere had poor ICE (30%~68%) because of its high surface area. However, with prelithiation, the ICE was significantly improved to over 90% [62]. Most of the electrochemical prelithiation procedure involved cell division and reassembly, which created complicity and were not suitable for a mass production.

The chemical prelithiation can be further classified: direct contact with lithium metal, lithium rich material additives, and lithium containing solution. Stabilized lithium metal powder (SLMP) is typically used in the direct contact method. A graphite anode was prelithiated through a direct coating of SLMP slurry by Ai et al [63]. It was tested the prelithiated graphite/NMC cell had an 88% increase in ICE as well as an improved cycle stability, although the prelithiation process took 48 hours to reach equilibrium. Other than using lithium metal, a lithium compound was used as lithium rich material additive. Sun et al

demonstrated a $Li_{2.6}Co_{0.4}N$ blended hard carbon anode exhibited nearly 100% ICE in a half cell. However, the hard carbon/ $Li_{2.6}Co_{0.4}N$ slurry had to be prepared then coated in an inert gas ambient [64]. Zhao et al reported Li_xSi-Li_2O core-shell nanoparticles as a prelithiation additive in both the graphite and the silicon anode for LIB. The prelithiated silicon anode presented a better Coulombic efficiency in the second cycle than the pristine silicon. Although the process was conducted in an argon filled glovebox, the slurry with the prelithiation additives was tested stable in dry air [65].

Using lithium containing solution is a promising prelithiation method. By immersing the electrode in a prelithiation reagent, the electrode can be lithiated spontaneously driven by the chemical reaction. The beauty of this method includes short prelithiation time, stability in dry air and compatibility with existing electrode production line. In order to make the process happen, a prelithiation reagent needs to be carefully selected. It has been learnt that a metal radical anion of aromatic hydrocarbons is immediately formed when adding an alkali metal to an organic solution of an aromatic hydrocarbon, whose reducing capability is mostly as strong as lithium metal. Our previous work reported that lithium biphenyl in tetrahydrofuran has a redox potential of ~0.4V, which successfully reduced P and Sn. During the reaction, the lithium was captured by reduced P and reduced Sn as the biphenyl cation oxidized, it was leading to the successful prelithiation on P and Sn [66], [67].

1.6. Aim of the thesis

The purpose of the research in this thesis is to improve the ICE for LIBs with either carbon or silicon-based anode, as well as increasing the reversible capacity of the battery

without losing its cycle life.

A prelithiation with lithium containing solution is the focused method for the aim, due to its high prelithiation efficiency and its potential to be easily installed in existing roll-to-roll electrode production line. Experiments of a HC anode prelithiation and a SiO anode prelithiation will be presented and discussed in Chapter 3.

In addition to compensate the initial capacity loss through prelithiation, the qualities of the SEI formation during the chemical prelithiation and the electrochemical lithiation are also the study concentration in this thesis, since the stability of the SEI determines the cycle life of the battery. The investigation method is EIS in this thesis. Combining the DRT transform, a representative equivalent circuit can be created to simulate the EIS results, providing quantitative properties of the electrochemical processes within a battery. A mechanism investigation on EIS behavior of an electrode will be presented, and an EIS analyzing method will be established in Chapter 2. Then, it will be applied on prelithiation in Chapter 3. The EIS investigation was based on the comparison between an LIB with a state-of-the-art electrolyte and an LIB with an improved electrolyte, under various temperature and aging conditions. In these experiments, the performance contrast of the two cells can be reasonably interpreted from the differences of the EIS outputs of the two cells.

CHAPTER 2. AC IMPEDANCE AS THE EXPERIMENT TOOL ON ELECTRODE SURFACE DIAGNOSIS

2.1. Introduction

The prelithiation with lithium containing solution method relies on a redox reaction on the surface of the electrode. The reaction carries the lithium intercalation. However, it may also carry side reactions leading the generation of an interface on the electrode surface. There was no evidence to predict the differences between the prelithiation interface and the electrochemically generated SEI before taking any surface diagnosis measures. Moreover, the chemically formed interface during prelithiation may vary when charging the battery and form a SEI different from the pristine battery both on structure and on composition.

Although the major purpose of prelithiation was to improve the ICE, it was also our goal in this research to maintain a good cyclability of a prelithiated LIB. The reason to discuss the SEI diagnosis before proceeding the prelithiation experiments was that the SEI significantly affects the stability and the cycle life of an LIB as mentioned in Chapter 1. It has been learnt that the SEI was formed on the anode through the reduction of the electrolyte. While preventing the further reaction between anode and electrolyte during cycling, the SEI layer also facilitates lithium-ion passage to the anode. A good SEI layer is thin, robust and has high ionic conductivity and high ohmic resistivity [68].

There are many ways to detect the quality of the interface. However, it has been presented in Chapter 1 that EIS has been used to characterize the LIB for a long time [25], [48],

[69] – [72]. The beauty of the method is that the analysis can be done in-situ without opening the cell making the data more reliable. The impedance measured over a wide frequency range offers more information regarding the electrochemical processes in a time domain than in a frequency domain. In general, there are a few processes in an LIB which can be identified from an impedance spectrum,

Inductive reactance from wires and metallic elements in the cell which appears at high frequency.

The Ohmic resistance due to electrolyte and separator which is the point where imaginary impedance is zero.

The contribution of SEI which could be a semi-circle at high to mid frequency region.

Charge transfer resistance and double-layer capacitance, which could be a semicircle from mid to low frequency region.

The diffusion of lithium ion inside the electrodes.

However, the experimental data did not normally show well separated semicircles or lines, or points as predicted by the theory. Therefore, extracting the parameters for the individual electrochemical process from EIS data became a very challenging task [73], [74]. Furthermore, unless a reference electrode was used, it was hard to separate the impedance contribution of the anode and cathode. Installation of a reference electrode has been a common practice for the electrochemical research. A reference electrode would be a good way if the polarization was uniform throughout the large electrode and the implementation of the reference electrode would not alter the performance of the cell. Other methods such as use

of symmetric cells have also been discussed [75].

It was necessary to establish an EIS diagnosis method to support the prelithiation experiments. Therefore, in this chapter, we mainly focused on EIS investigation. The investigation was based on a comparison between two cells with significantly contrast cycling performance. One contains a wide temperature electrolyte system developed through high-throughput screening for LIB in a previous work of our group. The other contains the state-of-the-art electrolyte. The cell cycling and the EIS measurements were conducted at both low temperature and elevated temperature. In order to separate the EIS contributions of the anode and the cathode, single layer three-electrode pouch cells were designed and assembled with a graphite anode, a NMC 111 cathode and a lithium reference.

2.2. Impedance investigation and cycling performance at low temperature

We have reported that the low temperature performance of an LIB can be tremendously improved by selecting the common solvents in proper ratio as opposed to using the 3 EC/ 7 EMC ratio, which is the state-of-the-art electrolyte for LIB [25]. The root causes of the better performance were not fully understood. However, it was believed that the qualities and composition of SEI were the critical factors.

In order to understand the mechanism, ac impedance was measured for anode, cathode and the complete cell respectively in a three-electrode pouch cell at various temperatures. In every case the same sized pouch cell was used for the two types of electrolytes. One electrolyte was the best wide temperature electrolyte (1.0 M $LiPF_6$ in 5 EC/ 30 DMC/ 65 EMC with 1% VC and 0.5% LiBOB) that was developed in our lab by a high through

screening. The other electrolyte was the state-of-the-art electrolyte (1.0 M $LiPF_6$ in 3 EC/ 7 EMC).

2.2.1. Experimental details

Chemicals

$LiPF_6$ (99.99%), battery grade LiBOB, and VC (99.5%, acid < 200 ppm, H_2O <100 ppm) were purchased from Sigma Aldrich and used without further purification. EC, DMC, and EMC solvents were purchased from BASF Corporation, Ohio and used without further treatments. In the NMC 111 cathode laminate, the loading of the active material was 6.80 mg/cm^2 and the reversible capacity was 0.93 mAh/cm^2; in the graphite anode laminate, the loading was 3.25 mg/cm^2. Both cathode and anode were made in the on-site automate pilot facility in our lab, with over 100 m of electrode laminates were made to ensure quality consistence. The Celgard 2325 polymer was used as separator.

Electrolyte preparation

Electrolytes were prepared in an argon filled glove box (H_2O < 0.5 ppm, O_2 < 1 ppm). Mixtures of 10.0 g of solvent combination (EC, EMC, DMC) at desired ratio were made. For convenience we identified these two electrolytes as “baseline” and “improved”. The baseline electrolyte solvent had EC/EMC in mass ratio 3:7. The improved electrolyte contained solvent mixture EC, EMC and DMC in 5: 30: 65 mass ratios. Lithium salt, $LiPF_6$ (1.51 g) was added to each of the solvent composition to make 1.0 M solution. In the improved electrolyte solution, 0.11 g vinylene carbonate and 0.057 g LiBOB were added to make 1% and 0.5% by weight of the electrolyte respectively. The mixture was left overnight to ensure

the complete dissolution of the salts and additives.

Fabrication of pouch cells with the implantation of reference electrode

Rectangular pieces of cathode (140 mm * 73 mm) and anode (142 mm * 77 mm) were used to construct pouch cells. The total theoretical capacity per cell was 95.0 mAh. Lithium foil (0.2 mm thickness and 15.8 mm diameter) was used as the reference electrode.

The electrodes were welded to the current collector tabs in a dry room using an ultrasonic welding machine. A nickel coated aluminum tab was welded with the cathode, and a nickel coated copper tab was welded with the anode and the reference electrode.

The pouch cells were assembled in the glove box. The cathode and anode were separated by two pieces of separator. Two pieces of lithium foil were pressed with the copper foil and sandwiched between the separators. A 3.0 g electrolyte was added in each of the pouch cells and spread uniformly. After electrolyte was filled, the pouch was sealed under low vacuum. The case of the pouch cell was the aluminum laminated film coated with nylon.

Electrochemical measurements

The cells were charged by constant current of C/20 until the voltage reached 4.1 V, then discharged at a constant current of C/20 until the voltage decreased to 2.0 V. The process was repeated two times. Then, constant current charge/discharge cycles at a rate of C/10 were applied between 2.0 V and 4.1 V three times. Between each charge and discharge cycle, the cell was rested for one minute. The entire formation process was completed at 25°C.

After the completion of formation, the cells were charged with 1C rate at 25°C and then cooled to -20°C for 2 hours before discharged at a 5C rate.

The cells were then warmed to 25°C and allowed to stay at this temperature overnight. These cells were then cycled for 50 cycles at 1C charge and 5C discharge rate at the temperature. At the end of the 50 cycles, the -20°C discharge cycle was repeated.

The cells were then warmed to 60°C, rested overnight, and cycled for 50 cycles at a 1C charge and 5C discharge rate at 60°C. At the end of the high temperature 50 cycles, the -20°C discharge were done for cold temperature performance.

The cells after formation were charged to 100% state of charge (SOC), at 1C rate at 25°C. After resting for 2 hours, the impedance was taken at 25°C. Then, the cells were cooled to -20°C and rested for 3 hours before the impedance was measured again.

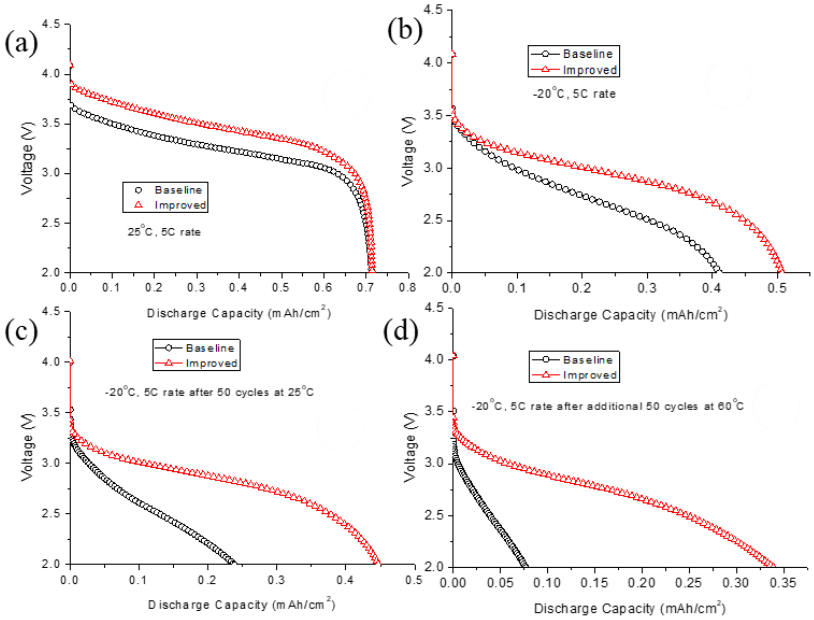

Figure 2-1. Comparison of baseline electrolyte and improved electrolyte in pouch cell format. (a) discharge at room temperature after formation; (b) discharge at -20ºC after formation; (c) discharge at -20ºC after 50 cycles at room temperature; (d) discharge at -20ºC after 50 cycles at 60ºC

2.2.2. Results and Discussion

Performance of the electrolytes

Before conducting the impedance analysis, the performance of the improved electrolyte was compared with the baseline electrolyte. Figure 2-1 shows the comparison of 5C discharge of pouch cells made with baseline electrolyte and improved electrolyte 5C rate was chosen, because one of the high-rate applications was cold cranking. Four cells were tested in each group and the standard deviations (SD) of discharge capacity were around 0.0126 mAh/cm^2 and 0.026 mAh/cm^2 at room temperature and 60°C cycles, respectively. Since the electrodes were from pilot production, mAh/cm^2 was used instead of mAh/g, because it was easy to be called up to full production. The small value of the SD was evident of the reproducibility of the pouch cells. In addition, Figure 2-1 clearly demonstrated the superior low temperature performance of the improved electrolyte especially after the cycled at high temperature (60°C).

Quality of the impedance data

Although ac impedance is a powerful electrochemical technique which has been widely used as diagnostic tool to investigate LIBs, due to the complexity of a LIB system, the system may deviate from the ideal linear and stationary conditions which are required for accurate modelling. The conditions of causality, linearity, stability and finiteness may not be satisfied [48]. Experimentally, the excitation signal should be large enough to ensure accuracy, but not too large to drive the battery from region of linearity. Also, it may take a relatively long rest time for the system to reach stability since the electrodes in a LIB were normally made with

porous materials which results of long relaxation time. Therefore, it is important to make sure the obtained ac impedance data points were reliable and representative to make sure the accuracy of the subsequent equivalent circuit modeling. A Kramers-Kronig (K-K) relationship was commonly used to verify the quality of impedance data at each frequency [54], [76] – [79]. Theoretically, for a stable system, the real and imaginary parts of the impedance are interdependent. In another words, the real part of an impedance can be obtained by direct integration of K-K equations and vise verse. The K-K equations are listed below,

$$Z'(\omega) = \lim_{\omega \to \infty} \left[Z'(\omega) \right] + \left(\frac{2}{\pi} \right) \int_0^{\infty} \frac{x Z''(x) - \omega Z''(\omega)}{x^2 - \omega^2} dx \tag{2-1}$$

$$Z''(\omega) = \left(\frac{2\omega}{\pi} \right) \int_0^{\infty} \frac{Z'(x) - Z'(\omega)}{x^2 - \omega^2} dx \tag{2-2}$$

The calculated real (from imaginary) and imaginary (from real) can then be compared with the experimental results. The divergence between the calculated values and experimental values should be low enough to ensure the stability of the system and validity of the data.

The K-K validation is critical to a battery system. Due to the high porosity nature of battery electrodes, it takes very long time for a battery to reach a true stable state, the "stability" of a battery system would be relative to the frequency of the excitation signals. Figure 2-2 shows the K-K validation of two typical impedance data from the research. Figure 2-2(a) shows the spectrum of K-K compliance, while Figure 2-2(b) shows the K-K non-compliant impedance spectrum. In Figure 2-2, the symbols are experimental data; solid lines are the least square fitting based on the equivalent circuit shown in the corresponding insert in Figure 2-2(b); while the dashed-lines are the impedance spectrum based on K-K

calculation (real impedance was calculated from imaginary and vice versa using Equation (3-1) and Equation (3-2). It is clearly shown in Figure 2-2(a) that the spectrum was K-K compliant, the errors in different frequency ranges were different. Another observation that needs to be pointed out is shown in Figure 2-2(b), an apparent good fit can be achieved even though the data were not K-K compliant, that is the major risk of data misinterpretation using equivalent circuit fitting for impedance spectrum. All the data used in this paper were K-K compliant, non-compliant data were removed.

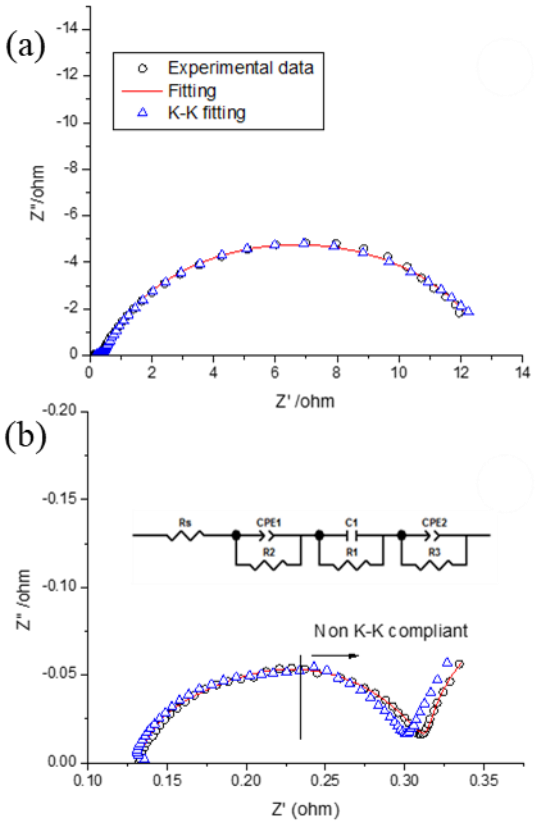

Figure 2-2. Numerical fitting and K-K fitting of typical impedance spectrum. (a) K-K compliant; (b) K-K non-compliant; The equivalent model was used to calculate the impedance points outside the measured frequency range.

Building equivalent circuit by the identification of electrochemical process at different frequency ranges through the DRT

Traditionally, an equivalent circuit was built based on the educated speculations of the electrode processes, e.g., Randall circuit, and the practice has been working well for simple electrochemical systems e.g., corrosion. However, a battery system is highly complex due to the integration of multiple physical and electrochemical processes. For example, most, if not all, battery systems consist of porous electrodes. Interfacial charge transfer reactions occur on both outer surface and inner surface of the pores the mass transfer is partially determined with the pore size distribution. Such processes may interweave with each other in various frequency ranges; therefore, different equivalent circles may be used to fit the impedance spectrum at different frequency ranges. Before the equivalent circuits of frequency ranges can be determined, the frequency range of each processes have to be deconvoluted.

Any electrochemical impedance regardless of the electrochemical nature can be descripted as a generalized circuit consisting of a continuous distribution of RC elements in the space of relaxation of time [48]. Therefore, the impedance can be fitted without prior assumptions of the physical and electrochemical processes and each process can be distributed along the change of the relaxation times which presents the rate constants of the corresponding processes. The practical relation between the impedance and its DRT is demonstrated in Chapter 1 Equation (1-18). Noted that R_k represents the relative share of the overall polarization resistance R_{pol} in vicinity of time-constant τ_k. The polarization processes of different time-constant can now be separated in a R_k vs. τ_k graph as shown in Figure 2-3,

while the peak area is proportional to the polarization resistance and the x-axis is the time-constant τ.

In order to better separate the anode and cathode contribution to the cell impedance, a reference electrode (Li^+/Li) was implanted between the cathode and anode in a pouch cell. Impedance spectrums were measured at room temperature and -20°C. Figure 2-3 shows the comparison of the impedance spectrum of the cells made with baseline electrolyte and the improved electrolyte at 25°C and -20°C, while the corresponding DRTs are also shown in the Figure 2-3.

The DRT offers direct access to the rate constants (relaxation times) of each physical and electrochemical processes from the impedance spectrum, as do the polarization resistances (relaxation amplitudes), which can be calculated by the integration of the corresponding peaks. Although the DRT was calculated using a universal transmission line model with no physical representation for the system under investigation, the DRT can be used to separate the impedance-related physical processes and can undeniably assist the identification of such processes. For example, as shown in Figure 2-3(a) and Figure 2-3(a'), in the baseline electrolyte the anode has three significant processes, while the cathode has two significant processes. Both cathode and anode played important roles when operated at ambient temperature. The limitations for the electrodes in the improved electrolyte at room temperature are similar to the baseline. The cathode processes were almost identical to those in the baseline electrolyte, while the processes in the anode were more complex than those in the baseline electrolyte. Significant differences can be observed for the cells in -20°C. It was

interesting that the two processes for the cathodes at -20°C were about the same as those at room temperature, although the relaxation time (rate constants) changed. The most important observation was that unlike at room temperature where both cathode and anode made fair contributions to the cell impedance, the anode processes made dominant contribution to the cell impedance at -20°C, where only two apparent processes can be identified, which is consistent with we reported previously [25].

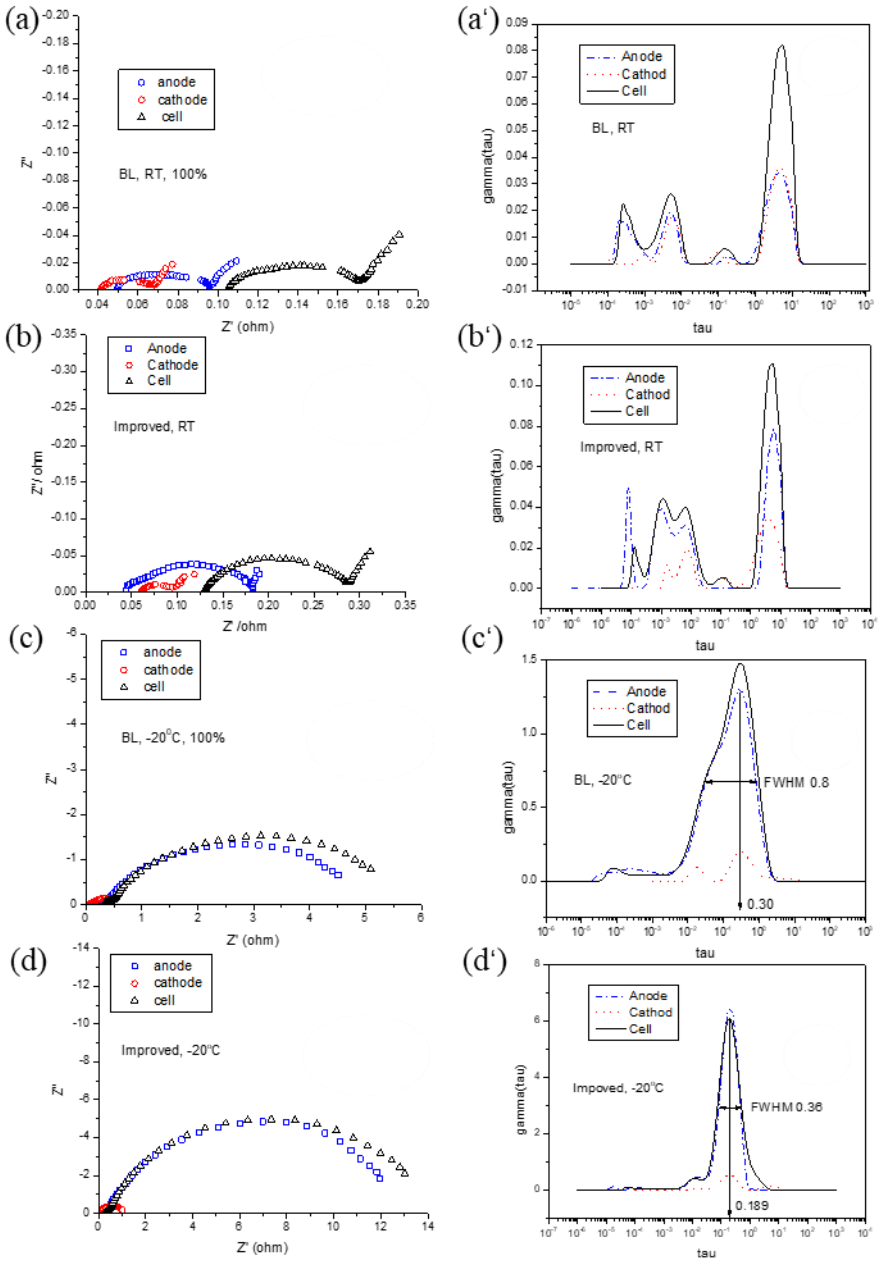

Figure 2-3. The comparison of the impedance spectrum and DRT. (a) and (a'): baseline (BL) electrolyte at room temperature (RT); (b) and (b'): improved electrolyte at room temperature; (c) and (c'): BL electrolyte at -20°C; (d) and (d'): improved electrolyte at -20°C.

Bearing in mind that DRT was based on a universal transmission line model in which the specific nature of the processes was not taken into consideration, it just revealed the kinetic aspects of the processes. The remaining challenge, of course, is to identify the processes and correlating them to the kinetic characteristics. Figure 2-4 shows the equivalent circuit of the anode developed through DRT. The equivalent circuit consists of two R/C (CPE) loops representing the two processes revealed in DRT. The R_{ct}/C represents the interfacial charge transfer reaction resistance and double-layer capacitance between the anode and SEI layer. The CPE/R represents the Li ion diffusion in a non-uniform SEI and within the graphite lattice. The ohmic resistance (R_s) consists of the electronic resistance e.g., contact resistance between particles and current collectors, and ionic resistance e.g., electrolyte resistance. The solid line in Figure 2-4 shows the excellent fitting for the impedance spectrum.

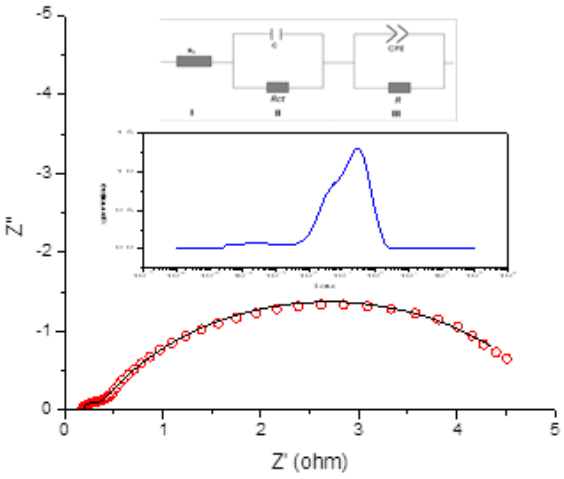

Figure 2-4. Building the equivalent circuit based on DRT.

Fitting the experimental impedance spectrum at -20°C

Figure 2-5 shows the comparison of experimental data and the fitting curves for the anode in both the baseline electrolyte and the improved electrolyte based on the equivalent circuit shown in Figure 2-4. The fitting parameters are tabulated in Table 2-1. As demonstrated, the fitting errors were almost below 10%.

The pouch cell (with reference electrode implanted) results echoed those of the previous coin cell (no reference electrode) for example, the conductivity of electrolyte played minor roles in low temperature performance [25]; the major contribution to the cell impedance was from the anode instead of the cathode etc. In addition, the interfacial charge transfer reaction was similar as shown in Table 2-1.

Interestingly, conventional wisdom taught us that the electrode showing large semi-circle would have poorer rate capability than that with smaller semi-circle. Apparently, the hypothesis was not true in this case. A good SEI layer should be electrically insulation while ionically conductive, in other words, an SEI layer should block electron transfer, while facilitate ion diffusion. As shown in Figure 2-5, the semi-circle of the impedance for the anode in the improved electrolyte was substantially larger than that of the baseline electrolyte. Indeed, the R value of the improved electrolyte is significantly higher than that of the baseline electrolyte. DRT peaks shown in Figure 2-3 may provide the explanation for the phenomena. Comparing DRT graph in Figure 2-3(c') and Figure 2-3(d'), although the peak area in Figure 2-3(c') was significantly larger than that of Figure 2-3(d'), the peak position of the major peak in Figure 2-3(d') (0.19) was at lower relaxation time than that of Figure

2-3(c') (0.3), the full width at half maximum (FWHM) of Figure 2-3(d') (0.36) was also smaller than that of Figure 2-3(c') (0.80). Therefore, although the polarization resistance of the processes for the anode in baseline was smaller, the kinetics for the processes were much more sluggish for the anode in the baseline electrolyte than that of the improved electrolyte. Indeed, the two major processes for the anode in the improve electrolyte can be clearly separated while they overlapped for that of baseline electrode, indicating the more favorable kinetic process in the improved electrolyte. The CPE is used to model the diffusion in a distributed a non-homogeneous matrix e.g., the matrix with wide pore distribution. For the diffusion in a homogenous matrix, CPE-P is equal to 0.5, the well-known 45-degree line shows on the Complex-Plane graph and 1/CPE-T is proportional to the diffusion coefficient. The deviation of CPE-P from 0.5 illustrates the degree the system deviates from its homogeneity. The CPE/R loop in the equivalent circuit was used to simulate the ionic diffusion in the non-homogeneous and porous SEI layer. Table 1 tabulates the fitting results for the two electrodes. The CPE-T for the anodes in the baseline electrolyte and in the improved electrolyte were 0.87 and 0.63, respectively, while the one in the baseline electrolyte deviated away from 0.5 more than that of improved electrolyte. It was evident that the more non-homogenous nature of the SEI layers in the anode in the baseline electrolyte. Consequently, the CPE-T for the improve electrolyte (0.01) was smaller than that of the baseline electrolyte (0.06), or Li diffusion coefficient in the SEI layer in improved electrolyte was substantially higher than that in the baseline electrolyte. The conclusions were in agreement with those in the previous publication [25].

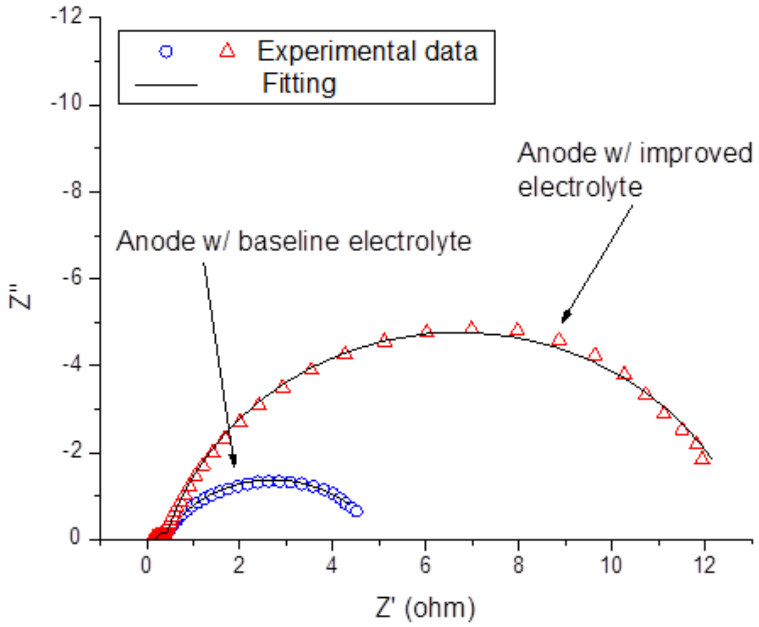

Figure 2-5. ac impedance spectrum and their fittings for the anodes in both baseline electrolyte and improved electrolyte.

Table 2-1. Equivalent fitting results for the impedance spectra

	R_s(Ω)	C (mF)	R_{ct} (Ω)	R (Ω)	CPE-T	CPE-P
Baseline	0.18 (0.8%)	0.86 (3.2%)	0.14 (2.3%)	4.7 (1.2%)	0.06 (1.8%)	0.87 (5.4%)
Improved	0.201 (8%)	0.8 (3.3%)	0.2 (10.4%)	12.6 (0.3%)	0.01 (0.53%)	0.63 (5.3%)

2.2.3. Conclusion

It is clearly demonstrated that the determination factor for the low temperature performance is on the graphite anode. Using DRT, the relaxation time (rate constant) for the electrode processes can be revealed through impedance spectrum. Combining DRT and equivalent circuit fitting show important roles that the homogeneity of the SEI layer on the surface of the anode plays. In addition, Li-ion diffusion kinetics through the SEI layer is more influential than the actual polarization resistance to the low temperature performance of the graphite anode.

2.3. High temperature performance and impedance investigation

As we presented that adjusting the ratio of EC, EMC and DMC affected the quality of the SEI [25], an electrolyte with EC/EMC/DMC 5/30/65, 1% VC, 0.5% LiBOB was proven to have an excellent low temperature performance. However, its cycling performance and SEI properties at high temperature remained unclear.

The SEI characterization was relied on ac impedance measurement. However, due to the complexity of the processes on an electrode, most of the time, the process cannot be explicitly identified on the Nyquist plot of an EIS. As a result, it was hard to precisely create a representative equivalent circuit. It has been realized that the DRT transformation was a powerful tool to distinguish the process by converting an EIS result from a frequency domain to a time domain via rewriting the measured impedance as a sum of finite RC elements [56], [80]. In a DRT, each electrochemical process is believed to be represented with a peak at different relaxation times [56]. Therefore, not only the process can be identified, but also the

kinetics and the resistance associated with the process can be estimated directly from the DRT plot by reading the horizontal position and the height of the peak.

Additionally, SEI properties after elevated temperature cycling were investigated by combining EIS and its DRT transform. A three-electrode pouch cell was made and used to measure the anode and cathode impedance separately. The electrolyte was the best low temperature electrolyte developed in our lab (1.0 M $LiPF_6$ in EC/DMC/EMC 5/30/65 with 1% VC, 0.5% LiBOB) [25]. The state-of-the-art electrolyte (1.0 M $LiPF_6$ in EC/EMC 3/7) was used as a baseline electrolyte.

2.3.1. Experimental details

Chemicals

Battery grade EC, EMC, DMC (99.9%, acid < 10 ppm, H_2O < 10 ppm) and $LiPF_6$ (99.99%) were purchased from BASF Corporation, Ohio and used without further purification. LiBOB and VC (99.5%, acid < 200 ppm, H_2O < 100 ppm) were purchased from Sigma Aldrich and used without further purification. The NMC 111 cathode laminate was loaded with the active material of 6.80 mg/cm^2 and had the theoretical capacity of 0.93 mAh/cm^2. The graphite anode laminate was loaded with the active material of 3.25 mg/cm^2. Both the cathode and the anode were made in the on-site automated pilot facility in our lab. Over 100 m electrodes laminates were made to guarantee the consistence of the quality.

Electrolyte Preparation

Two electrolytes were made by dissolving 1.0 M $LiPF_6$ in the solvent of the desired ratio. For the sake of convenience, one was identified as “baseline” electrolyte, and the other

was identified as “improved” electrolyte. For the baseline electrolyte, 1.0 M $LiPF_6$ was dissolved in EC and EMC solvent (3:7 mass ratio). For the improved electrolyte, 1.0 M $LiPF_6$ was dissolved in EC, EMC and DMC solvent (5:30:65 mass ratio) with adding 1% VC and 0.5% LiBOB (by weight) as additives. The mixtures were left overnight before using. All the electrolyte preparation was conducted in an argon-filled glove box (O_2 < 1 ppm, H_2O < 0.5 ppm).

Cell Fabrication

Before assembling the three-electrode pouch cell, the NMC cathode was cut into a 4 cm * 5 cm piece and the graphite anode was cut into a 4.4 cm * 5.2 cm piece, which made the theoretical capacity based on the cathode be 18.6 mAh per cell.

An aluminum tab was welded onto the cathode using an ultrasonic welder, and a nickel tab was welded onto the anode using a spot welder.

Two lithium foils (0.2 mm thickness and 15.8 mm diameter) were pressed onto a nickel tab and were sandwiched right in the middle, in between the cathode and the anode as a reference electrode, with both sides separated by the Celgard 2325 separators.

A nylon coated aluminum laminated film case was used to seal the three-electrode pouch cell. After adding 1 ml electrolyte, the assembled pouch cell was heat sealed under low vacuum. All the assembly and seal processes were conducted in the argon filled glove box.

Electrochemical Measurement

The voltage window for all the three-electrode pouch cells was 2.0~4.1 V. In the formation process, the cells were first charged and discharged at C/20 rate (1C = 18.6 mAh)

for 2 cycles, then followed by a C/10 charge and discharge rate for 3 cycles. The formation process was conducted at 25°C. After the formation, the cells were cycled at 1C charge and a discharge rate at 60°C for 100 cycles. After the 100 60°C cycles, the cells were followed by a 1C charge rate at 25°C and a 1C discharge rate at -20°C for 2 cycles.

In the three-electrode pouch cell, the EIS was measured for the anode, the cathode and the complete cell during the cycles, respectively. An Autolab PGSTAT30 potentiostat/galvanostat electrochemical system was used for the EIS measurements. The measurements were conducted in a frequency ranging from 10^{-2} Hz to 10^{6} Hz and a sinewave potential input signal with an amplitude of ±10 mV against the reference electrode.

Three times of the EIS were recorded on each cell at the state of after formation, the state of after 50 60°C cycles, and the state of after 100 60°C cycles, respectively. All the EIS measurements were done at room temperature and at 100% state of charge of the cell.

2.3.2. Results and Discussions

In order to eliminate the coincidence, two repeat cells for each electrolyte were made. The differences of the capacity measurements and the EIS measurements between the repeat cells were less than and respectively. The presented results were selected from one the repeats.

Figure 2-6 show the comparison of the cycling performance of the cells with the improved electrolyte and the baseline electrolyte at 1C rate at 60°C. At the beginning of the cycle, the baseline electrolyte exhibited 16.8 mAh discharge capacity, which delivered 90% of the total theoretical capacity. The improved electrolyte provided 15.8 mAh, which was

85% of the total theoretical capacity. The improved electrolyte appeared to consume more Li to build the SEI layer during the formation cycles. Both electrolytes maintained the capacities above 70% of the theoretical capacity in their first 20 cycles at 60°C. Then, the cell with the baseline electrolyte lost its capacity slightly faster than the improved electrolyte along the cycles. After 50 cycles at 60°C, the cell with the baseline electrolyte was discharged with 8.8 mAh capacity and the cell with the improved electrolyte provided 8.2 mAh discharge capacity. However, after 100 high temperature cycles, the cell with the baseline electrolyte had 4.0 mAh capacity, while the cell with the improved electrolyte had 4.4 mAh discharge capacity. The cell with the improved electrolyte maintained a higher 98% Coulombic Efficiency against 96% Coulombic efficiency for the baseline electrolyte after 100 cycles at 60°C. Our previous report concluded that the improved electrolyte presented higher discharge capacity at -20°C than that of the baseline electrolyte after formation. As shown in Figure 2-7, the cell with the improved electrolyte maintained 91% capacity at -20°C after 100 cycles at 60°C, while the cells with baseline electrolyte demonstrated 40%. It was evident that the improved electrolyte had a close performance at 60°C in comparison with the baseline electrolyte, but the improved electrolyte slightly outperformed the baseline electrolyte after 60 cycles at the elevated temperature. However, the improved electrolyte still retained its performance superiority against the baseline at -20°C, even after 100 cycles at 60°C. In conclusion, the improved electrolyte had parity performance with the benchmark at 60°C, while missing word here had superior performance at -20°C. The improved electrolyte clearly demonstrated an excellent performance in crossing the wide range of operation temperature.

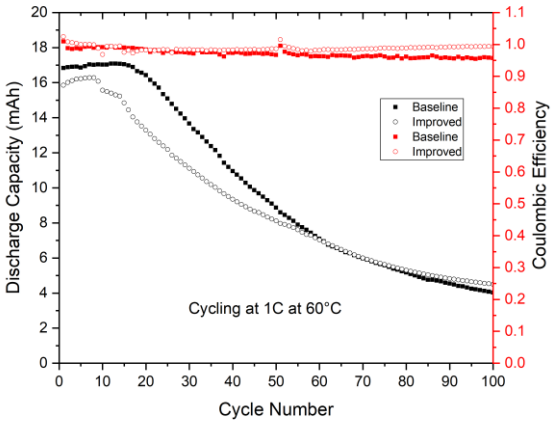

Figure 2-6. High temperature cycling performance of the three-electrode cells.

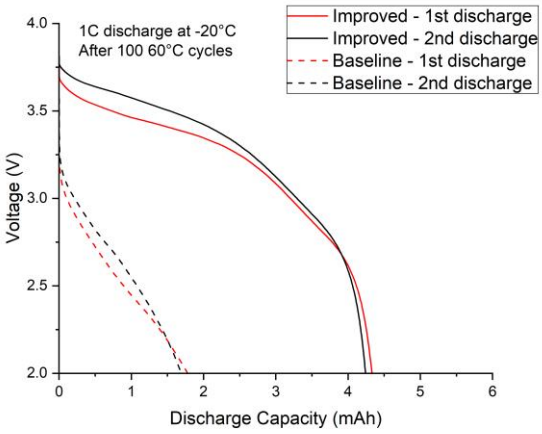

Figure 2-7. Low temperature discharge performance of the three-electrode cells.

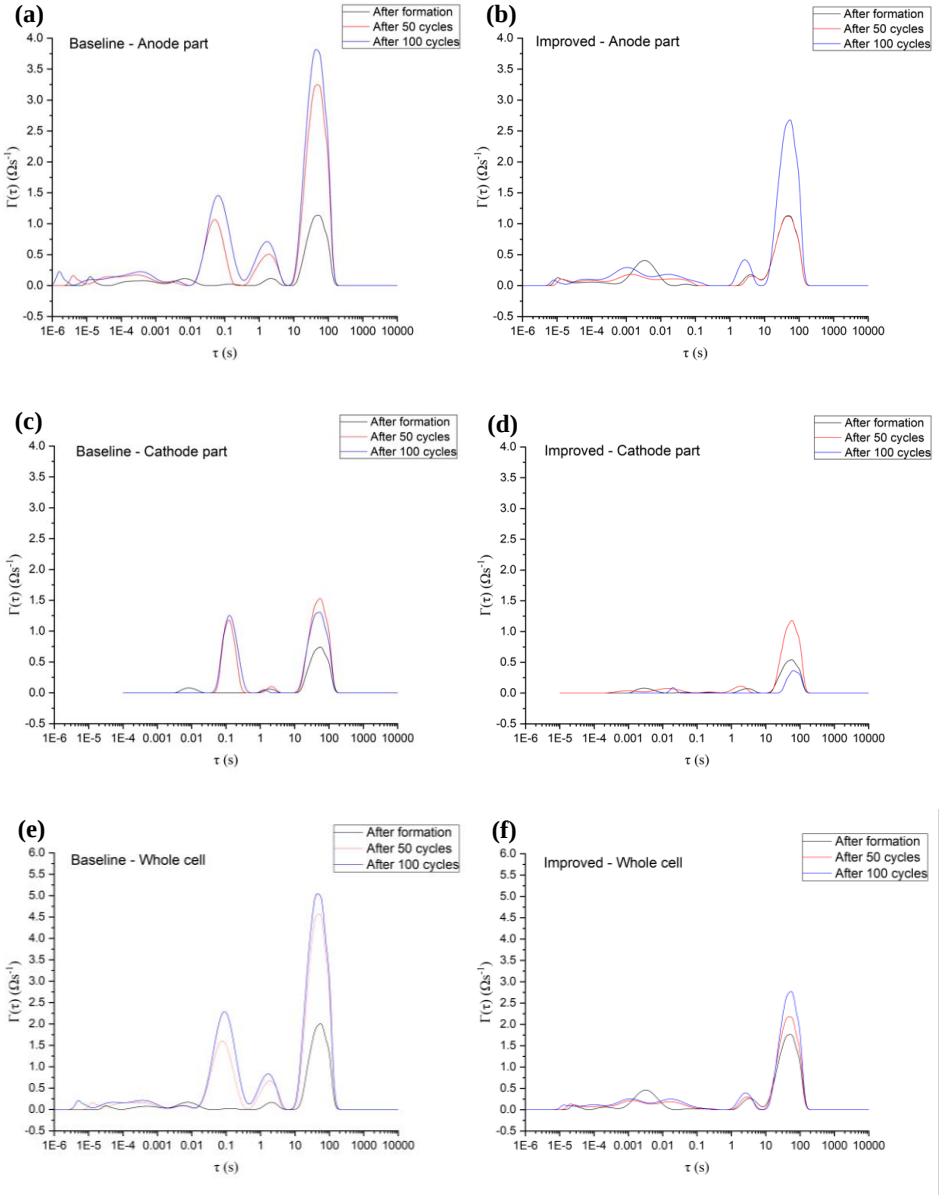

Figure 2-8. DRT at different state of aging. (a) baseline anode, (b) improved anode, (c) baseline cathode, (d) improved cathode, (e) baseline whole cell, (f) improved whole cell.

It has been common wisdom that a strong and dense SEI is required at high temperature to effectively prevent electrolyte decomposition [30]. However, such a SEI is not suitable at low temperature. Therefore, it has been a challenge to develop an SEI layer with a wide spectrum of temperature. In this paper, we tried to shed light on the issue by the comparison of the electrochemical kinetics of both diffusion and charge transfer processes across the SEIs in both baseline and improved electrolytes.

In order to analyze the difference of the electrochemical processes between the two electrolytes, impedance spectrum in a frequency domain was transferred into a time domain. The result of the transformation is presented as the DRT shown in Figure 2-8. Figure 2-8(a, b) compare the anodes DRTs of the two cells after formation cycles, after 50 cycles at 60°C, and after 100 cycles at 60°C respectively. Figure 2-8(c, d) show the cathodes DRTs of the two cells at different state of aging. The whole cell DRTs of the two cells are exhibited in Figure 2-8(e, f). Starting with the DRTs that were taken after the formation, four peaks for the anode and three peaks for the cathode can be clearly observed. The whole cell DRT was the superposition of the anode DRT and the cathode DRT. A peak in DRT represents one RC element in a transmission line circuit and reflects one electrochemical process of the electrode. Note that the horizontal position of a DRT peak was the relaxation time of the RC element, which represented the kinetics of the corresponding electrochemical process.

In Figure 2-8(a, b), the anode DRT peaks at $\tau = 10^{-5}$ s indicate the charge transfer reaction at the anode and the SEI interface. It is evident in Figure 2-8(a, b) that the peaks at $\tau = 10^{-5}$ s were independent of the state of aging or the type of the electrolyte used. The peak at

around $\tau = 10^2$ s represented the Li ion diffusion within the bulk anode, which was considered as a process with the lowest kinetics. Finally, the peaks at $\tau = 10^{-2}$ s and $\tau = 10^0$ s represented Li ions passing through the SEI and the interface of the SEI and the electrolyte, respectively.

Figure 2-8(a, b) show that the major difference on the anode between the baseline cell and the improved cell after the formation happens at $\tau = 10^{-2}$ s. The improved electrolyte had a higher peak representing the higher resistance for Li ions passing through the SEI. This difference revealed that the improved electrolyte generated a different SEI from that of the baseline; possibly a denser SEI formed in the improved electrolyte than that in the baseline electrolyte. Also, no significant difference on the other peaks indicated that, other than the SEI, the two electrolytes may play the same role on the anode part after the formation of the cell. As the cells completing 50 cycles and 100 cycles at high temperature, it was found that the anode peaks of the baseline cell at $\tau = 10^{-2}$ s, $\tau = 10^0$ s, and $\tau = 10^2$ s were gradually and significantly increased while those of the improved cell remained relatively unchanged. Clearly the resistances of the SEI and the graphite anode in the baseline cell became larger than those in the improved cell. Apparently, the increase of the resistance resulted from the continuous chemical reaction between the graphite anode and the baseline electrolyte, while such a reaction was hindered in the improved electrolyte. The hypothesis was at least partially proven with the evidence that a denser SEI was formed in the improved electrolyte after the formation. The continuous reaction of the baseline electrolyte was consistent with the evidence that its capacity decay during the cycling at 60°C was faster than that of the improved electrolyte.

In order to understand the physical changes on the anode during the cycles, a detailed observation from Figure 2-8(a, b) was that, in the baseline cell, the peaks at $\tau = 10^{-2}$ s grow nearly four times after 50 cycles and nearly five times after 100 cycles. Moreover, the peaks at $\tau = 10^{-2}$ s in baseline cell shift to a higher relaxation time during the cycling. However, there was no significant increasing nor shifting of the $\tau = 10^{-2}$ s peak for the improved cell. Evidentially, in the baseline cell, the SEI continued growing during the high temperature cycles, causing a resistance increase and a decrease of the Li ion diffusion kinetics. In the improved cell, however, thanks to the dense SEI formed during the formation, despite its lower initial capacity owing to the relative higher SEI resistance against the baseline, the improved electrolyte outperformed the control during a prolong cycles. The superior cycle performance of the improved electrolyte at 60°C could be attributed to the effective protection of the SEI preventing the anode from further reaction with the electrolyte. The conclusion is consistent with the previous results that Li inventory loss was the main cause for the capacity loss and most of the Li was consumed on a graphite anode [81].

As shown in Figure 2-8(a, b), the $\tau = 10^{2}$ s peaks of the baseline cell grew three times from 1 Ω/s to 3.5 Ω/s during the first 50 cycles and reached about 4 Ω/s at 100 cycles. For the improved cell, however, the $\tau = 10^{2}$ s peaks did not change at all during the first 50 cycles, and they only grew from 1 Ω/s to 2.8 Ω/s at 100 cycles. Assuming that the peak at $\tau = 10^{2}$ s represented the Li diffusion in the graphite anode, the growth of $\tau = 10^{2}$ s peak meant the decrease of the kinetics of the Li diffusion in the graphite layers. It is natural that the graphite material degraded along the cycle especially at high temperature [82], [83]. Evidentially a dense

and strong SEI may protect a graphite anode degradation causing by, e.g., a solvent co-insertion. In the baseline cell, the loosened SEI may not shield the anode from the electrolyte at a high temperature. Therefore, the solvent molecules in the electrolyte could become decomposed on and co-intercalated into the anode at the very beginning of the high temperature cycles. The permeation of the solvent molecules into the graphite layer would block the lithium diffusion or damage the graphite layer structure, and both would impede the Li diffusion near the interface. In the improved cell, the dense SEI provided better protection to the anode by preventing the solvent from reaching the graphite anode. Therefore, the initial performance of the improved cell was compromised for long term cyclability.

The cathode DRTs are shown in Figure 2-8(c, d). The cathode DRTs in both electrolytes were similar at room temperature. The intensity of the cathode peaks was in the same order of magnitude to that of anode. Both electrodes contribute similarly to the impedance of the cell at ambient temperature. The conclusion is consistent with what we presented previously. After cycling at elevated temperature, however, a new peak at $\tau = 10^{-1}$ s started to merge and eventually became a major peak for the cathode in the baseline electrolyte. In the improved electrolyte, the peak at $\tau = 10^{-1}$ s did not show up after 100 cycles at 60°C. The peak around $\tau = 10^{0}$ s increased in both electrolytes when cycling at 60°C, but it increased faster and reached a higher value in the baseline electrolyte. It is worth mentioning that, as presented in this chapter, at -20°C the DRT contribution from the cathode can be ignored and the cell kinetics were determined by the anode impedance. As shown in Figure 2-8, although the impedance of the anode still makes a major contribution to the cell impedance at an elevated

temperature, at least in the baseline electrolyte, the cathode contribution cannot be overlooked. Even though additional studies are in progress to understand the cathode process at elevated temperatures, it is evident that the oxidation nature of the cathode activated material could be magnified at an elevated temperature and played an important role in the impedance increase.

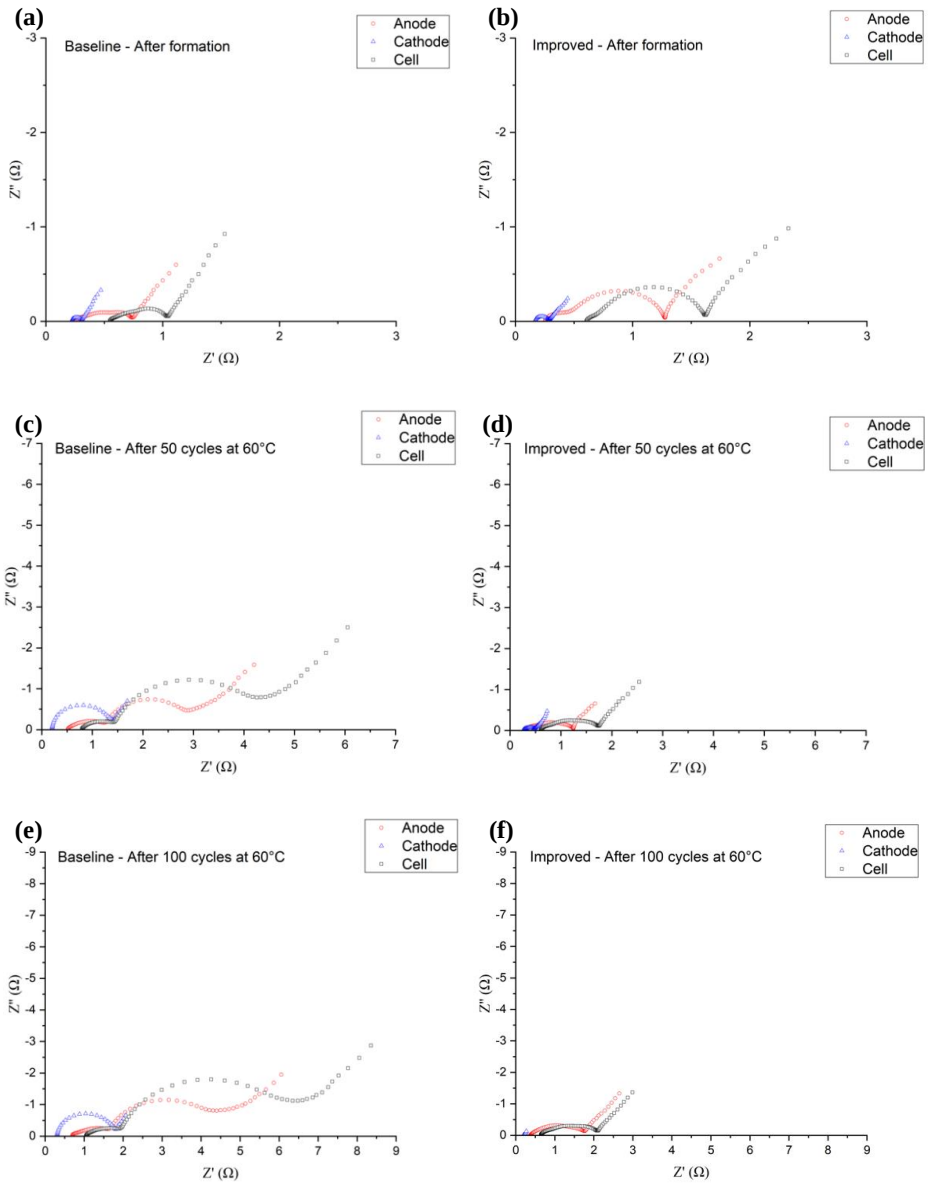

Figure 2-9. EIS on the three electrodes separately. (a) baseline after formation, (b) improved after formation, (c) baseline after 50 cycles at 60°C, (d) improved after 50 cycles at 60°C, (e) baseline after 100 cycles at 60°C, (f) improved after 100 cycles at 60°C.

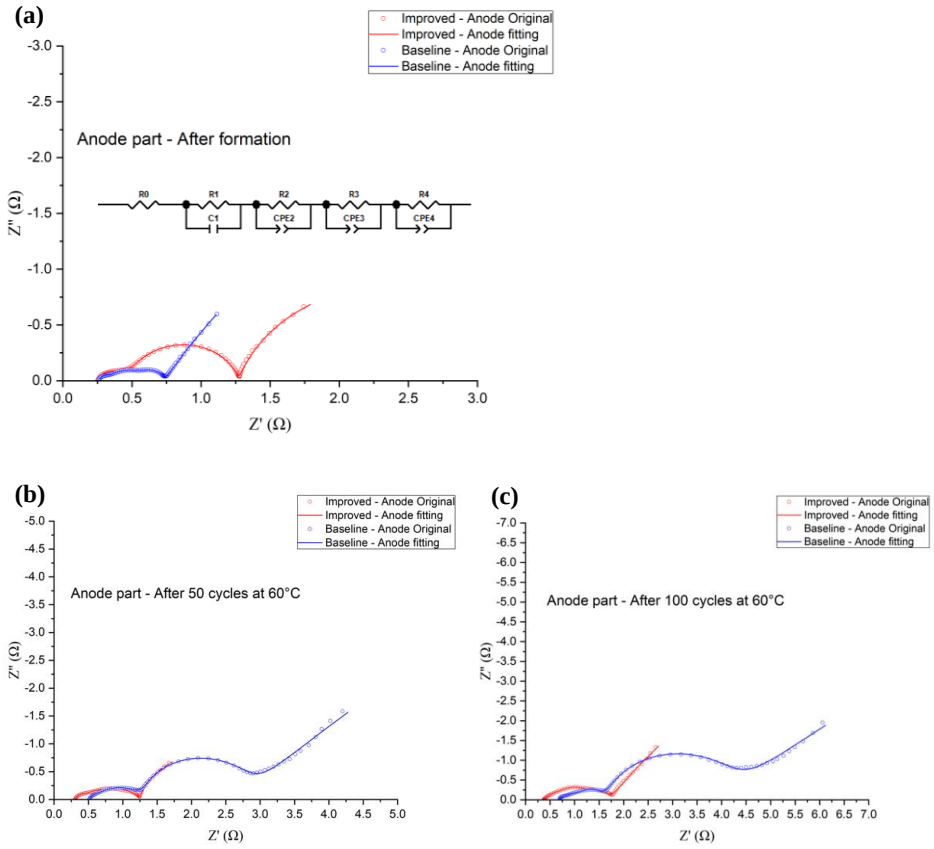

Figure 2-10. Equivalent circuit fitting on the anode part EIS. (a) after formation and the model of the equivalent circuit, (b) after 50 cycles at 60°C, (c) after 100 cycles at 60°C.

Table 2-2. Equivalent circuit simulation results.

Sample	State	R_0	R_1	C_1	R_2	CPE_2-T	CPE_2-P	R_3	CPE_3-T	CPE_3-P	R_4	CPE_4-T	CPE_4-P
Baseline	After formation	0.261	0.059	1.7e-4	0.263	0.014	0.701	0.150	0.071	0.907	9.794	9.0	0.679
	After 50 cycles	0.511	0.062	8.2e-5	0.718	0.004	0.647	1.431	0.043	0.929	37.69	1.7	0.528
	After 100 cycles	0.641	0.225	1.3e-3	0.802	0.014	0.452	2.372	0.039	0.884	50.53	1.2	0.488
Improved	After formation	0.258	0.104	1.2e-4	0.125	0.002	0.864	0.783	0.009	0.865	2.271	9.4	0.783
	After 50 cycles	0.307	0.097	2.4e-4	0.583	0.023	0.612	0.265	0.149	0.719	2.058	11.1	0.866
	After 100 cycles	0.364	0.302	3.7e-3	0.572	0.010	0.610	0.477	0.057	0.818	19.82	3.3	0.641

Figure 2-9 shows the impedance spectra used for the DRT transforms. Figure 2-9(a, b) show the impedance spectra of the cathode, the anode and the cell of the baseline cell and the improved cell after formation, respectively. Figure 2-9(c, d) present those after 50 cycles at 60°C, and Figure 2-9(e, f) exhibit those after 100 cycles at 60°C. Based on the DRT of the anode, as discussed extensively above, an equivalent circuit was built up to simulate the anode EIS and facilitate a quantitative analysis.

The fitting results for the anode EIS are presented in Figure 2-10, and the fitting parameters are tabulated in Table 2-2. The equivalent circuit used for the anode fitting is shown as an insert in Figure 2-10(a). In the equivalent circuit, the CPE was used as a non-ideal capacitor to simulate a porous electrode with a rough surface or interface [50]. In the equivalent circuit shown in Figure 2-10(a), R_0 represents the ohmic resistance of the electrolyte, the current collector and the contact resistance; the C_1/R_1 relates to a charge transfer reaction; CPE_2/R_2 simulates the Li ion crossover the electrolyte/SEI interface; CPE_3/R_3 represents the Li ion diffusion through the SEI, while CPE_4/R_4 is used to simulate Li ion diffusion in the bulk anode. As shown in Table 2-2, after formation, the R_3 value in the improved cell is 5 times higher than that in the baseline cell, while the CPE_3-T value in the improved cell is 7 times smaller than that in the baseline cell. The CPE-T can be considered as a capacitance component of a non-ideal capacitor. The higher the CPE-T value normally means the higher the surface area of an electrode, which indicates the high porosity of an electrode. Therefore, the improved anode seemed to have a low porosity SEI and a high resistance. The conclusions agree well with the speculation that a dense SEI was formed on

the anode in the improved electrolyte. As a result, in the baseline cell, R_3 increases 9 times after 50 cycles at 60°C and 15 times after 100 cycles at 60°C, but R_3 of the improved cell retained its original value after 100 cycles at 60°C. The results indicated a more substantial growth of the SEI in the baseline cell than in the improved cell. A comparison between the anodes EIS fitting results in Table 2-2 and the anodes DRT peaks in Figure 2-8(a, b) exhibited that the values of the CPE_3/R_3 matched the area of the peaks at $\tau = 10^{-2}$ s correspondingly, which both represented the Li ion diffusion in the SEI. Therefore, it was not supervising the EIS fitting results yielded to a same prediction as the DRT analysis, but in a quantitative aspect. Furthermore, both R_2 and R_4 values were higher and growing faster along the cycles in the baseline cell than in the improved cell, which was also evident that a dense SEI in the improved cell can protect the anode during the high temperature cycles.

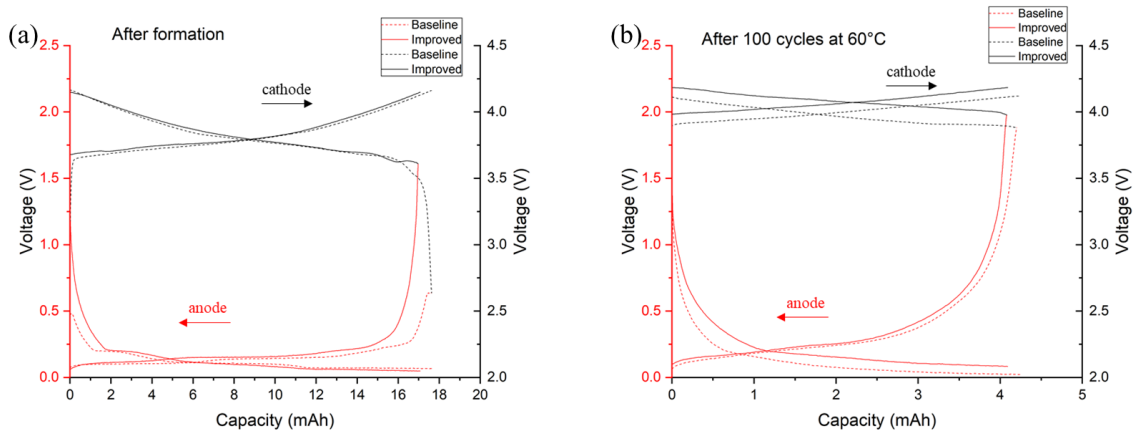

Figure 2-11. Anode and cathode separate charge/discharge for 1 cycle at 0.1C rate at room temperature (a) after formation, (b) after 100 cycles at 60°C.

Figure 2-11(a) compares the charge/discharge curves of the separate anodes and cathodes between the baseline and the improved cells before cycles. In Figure 2-11(a), the plateaus of the two cells were almost overlapped for both the anode and the cathode, except the polarization sections at the end of discharge and at the beginning of charge. At the end of discharge, it can be observed that the anode in the improved cell polarized slightly earlier than that in the baseline cell, which caused the cathode in the improved cell not fully discharged. As a result, it corresponded to the phenomenon where the improved cell had inferior capacity compared to the baseline cell in the first 20 cycles at 60°C. A high resistance on the anode was a reasonable explanation on its early polarization, which is consistent with the observation of the high SEI impedance peak in the DRT discussions. Therefore, this observation yields the same hypothesis that a denser SEI may form on the anode surface with the improved electrolyte.

Figure 2-11(b) compares the same electrodes after 100 cycles at 60°C. No polarization could be observed on the cathode charge/discharge curves either in the baseline or in the improved cell, which indicated the state of the cathodes were far from fully charged or discharged during the cycles. On the contrary, the polarization on the anode side revealed that the anode was the capacity limitation for the full cell after elevated temperature cycles. An anode charging curve comparison between the baseline and the improved cells showed that the potential of the baseline anode rapidly dropped below 0.15 V at the beginning of charge. However, the improved anode could maintain its potential around 0.20 V for a while during charging. The high overpotential on the baseline anode during charging indicated high

resistance as lithium intercalated into the anode, thus explained the reason that the baseline cell underperformed after 60 cycles at elevated temperature, although it presented a similar capacity to the improved cell at room temperature in Figure 2-11(b). Since high resistance causing high overpotential, it mirrored the high SEI impedance growth on the anode in DRT graph and EIS simulation and became a support for the hypothesis that the SEI grew faster in the cell with the baseline electrolyte.

2.3.3. Conclusion

The electrolyte with a proven low temperature rate performance was investigated against the state-of-art electrolyte at 60°C. A small but significant performance advantage was demonstrated in the improved electrolyte. The EIS and DRT transforms results revealed that a denser SEI layer was formed in the improved electrolyte. Therefore, further anode electrolyte and/or cathode electrolyte reactions were either delayed or reduced in the improved electrolyte. Although the denser SEI in the improved electrolyte compromised the initial performance of the improved electrolyte at 60°C, its benefit started to emerge after about 50 cycles.

2.4. Summary

This chapter gives the fundamental EIS investigations for LIB. A traditional electrolyte was compared with a wide temperature improved electrolyte. The three-electrode pouch cell was the key to support the EIS measurement, since the impedance contributions of the anode and the cathode can be separated. Through the DRT transformation and the EIS fitting, plenty

evidence indicated that the improved performance related to a dense homogeneously formed SEI.

In the future, the work will provide instruction on investigating the components of the different SEIs on different electrode material with EIS. More comparisons of EIS behaviors on different batteries will be conducted to further understand how different SEIs affect an LIB. Then, it will be applied on analyzing the SEI differences between chemical prelithiation and the electrochemical lithiation in the following chapter.

CHAPTER 3. PRELITHIATION OF CARBON AND SILICON-BASED ANODE WITH LITHIUM CONTAINING SOLUTION METHOD

3.1. Introduction

After establishing EIS tool for analyzing the electrode surface. The details of the prelithiation method we applied will be introduced in this chapter. The prelithiation with lithium containing solution method relies on the choice of the prelithiation reagent. To make the process happen simultaneously, the thermodynamic driving force is the redox potential. Given the unique redox potential during lithiation for a specific anode material, the redox potential of the prelithiation reagent has to be lower than the lithiation potential of the anode, so that the anode material can be reduced and be lithiated at the meantime. It has been mentioned in Chapter 1 that an aromatic hydrocarbon dissolved in an organic solvent owns the low redox potential property. It has been tested that different aromatic hydrocarbon with different organic solvent exhibit slightly varying redox potential. The distinguished potential plays the key roles when prelithiate different anode materials, especially those with low lithiation potential [84].

This chapter will present lithium containing solution prelithiation in details for a HC anode and a SiO anode respectively.

In order to prelithiate a target anode material using lithium containing solution method, a cyclic voltammetry (CV) was conducted for various prelithiation reagent before any electrode treatment, using an Autolab PGSTAT30 potentiostat/galvanostat electrochemical system with a potential range of 0.01~2 V (vs. Li^+/Li). A galvanic cell was assembled in a three-neck flask

with a glass carbon anode, a lithium metal cathode and a lithium metal reference. The electrolyte was prepared as 1.0 M $LiPF_6$ with 0.01 M target aromatic hydrocarbon in target organic solvent.

3.2. Prelithiation of hard carbon anode

Although graphite has long served as the anode material for LIBs thanks to its high coulombic efficiency, and good cycling performance, the limited specific capacity and relatively poor rate capability of graphite cannot satisfy the increasing demand of high-energy and high-power LIBs. As one of the potential alternatives, non-graphitizable HC is of great interest for its high capacity and better rate performance.

It is generally accepted that the higher capacity of HC comes from the random arrangement of single graphene layers, which provides extra voids to accommodate lithium [85], [86]. However, its practical application is hindered by a large irreversible capacity and thus low ICE (<80%), which originates from the relatively large surface area, causing SEI formation and side reaction between lithium ions and surface functional groups [87]. Several strategies have been investigated to solve this issue, and prelithiation has been proved to be one of the most effective methods [61], [88]. The lithium containing solution was selected as the prelithiation method for HC anode, since the operation is rather simple and shows great potential for industrial application with a suitable roll-to-roll design.

Biphenyl (Bp) in tetrahydrofuran (THF) is one of the aromatic hydrocarbon solutions that can oxidize the lithium [66]. The CV results in Figure 3-1(a) indicates the Li–Bp–THF owns a low redox potential of ~0.4 V. Then, Figure 3-1(b) shows the HC materials possess a

slope lithiation potential from ~1 V to 0.2 V. Therefore, the Li–Bp–THF is expected to prelithiate the HC and ideally takes care of the lithiation capacity above ~0.4V.

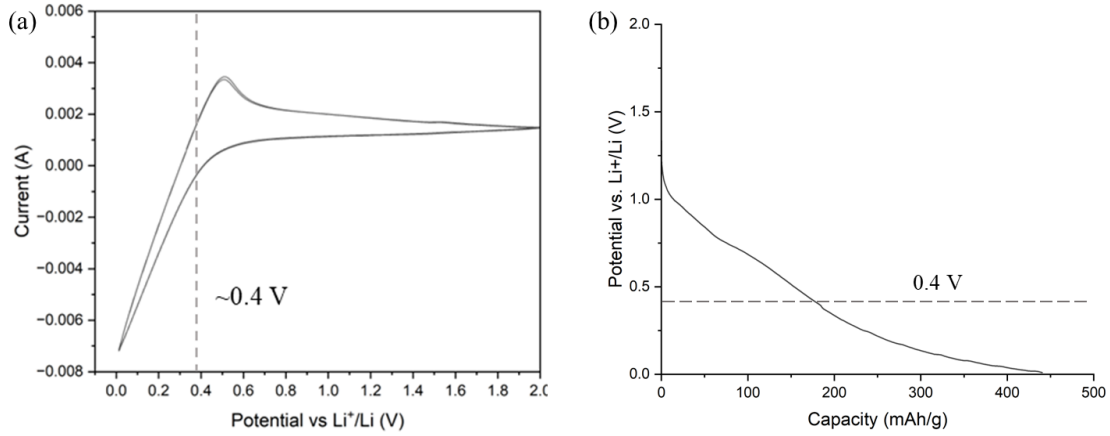

Figure 3-1. (a) CV of Bp^{-}/Bp in 1 M $LiPF_6$ electrolyte (THF as solvent) at 50 mV/s; (b) first lithiation curve of a hard carbon anode in half-cell.

3.2.1. Experiment details

Materials

Commercial HC powder was provided by BTR New Energy Materials Co., China. Biphenyl was purchased from Sigma-Aldrich, and vacuum dried at 60°C overnight before use. All other chemicals were of analytical grade and used as received.

Prelithiation Reagents Preparation

Certain amount of Bp was dissolved in THF to make a 1.0 M Bp–THF solution. Then, an excess amount of lithium metal was added in the solution and reacted overnight to prepare 1.0 M Li–Bp–THF solution. Once the Li metal was added, the solution turned a dark blue-green color. The prelithiation reagent is usually prepared fresh before use.

Material Characterization

The morphologies of the samples were characterized using the Hitachi S-4800 field emission scanning electron microscope. XPS were recorded using the Perkin-Elmer PHI 5400 ESCA System. The binding energy scale was calibrated from the C 1s peak at 284.8 eV (C–C/C–H). Half cells at different discharging and charging states were disassembled in an argon glovebox to obtain electrode samples. Each electrode piece was rinsed with DMC to remove any residual lithium salt. After drying, the electrodes were mounted on XPS or scanning electron microscope (SEM) sample holders using conductive carbon tape. Electrodes were stored in sealed containers in the argon-filled glovebox prior to XPS or SEM analysis and moved from the glovebox to the XPS or SEM system with less than 30 s exposure time to air. Inductively coupled plasma-atomic emission spectrophotometry (ICP-OES) measurements

were carried out on a Perkin–Elmer Optima 2100 DV ICP-OES apparatus to determine the lithium amount in the prelithiated electrodes. After prelithiated for certain time, the electrodes were immersed into *n*-methyl-2-pyrrolidone (NMP) solvent and subject to ultrasonic method to remove the active materials from current collectors. Then the particles were dissolved into concentrated HNO_3 solution at 80°C and diluted before test. The calibration curve of Li concentration for ICP-OES analysis is shown in Figure 3-2.

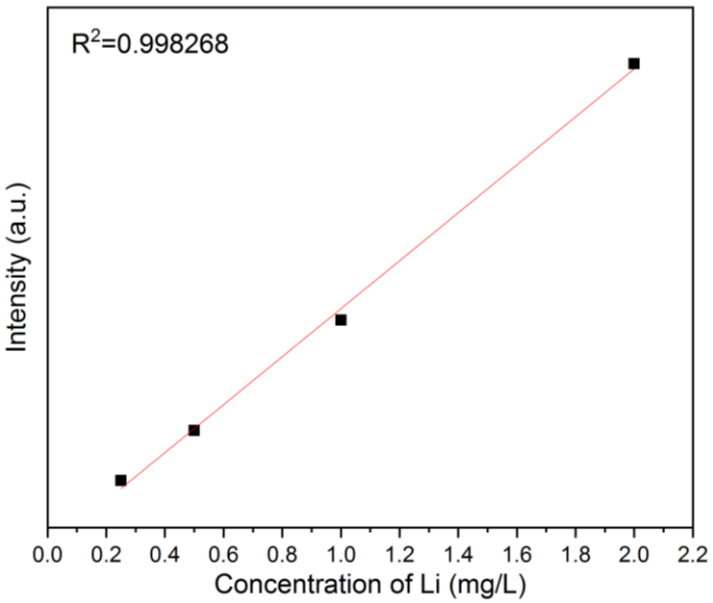

Figure 3-2. The calibration curve of Li as determined by the ICP-OES method.

Electrode Fabrication and Battery Test

A slurry of HC powder, super C65, and poly(vinyl difluoride) (PVDF) at a weight ratio of 94:3:3 was coated onto a carbon-coated copper foil to prepare the working electrode, and vacuum dried at 120°C overnight. A prelithiated HC electrode was prepared by immersing the pristine HC electrode into the prelithiation reagent for different time (30 s, 2 min, 5 min, 10 min and 1 h), followed by washing with THF and vacuum-drying to remove residual Bp and solvent. PreLi-30s, PreLi-2min, and PreLi-5min represented the HC electrode immersed in Li–Bp–THF solution for 30 s, 2 min, and 5 min, respectively. Full cells were made with NMC 111 as the positive electrode and HC as the negative electrode. The NMC 111 electrode formulation was 92% active material (Umicore), 5% super C65, and 3% PVDF binder by weight. Typical mass loading of active material was 3~4 mg/cm^2 for the HC anode and 6~7 mg/cm^2 for the NMC 111 cathode.

The electrochemical characterization was carried out using 2032 coin cells assembled in an argon-filled glove box (H_2O < 0.5 ppm, O_2 < 1 ppm). The Li-ion half-cell consisted of a lithium metal anode, a Celgard 2325 separator, and the prepared working electrode. The electrolyte was 1.0 M $LiPF_6$ dissolved in EC and EMC solvent (3:7 mass ratio). Galvanostatic charging/discharging tests were conducted on an Arbin battery testing system (BT2000) at room temperature. The voltage windows for HC/Li half-cell and HC/NMC 111 full cell were 0.01~2 V and 2.5~4.1 V respectively. In order to evaluate the prelithiation efficiency, a prelithiated HC electrode was first reduced electrochemically in a half cell and then oxidized to determine the reversible Li insertion. The ICE of a prelithiated HC electrode can be

determined by the ratio of first oxidation capacity and first reduction capacity. The capacity of the reversible Li in the electrode through the prelithiation can also be determined directly by first oxidizing a prelithiated HC electrode. In this case, the ICE of a prelithiated HC electrode can be calculated by the ratio of second oxidation capacity and first reduction capacity. The reversible capacities of the cathode and the anode were measured in half-cell geometry, which were used for the determination of full cell balance. The cycling performance of half cells were conducted at 1C (1C = 300 mAh/g) discharge/charge rate for 100 cycles. In a full cell assembly, the size of HC and NMC electrodes were 5/8 inch and 9/16 inch outer diameter (OD), respectively. The reversible capacity of negative to positive electrodes (N/P ratio) was ~1.1. Following the formation cycles (2 cycles at C/20 and 3 cycles at C/10), the cells were cycled at 1C for another 200 cycles. The rate capability of half and full cells was tested at 1C, 2C, and 5C for 10 cycles each, and back to 0.1C for 3 cycles. For full-cell formation and cycling tests, the voltage window was 2~4.1 V. A three-electrode cell was used for the ac impedance measurement, in which Li foil and a Li ring were used as the counter electrode and reference electrode, respectively. Measurements were conducted using an Autolab PGSTAT30 potentiostat/galvanostat electrochemical system (Metrohm). The frequency range was from 0.1 Hz to 10^6 Hz with a perturbation amplitude of 5 mV. Spectra were recorded at the end of selected charge/discharge states.

3.2.2. Results and discussions

The SEM images of pristine HC electrodes in Figure 3-3(a, b) show sphere-like particle shapes, with a particle size range of 5~15 μm. After prelithiation, the void at the surface area

was filled up shown in Figure 3-3(f, j, n), which may be ascribed to the volume expansion from lithiation, and SEI preformed during prelithiation. In order to explore the effect of prelithiation on the surface chemistry of HC, the pristine and prelithiated electrodes were immersed in the electrolyte for 24 h. No obvious change was observed in the pristine HC in Figure 3-3(c, d), while the prelithiated HC exhibited a denser surface, indicating an SEI reconstruction when contacted with electrolyte. After the 1st discharge/charge cycling, the shape of the pristine HC is retained as shown in Figure 3-4(a, b), whereas the surface texture of the cycled electrode is different from that of the pristine one, with some small particles on the surface. After formation, Figure 3-4(c, d) show that a smooth SEI film was formed on the surfaces of the HC agglomerates. For the prelithiated electrodes, a smoother surface texture after delithiation was observed compared with the electrochemically cycled electrode. The pristine and prelithiated HC showed similar surface morphology after the formation process.

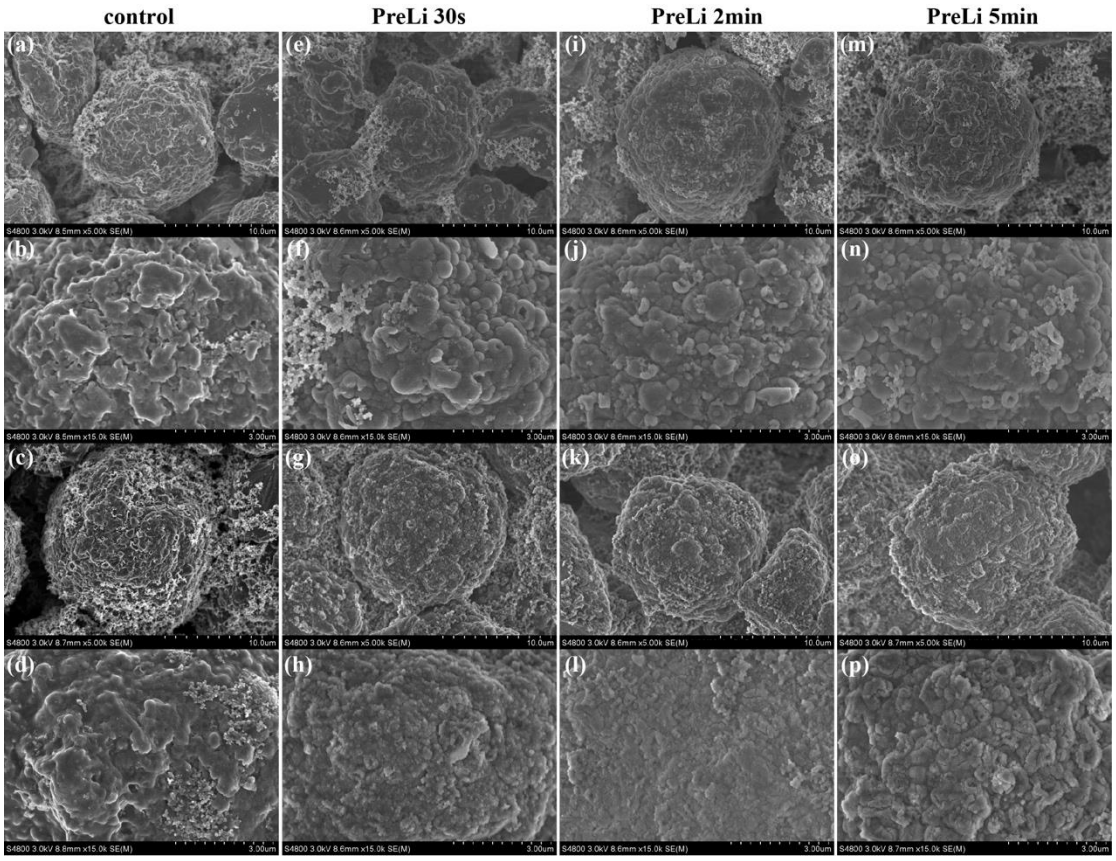

Figure 3-3. SEM images of pristine HC electrode (a, b) and after immersion in electrolyte for 24 h (c, d); PreLi-30s before (e, f) and after (g, h) immersion in electrolyte for 24 h; PreLi-2min before (i, j) and after (k, l) immersion in electrolyte for 24 h; and PreLi-5min before (m, n) and after (o, p) immersion in electrolyte for 24 h.

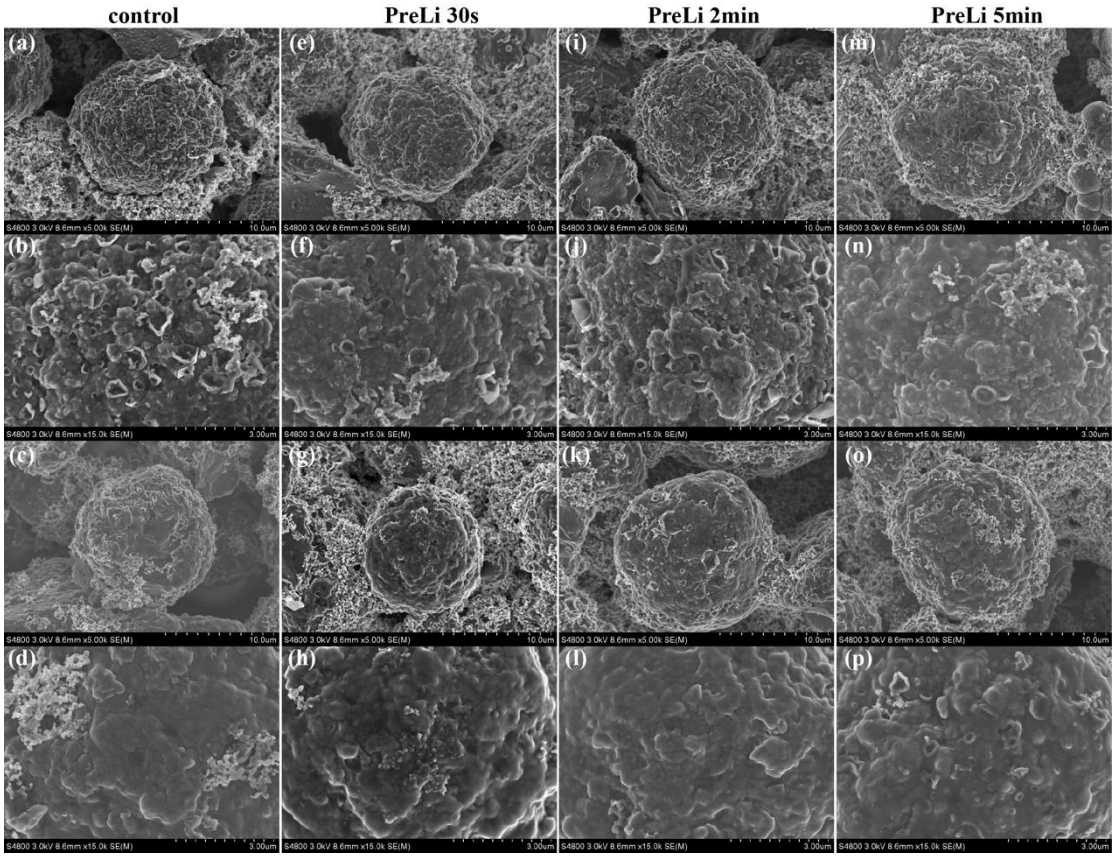

Figure 3-4. SEM images of pristine HC electrode after 1st cycle (a, b) and formation (c, d); PreLi-30s after 1st delithiation (e, f) and formation (g, h); PreLi-2min after 1st delithiation (i, j) and formation (k, l); PreLi-5min after 1st delithiation (m, n) and formation (o, p).

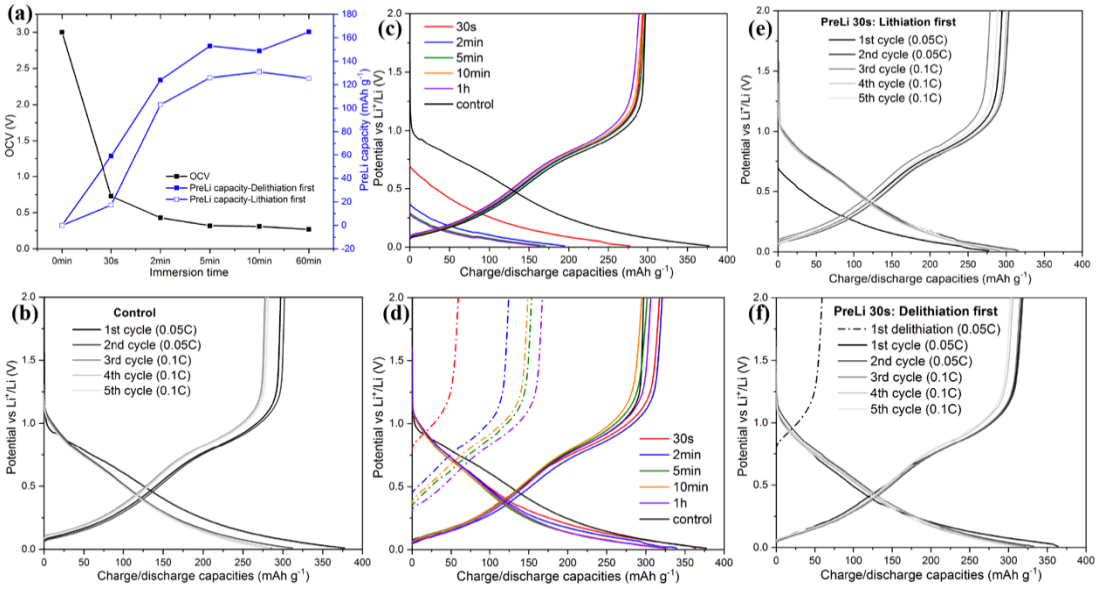

Figure 3-5. (a) OCV values and PreLi capacities of HC electrodes with different prelithiation time; (b) Discharge and charge curves of the formation process of control electrodes in half cells; 1st discharge/charge curves started from lithiation (c) and delithiation (d) of HC electrodes with different prelithiation time; Discharge and charge curves of formation process started from lithiation (e) and delithiation (f) of PreLi-30s electrode in half cells.

Table 3-1. Data summary of electrochemical performance of different samples.

Samples	Lithiation first				Delithiation first				
	A: 1st Lithiation capacity (mAh/g)	B: 1st DeLi capacity (mAh/g)	PreLi capacity (=B-A) (mAh/g)	CE_{avg} (=B/A) (%)	a: 1st DeLi capacity (mAh/g)	b: 1st Lithiation capacity (mAh/g)	c: 2nd DeLi capacity (mAh/g)	PreLi capacity (=a) (mAh/g)	CE_{avg} (=c/b) (%)
Control	377.4	297.1	--	79.2±1.9	--	--	--	--	--
30s	277.2	294.5	17.3	104.4±2.2	59	363.8	317.3	59	87.6±1.7
2min	194.5	297.5	103	145.2±6.8	124.2	339.7	320.8	124.2	91.2±1.6
5min	170.8	296.7	125.9	179.8±8.6	153	325.1	301.7	153	89.9±2.3
10min	162.1	293	130.9	186.8±8.4	148.8	327.7	294.8	148.8	89.9±0.9
1h	163.8	289.2	125.4	172.9±5.1	167.4	325.3	306.2	167.4	92.6±3.2

Figure 3-5(a) shows the open circuit voltage (OCV) of a half-cell after resting for 24 h. The pristine HC half-cell exhibited an OCV of ~2.9 V vs Li^+/Li while the prelithiated ones showed OCV decreasing with the immersion time increasing, which indicated that more Li ions were inserted chemically into the HC electrode. The OCV can drop down to ~0.7 V after a very short immersion time of 30 s, and stabilized at ~0.3 V after 5 min.

The electrochemical performance of pristine and prelithiated electrodes in a half cell construction is shown in Figure 3-5(b – f) and Table 3-1. The first reduction (lithiation) and oxidation (delithiation) capacities of the pristine electrode were 377.4 and 297.1 mAh/g, respectively, indicating a large irreversible capacity of ~80 mAh/g and an ICE of only 78.7%. Two different electrochemical tests were conducted for the prelithiated HC half cells, that is, lithiation first and delithiation first. In the lithiation first case, while reversible oxidation (delithiation) capacities remained almost the same as the pristine sample, the reduction (lithiation) capacity was gradually decreased with the immersion time increasing shown in Figure 3-5(c), which was consistent with the trend of OCV values. Specifically, the PreLi-30s, which stands for 30 sec of prelithiation, electrode delivered a reduction (lithiation) capacity of 277.2 mAh/g and an oxidation (delithiation) capacity of 294.5 mAh/g, leading to a high ICE of ~106.2%. The maximum oxidation (delithiation) capacity of ~130 mAh/g (~44% of reversible capacity) after prelithiation was obtained after 10 min immersion and the unprelithiated part may result from the lower lithiation voltage region of HC. When the prelithiated HC was oxidized (delithiation) first, the oxidation (delithiation) capacities were increased with the immersion time increasing and stabilized after 10 min immersion. In this

case, the ICE of the prelithiated electrodes showed an increasing trend for prelithiation time from 30 s to 2 min. With prolonged time, no obvious increase of ICE is observed. Even with a short time of 30 s, the ICE had already reached ~88%. The difference of the prelithiation capacities in the two cases indicated that an artificial and incomplete SEI was chemically formed during prelithiation. The slightly different delithiation capacity (1st delithiation capacity in lithiation first process and the 2nd delithiation capacity in delithiation first process) may come from the different SEI formation process of the two methods, where delithiation first leads to more electrochemically formed SEI. With lithiation first, some chemically preloaded lithium may be trapped and not be delithiated in the following cycle. After the formation process, the reversible capacities of the pristine and PreLi-30s electrodes at 0.1C were 281.5 and 288.7 mAh/g, respectively. The cycling performance of the HC electrodes in half cells were tested as shown in Figure 3-6. The two methods have no obvious effect on the cycling performance. All the cells exhibited a slightly increased capacity in the first several cycles and stabilized later. The half cells with delithiation first showed a slightly better capacity retention after cycling at 1C for 100 cycles, which may be ascribed to the slightly different SEI of the two methods as stated above.

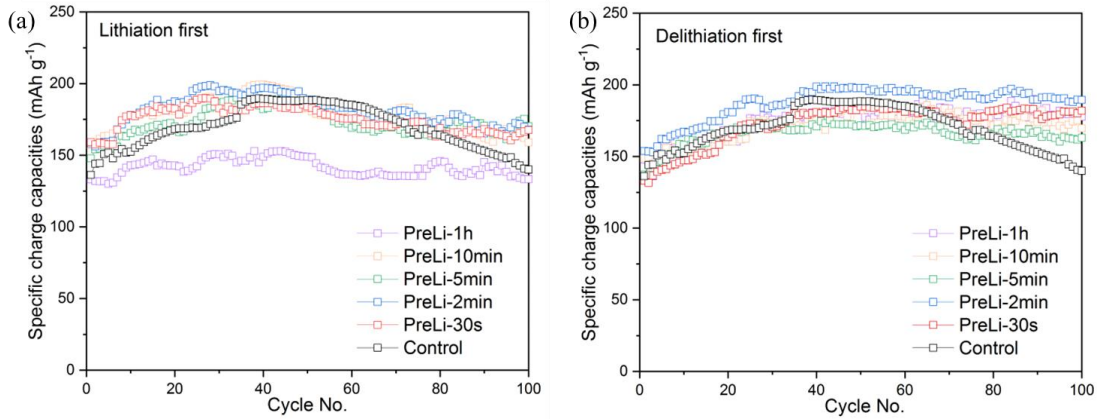

Figure 3-6. Cycling performance of pristine and prelithiated HC electrodes in half cell format at 1C with (a) lithiation first; (b) Delithiation first.

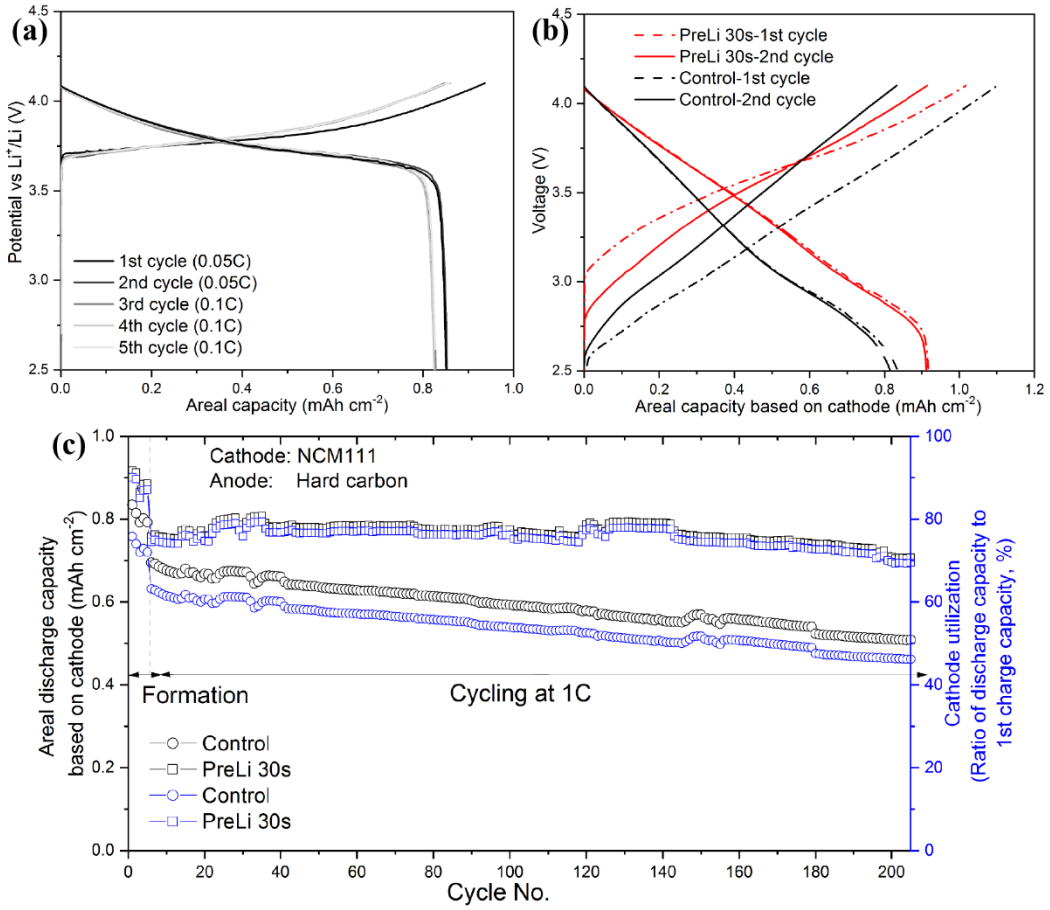

Figure 3-7. (a) Charge/discharge curves of NCM111 electrode in half cells; 1st and 2nd charge/discharge voltage curves (b) and cycling performances (c) of full cells with pristine HC anode and PreLi-30s HC anode.

The content of Li in hard carbon anodes for PreLi-30s, PreLi-2min, and PreLi-5min have been tested using ICP-OES. The Li content of PreLi-30s, PreLi-2min, and PreLi-5min was determined to be 0.0163, 0.0347, and 0.0457 mg(Li)/mg(C), respectively. The increasing trend is consistent with the increasing delithiation capacity result. Meanwhile, based on the 1st delithiation capacity results (59, 124.2, and 153 mAh/g for PreLi-30s, PreLi-2min, and PreLi-5min, respectively), we can calculate that the prelithiated and active Li content in the HC matrix for PreLi-30s, PreLi-2min, and PreLi-5min was 0.0153, 0.0322, and 0.0396 mg(Li)/mg(C), respectively. The slightly higher Li content in the ICP test comes from the Li content in the SEI layer, which was extracted during the sample prepare process.

In a full cell test, a commercial NMC 111 was chosen as the cathode material. As the matched cathode is NMC 111 with full lithium content, only the charging first method is applied in the full cell test. This formation step was contradicted to a lithium-free cathode (e.g., V_2O_5, S) which needs to be discharged first with a prelithiated anode. The first areal oxidation and reduction capacities of NMC 111 were 0.95 and 0.85 mAh/cm^2, respectively as shown in Figure 3-7(a). Since the HC anode was prelithiated, the OCV of the prelithiated full cells were about ~2 V. When paired with the pristine HC anode, the full cell exhibited an initial areal charge capacity of 1.1 mAh/cm^2 (cathode area) and discharge capacity of 0.83 mAh/cm^2 (cathode area) at 0.05C, with an ICE of 75.5% Figure 3-7(b). The large irreversible capacity resulted from the SEI formation on the HC anode. In contrast, when paired with the PreLi-30s HC anode, the 1st areal discharge capacity of the full cell was 0.92 mAh/cm^2 (cathode area), indicating a high ICE of 90.2%. In order to better demonstrate the advantage

of the prelithiation process, the capacity retention of the NMC 111 cathode was used. When cycled at a 1C rate, it delivered an initial discharge capacity of 0.76 mAh/cm^2 (cathode area) and maintained at 0.71 mAh/cm^2 (cathode area) after 200 cycles, with a high-capacity retention ratio of 93.4% Figure 3-7(c). For the pristine full cell, the discharge capacity after 200 cycles at 1C was 0.51 mAh/cm^2 (cathode area) with a capacity retention of 74%. To further exhibit the advantage of prelithiation, the utilization ratio of active Li ions in the cathode material (defined as the ratio of discharge capacity per cycle to the 1st charge capacity) is calculated. The utilization ratio at 1st cycle of prelithiated full cell is the same with an ICE of 90.2%. After the formation process and 200 cycles at 1C, the utilization ratio of active Li ions in the PreLi-30s full cell is 70%, higher than that of pristine full cell (46%).

The rate performance of the full cells is shown in Figure 3-8. With more active Li utilization from cathode, the PreLi-30s sample delivered a higher discharge capacity at 1C and 2C rate. When the calculation is based on the discharge capacity at respective 0.1C, the rate capability of the prelithiated and pristine samples are similar. Specifically, 87.7% for pristine and 85.5% for PreLi-30s were delivered at 1C, and 72.5% for pristine and 71% for PreLi-30s delivered at 2C. However, when the rate increased to 5C, the pristine sample exhibited a superior performance than the prelithiated sample (54.5% for the pristine vs. 43.1% for the PreLi-30s), which may be ascribed to the different SEI layer and thus resistance at higher rate, as will be discussed later in Figure 3-15. When the rate went back to 0.1C, the discharge capacity of prelithiated samples restored, indicating that the structure of prelithiated HC was not destroyed by the fast charging/discharging. The rate performance of

the half cells is shown in Figure 3-9. Similarly, the pristine sample exhibited a better performance than the prelithiated sample at high rate of 5C.

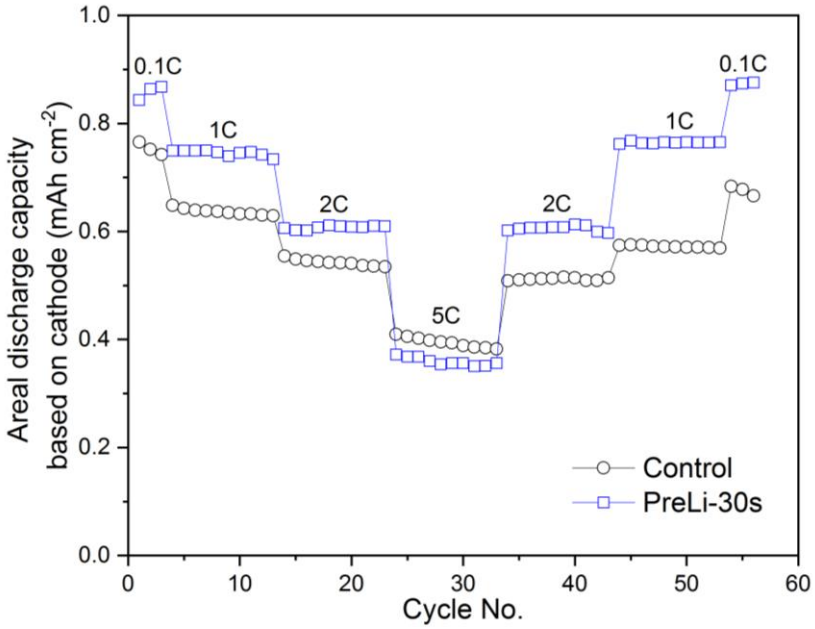

Figure 3-8. Rate capability of pristine and prelithiated HC electrodes in full cell format.

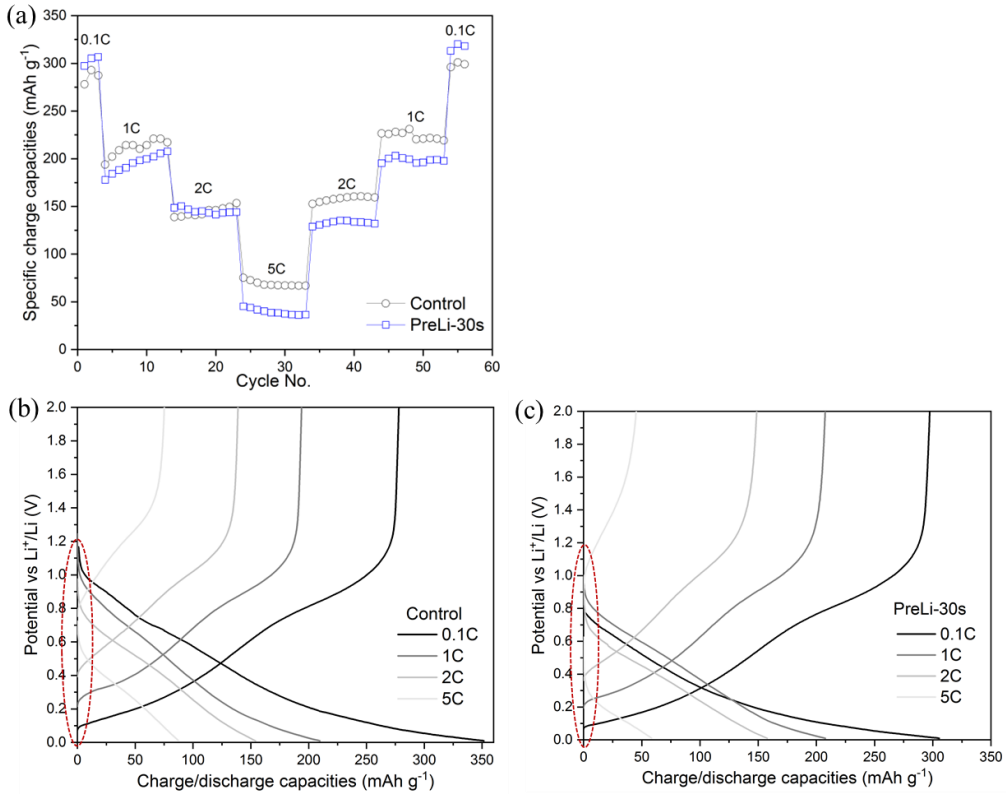

Figure 3-9. (a) Rate capability of pristine and prelithiated HC electrodes in half cell; (b) Charge/discharge curves of pristine HC electrodes at different rate; (c) Charge/discharge curves of PreLi-30s HC electrodes at different rate in half cell format.

The proposed prelithiation mechanism is illustrated in Figure 3-10. The addition of Li metal to aromatic hydrocarbons (Bp in this case) produces a Li-containing aromatic radical compound ($Li^+-Bp^{\cdot-}$), which has strong reducing ability as evidenced by the low redox potential of Bp/Li−Bp (~0.41 V vs Li^+/Li). Due to the high and slope lithiation voltage of hard carbon (0.2~1V), it can be reduced by Li−Bp, accompanied by the Li ions transferred from Li−Bp to hard carbon:

$$Li^+\text{-}Bp^- + C \rightarrow LiC + Bp$$

The key in this chemical prelithiation method is the lower redox potential of the Li-containing prelithiation reagent than the lithiation potential of anode materials. It should be noted that there were two distinct processes in the so-called prelithiation. One process forms the SEI layer on an anode, where reversible Li can also be intercalated into the matrix of the anode. After contact with the electrolyte, the preformed SEI was reconstructed. Complete formation of the SEI layer during chemical prelithiation is always beneficial, since less Li from a cathode would be irreversibly consumed in the formation of SEI layer during an electrochemical formation. However, unnecessary and excess Li could result in metallic Li plating during the subsequent cycles.

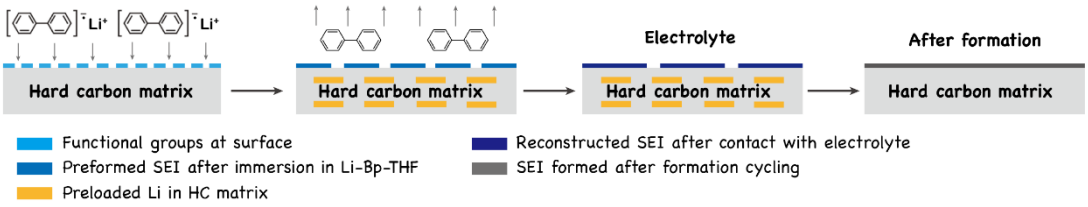

Figure 3-10. Proposed prelithiation mechanism of Li-Bp-THF in hard carbon.

Figure 3-11 – Figure 3-14 show results from surface analysis by XPS of the pristine and prelithiated HC electrodes with different prelithiation treatment time. Assignments of different components are based on the NIST XPS database and published research papers [89] – [92]. The C 1s and O 1s spectra of prelithiated electrodes after first delithiation and formation are similar to those of pristine electrodes after 1st cycling and formation respectively, while the F 1s spectra of the electrochemically cycled HC electrodes with and without chemical prelithiation are quite different, indicating that the prelithiation process has certain influence on the SEI composition of the HC anode. Specifically, apart from the PVDF binder component, the only source of F comes from the decomposition of $LiPF_6$. It is thus speculated that the chemical reaction of prelithiation reagent with PVDF binder and prelithiated HC with $LiPF_6$ lead to different SEI component on the surface of prelithiated HC. In Figure 3-11(a), a strong peak at 284.8 eV in the C 1s spectra of pristine HC was assigned to the sp2 C–C carbon in the graphene of the HC matrix. After first cycle and formation, the peak almost disappeared, indicating that the HC electrode was covered with the SEI layer from the decomposition of the electrolyte. The shift of the C, O, and F 1s spectra in the prelithiated electrodes before contacting with electrolyte supports the preformed SEI during prelithiation process. After contact with electrolyte, the XPS results of pristine electrode showed almost no change in the peak position. By contrast, a new peak of P 2p spectra appeared in the prelithiated electrodes shown in Figure 3-14, which indicated the decomposition of electrolyte and reconstruction of SEI. Generally, apart from the $–CF_2CH_2–$ binder component located at 688.3 eV [92], the components at ~685.2 eV and higher binding

energy of ~686.8 eV is assigned to inorganic lithium fluoride (LiF) and organic F-containing components, respectively [90], [91]. As we can see, more organic F-containing components and LiF are observed in the SEI of prelithiated samples, which may contribute to the improved cycling performance of full cells with prelithiated HC anodes [90].

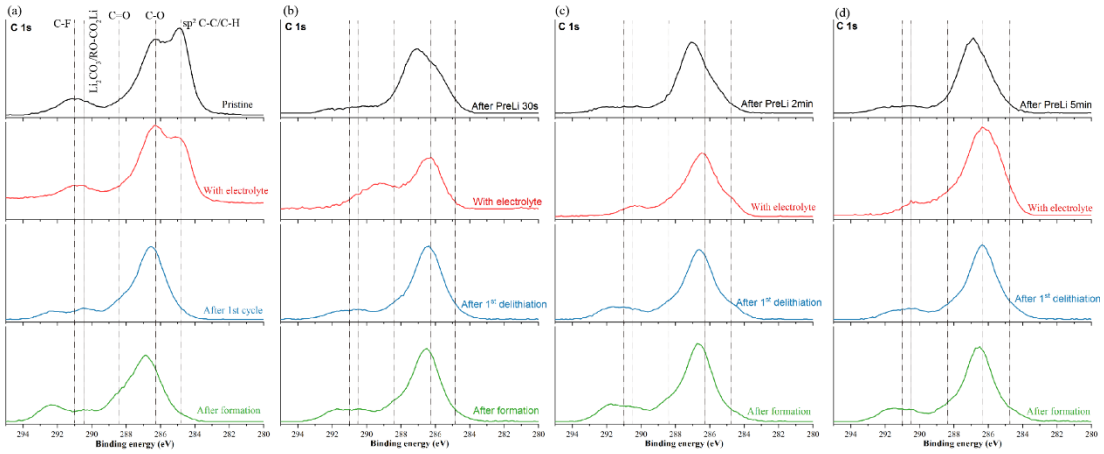

Figure 3-11. C 1s XPS spectra of pristine HC (a), PreLi-30s (b), PreLi-2min (c), and PreLi-5min (d) electrodes at different states.

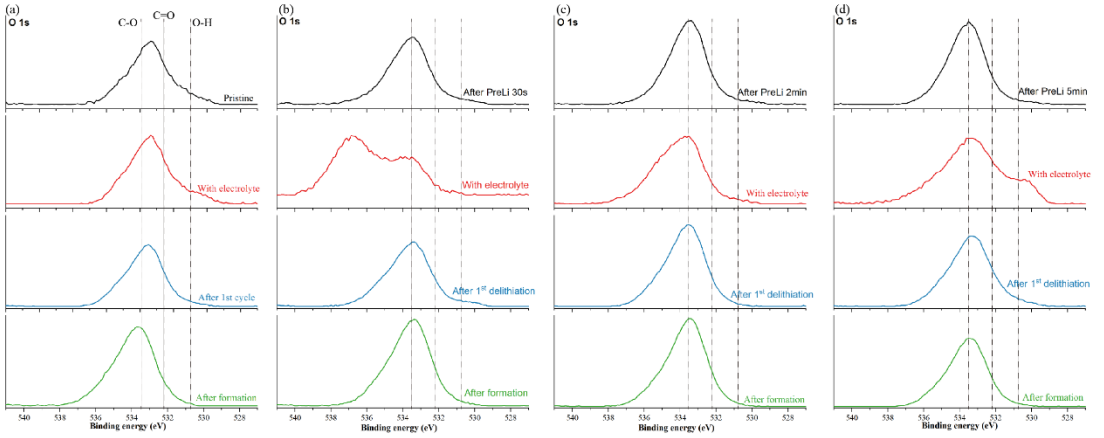

Figure 3-12. O 1s XPS spectra of pristine HC (a), PreLi-30s (b), PreLi-2min (c), and PreLi-5min (d) electrodes at different states.

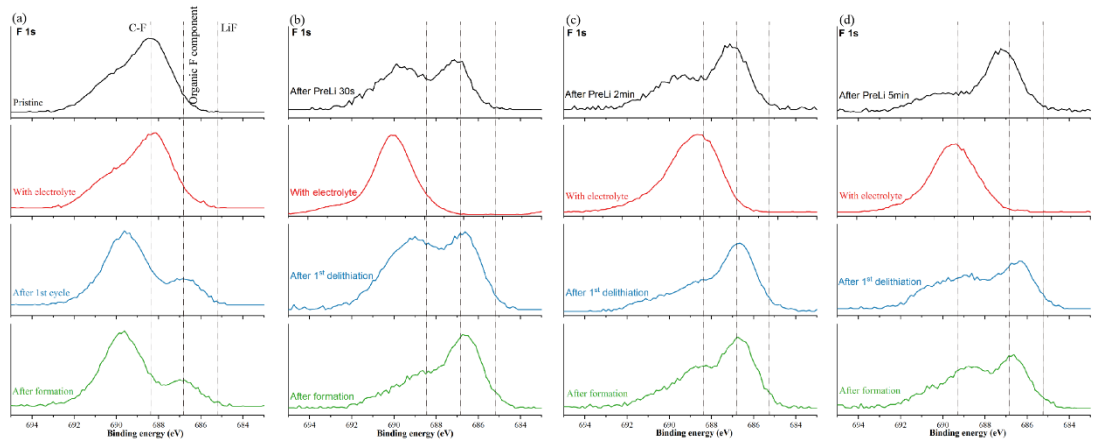

Figure 3-13. F 1s XPS spectra of pristine HC (a), PreLi-30s (b), PreLi-2min (c), and PreLi-5min (d) electrodes at different states.

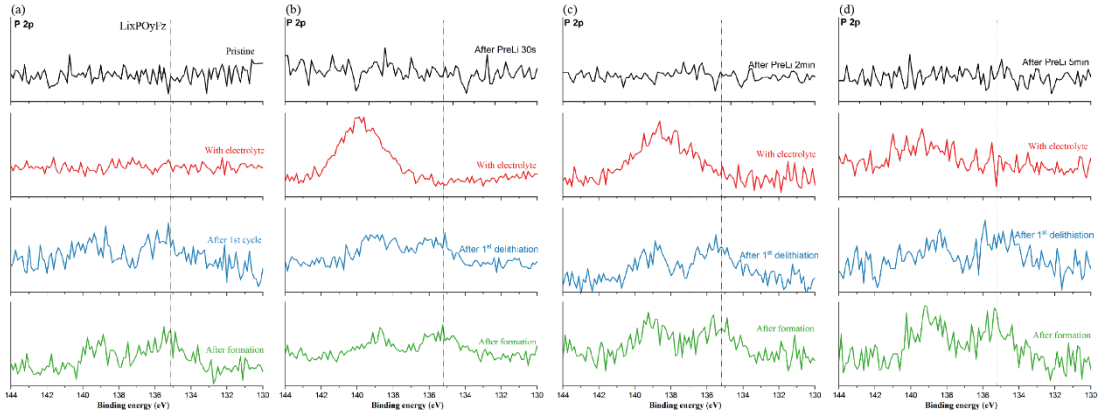

Figure 3-14. P 2p XPS spectra of pristine HC (a), PreLi-30s (b), PreLi-2min (c), and PreLi-5min (d) electrodes at different states.

Figure 3-15(a − c) show the CV curves of pristine HC electrodes in half cell construction. In the first cathodic scan, the cathodic current started from ~1.1 V and is assigned to the decomposition of the electrolyte components [93]. The following flat area from ~0.7 V is due to the Li ions insertion on the charge transferred surface sites. The sharp peak in the potential range of 0.01~0.3 V is usually ascribed to the Li ions intercalation into the graphite-like layers (0.15~0.3 V) and insertion into the cluster gap (0.01~0.15 V). In the reverse scan, the peaks located at ~0.25 and 0.8 V are related to the delithiation from the layers and gap, respectively [94]. In the subsequent cycles, the irreversible peak at ~1 V of the pristine electrode mainly results from the Li ions reaction with surface functional groups. By comparison, the prelithiated samples exhibit clearly reduced peaks, as shown in the dash square. Meanwhile, the flat area reflecting the charge transferred surface sites for Li ions insertion decreases with longer immersion time. The results indicate that the surface of prelithiated samples were reconstructed after the chemical prelithiation, which is consistent with the XPS results above.

An equivalent circuit is normally used to simulate the electrochemical process occurring in the cell. However, how to separate the contribution of individual process to the overall impedance remains a challenge, as different equivalent circuits can fit the same impedance curve. As it is presented in Chapter 2, in order to select the reasonable equivalent circuit to reflect the genuine processes, it is necessary to transfer the impedance in frequency domain into a distribution of the impedance in time domain, that is, the DRT [56], [95], [96]. It is based on the assumption that the impedance of an electrochemical system can be interpreted by a

universal transmission line model which consists of a continuous distribution of RC elements in the space of relaxation times. By analyzing the peaks in a DRT plot, the number of electrochemical processes can be predicted. In Figure 3-15(d − f), the three peaks in the DRT curves indicate three R/C (CPE) components in the equivalent circuit. The CPE is a constant phase element to simulate the distributed network of double layer capacitance and resistance in an inhomogeneous electrode and the deviation of CPE-P from 0.5 illustrates the deviation degree of the electrode surface from homogeneity. Before data analysis, all the data sets are subject to the Kramers–Kronig rule validation test [97]. Based on the possible reactions occurred in the cell, R_0 in the proposed circuit represents ohmic resistance of the electrolyte and the contact resistance in the cell; the first CPE_1/R_{ct1} component represents the capacitance and resistance of Li ions across the SEI layer; the second CPE_2/R_{ct2} and the last CPE_3/R_{ct3} components are used to simulate the possible side reactions between electrode and electrolyte and the capacitance and resistance of Li ions across the interface with the bulk electrode, respectively. The fitting results in Table 3-2 show that the R_1 value of prelithiated electrodes are higher than that of pristine electrodes and increases with increasing immersion time, which may be attributed to a thicker SEI formed with longer prelithiation time and leads to inferior rate capability. Meanwhile, the prelithiated electrodes exhibit much smaller values of R_2 and R_3 compared with pristine electrodes. It can be explained by the different SEI composition, that is, more organic F-containing component and LiF formed with chemical prelithiation is beneficial to the uniformity of SEI and thus cycling performance of full cells.

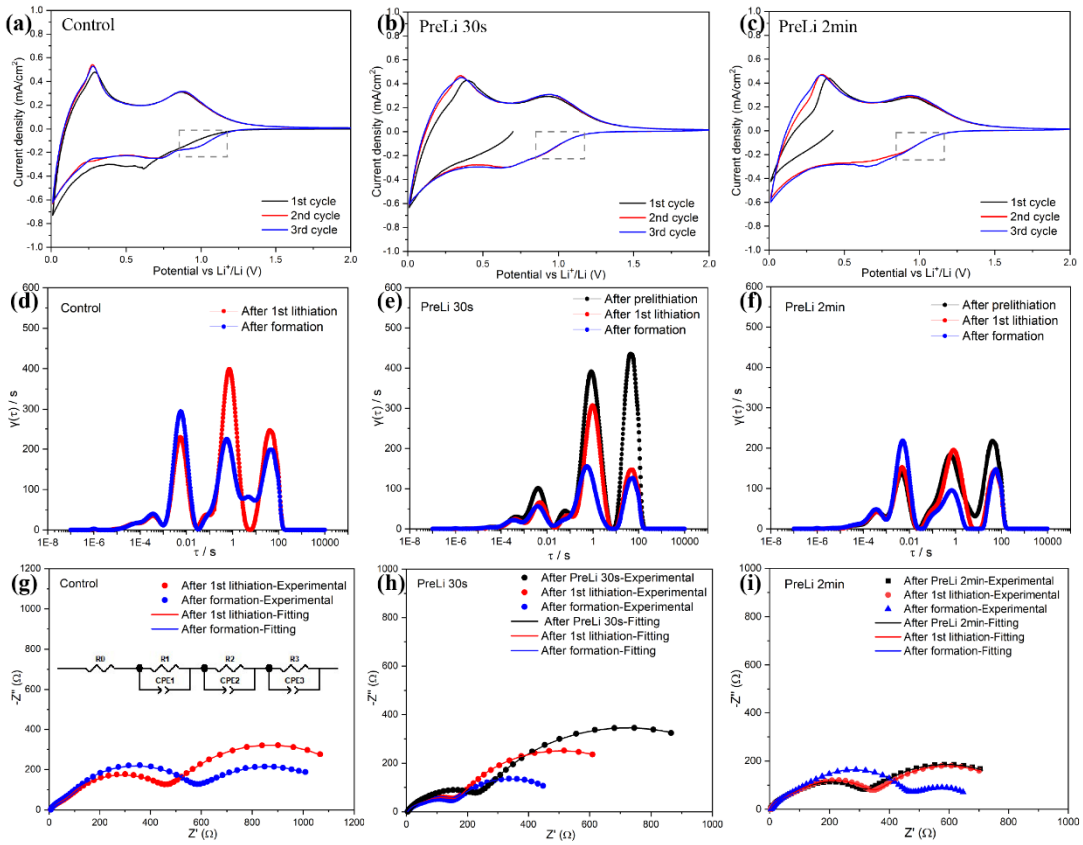

Figure 3-15. (a) CV curves of control, (b) PreLi-30s, (c) and PreLi-2min electrodes; (d) DRT plots of control, (e) PreLi-30s, (f) and PreLi-2min electrodes; (g) Nyquist plots of control, (h) PreLi-30s, (i) and PreLi-2min electrodes.

Table 3-2. Data summary of the EIS fitting results.

Sample	Status	R_0	R_1	CPE-T1	CPE-P1	R_2	CPE-T2	CPE-P2	R_3	CPE-T3	CPE-P3
Control	After 1st lithiation	5.877	55.09	1.36E-05	0.7931	421.3	3.15E-05	0.8234	795.4	0.00096	0.8529
	After formation	6.193	66.18	1.53E-05	0.7842	510.7	2.24E-05	0.8562	582.8	0.00134	0.7888
PreLi-30s	After PreLi for 30s	4.194	131.5	6.3E-05	0.7041	92.87	5.47E-05	0.9788	996.3	0.00096	0.7706
	After 1st lithiation	4.192	59.55	5.91E-05	0.7383	94.4	8.84E-05	0.8954	698.8	0.0014	0.7912
	After formation	3.518	82.01	8.21E-05	0.6829	61.49	8.94E-05	0.957	396	0.00159	0.7581
PreLi-2min	After PreLi for 2min	3.39	97.29	3.27E-05	0.728	210.4	3.66E-05	0.8818	568.9	0.00133	0.7285
	After 1st lithiation	3.637	89.05	2.61E-05	0.7443	250.7	3.57E-05	0.8639	512.8	0.00156	0.7677
	After formation	4.683	145.8	3.71E-05	0.6827	306.4	2.45E-05	0.9264	255.9	0.00255	0.746

3.2.3. Conclusions

Prelithiation method is effective to compensate for the initial loss of active Li ions and thus improve the reversible specific capacity of the cell. In this study, the chemical prelithiation reagent, Li-biphenyl-tetrahydrofuran, was evaluated for its prelithiation capability in hard carbon electrodes through the immersion method. The prelithiation depth can be tuned by immersion time. A short time of 30 s results in a high ICE of ~106% in half cell. When paired with NMC 111 cathode, the ICE of the full cell with prelithiated HC anode is increased to 90.2% compared with 75.5% of the pristine full cell. The cycling performance is improved as well, with a higher capacity retention of 93.4% after 200 cycles at 1C. The improvement is ascribed to the preformed SEI and reconstruction of the SEI with chemical prelithiation, where more organic F-containing components and LiF are formed. This fast and simple prelithiation method shows great potential in industrial application.

3.3. Prelithiation for silicon monoxide anode

Silicon is considered as a potential anode material for LIBs due to its higher theoretical capacity (3580 mAh/g) than that of graphite (372 mAh/g) [81] – [84]. However, Si undergoes a significant volume change (the expansion ratio of ~300%) during the lithiation and delithiation processes, which leads to cracking and pulverization of the active Si particles [85] – [88]. Consequently, the Si anode exhibits a severe capacity fading and low ICE, which limits its use in practical LIBs [98], [99], [106].

To overcome these obstacles, researchers studied various alternative Si-based materials,

including Si alloys (Si−M, where M = Sn, Ag, Zn, etc.) and Si composites with pure Si dispersed in a matrix (Si/C, SiO/C, etc.) [90] – [94]. The latter one, especially SiO/C material, shows much improved cycling performance with satisfactory specific capacity (1000~1400 $mAh/g_{composite}$) [10], [11]. It is generally accepted that the amorphous SiO is composed of metallic Si clusters finely dispersed in a SiO_2 matrix [112], [113]. During the first lithiation, the metallic Si is reduced to a $Li_{3.75}Si$ alloy, which is rechargeable during the subsequent cycles. Meanwhile, the amorphous SiO_2 is converted to lithium silicon oxides (Li_4SiO_4) with or without Li_2O, which play a buffer role to alleviate the volume change of the Si component and thus improve the cycling performance [114], [115]. However, the inherent irreversible formation of Li_4SiO_4 and Li_2O results in a low ICE (<80%); thus, only a small portion of SiO has been used (5~10 wt.%) with graphite in industry.

Lithium containing solution prelithiation is also the first choice to improve the ICE as well as the cycling capacity. Li-containing reagents with lower redox potentials are preferred as the average lithiation potential of the SiO anode is ~0.3 V.

From Figure 3-16, it can be seen the organolithium compound, Li−9,9-dimethyl-9H-fluorene (Flr) in THF has a pair of reversible redox peaks at 0.07 and 0.3 V (vs Li/Li^+), corresponding to a formal potential of 0.18 V. It is worth pointing out that since the reduction potential of Flr/Flr^- is so close to the Li deposition potential, the redox reactions of Flr/Flr^- and Li/Li^+ take place almost simultaneously. The small reduction plateau in the end of the reduction scan as shown in Figure 3-16 can be attributed to Li plating. Apparently, the redox potential of Flr/Flr^- was within the range of the lithiation potential of the SiO/G electrode

(0.02~0.4 V vs Li/Li^+). Li–Flr is a suitable reducing reagent to prelithiate the SiO/G electrode.

For the purpose of comparison, the redox potential of other organolithium compounds including Flr, Bp, naphthalene (Nap), and *n*-butyl reported for prelithiation are shown on the right of the CV curve. It was shown that the redox potentials of those organolithium compounds increased in the order of Li−Flr < Li−Bp < Li−Nap < Li−*n*-butyl. The different redox potentials have a direct impact on the selection of prelithiation reagents and prelithiation rate. The lower redox potential results of the shorter prelithiation time to reach a certain prelithiation depth. From the Figure, lower redox potential of ~0.2 V (vs Li/Li^+) which can theoretically prelithiate the SiO anode. To our best knowledge, this is the lowest redox potential value that has been reported so far for the organolithium compound for prelithiation.

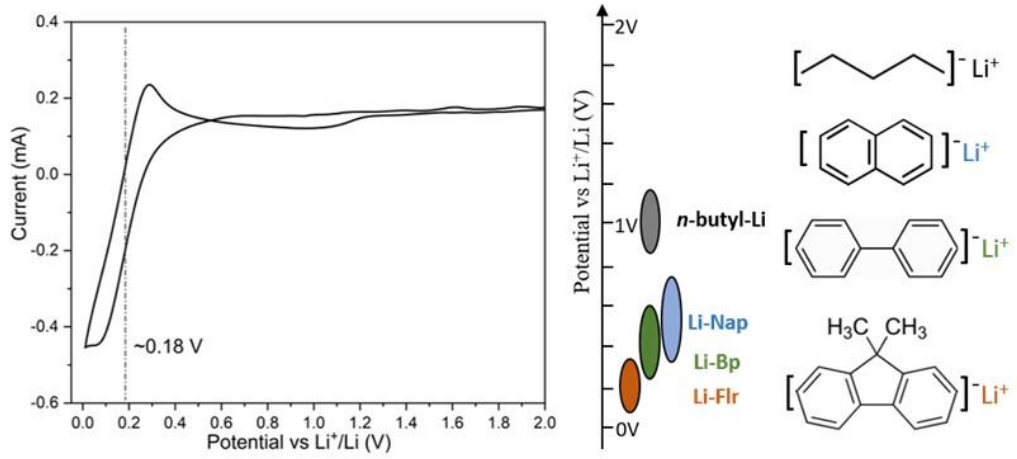

Figure 3-16. CV of Flr^{-}/Flr in 1 M $LiPF_6$ electrolyte (THF as solvent) at 10 mV/s (Right: Schematic illustration of redox potential and structure of Li−Flr, Li−Bp, Li−Nap, and Li−n-butyl prelithiation reagents)

3.3.1. Experiment details

Materials and characterization

A graphene coated SiO (SiO/G) anode and a NMC 622 cathode were provided by commercial sources. Bp, Nap, and THF were purchased from Sigma-Aldrich, and Flr from Tokyo Chemical Industry Co., Ltd. (TCI). All other chemicals were of analytical grade and were used as received. The morphology of the electrode was characterized using a Hitachi S-4800 field emission scanning electron microscope.

Prelithiation reagent preparation and electrode prelithiation

The prelithiation reagents (1.0 M Li−PAH−THF, where PAH = Flr, Bp, or Nap) were prepared as described in our previous reports [66], [116]. Specifically, a certain amount of Flr, Bp, and Nap was dissolved in THF to make a 1.0 M PAH−THF solution. Then, an excess amount of Li metal was added in the solution and reacted for 2 h to prepare a 1.0 M Li−PAH−THF solution. The addition of Li metal to a PAH solution produces a Li-containing aromatic radical compound, which has strong reducing ability. Once the Li metal was added, the solution turned to a dark blue-green color. The prelithiation reagents were prepared fresh before use.

A prelithiated SiO/G electrode was prepared by immersing the pristine SiO/G electrode into the prelithiation reagent for a predetermined duration, followed by washing with THF and drying to remove residual solvent. PAH-5min, PAH-10min, PAH-30min, and PAH-1h represented the SiO/G electrodes immersed in Li−PAH−THF solution for 5 min, 10 min, 30 min, and 1 h, respectively. The control sample is the SiO/G electrode without prelithiation

treatment.

Electrode fabrication and battery test

The formulation of the anode was SiO/G (mass ratio of 45:55), a carbon additive, and a binder in a mass ratio of 75:5:20. The typical electrode loading of the NMC 622 cathode, and the SiO/G anode was 18~19 mg/cm^2 and 3~4 mg/cm^2, respectively, and the areal rechargeable capacity of the NMC 622 cathode and the SiO/G anode was ~3 mAh/cm^2. The electrolyte was 1.0 M $LiPF_6$ dissolved in EC and EMC solvent (4:6 mass ratio), with 10 wt.% FEC and 2 wt.% VC as additives.

The electrochemical characterizations were carried out using 2032 coin cells assembled in an argon-filled glovebox (H_2O < 0.5 ppm, O_2 < 1 ppm). The Li-ion half-cell consisted of a Li metal anode, a Celgard 2325 separator, and the SiO/G or NMC 622 electrode. Galvanostatic charging/discharging tests were conducted on an Arbin battery testing system (BT2000) at room temperature. The voltage windows for SiO/G and NMC 622 half-cell tests were 0.02~1.5 and 2.5~4.3 V, respectively. In a full-cell assembly, the sizes of SiO/G and NMC electrodes were 5/8 and 9/16 inch ODs, respectively. The reversible capacity of negative-to-positive electrodes (N/P ratio) was 1.1~1.2. Following the formation cycles (C/20, C/10, and C/5 for cycles 1~3, followed by constant voltage charge until the current drops to C/20), the cells were cycled at 0.5C for another 100 cycles. For full-cell formation and cycling tests, the voltage window was 2.7~4.3 V and 3~4.3 V, respectively.

A three-electrode cell was used for the AC impedance measurement, in which Li foil and a Li ring were used as the counter electrode and reference electrode, respectively.

Measurements were conducted using an Autolab PGSTAT30 potentiostat/galvanostat electrochemical system (Metrohm). The frequency range was from 0.1 Hz to 10^6 Hz with a perturbation amplitude of 5 mV. The raw data were fitted using ZView software.

3.3.2. Results and discussions

The SEM image in Figure 3-17(a) shows the rock shaped SiO/G composite with an average size of ~2 μm. From Figure 3-17(b), when tested at 0.05C in a half-cell, the first lithiation and delithiation capacities of the control sample were 1504.7 and 1070.6 mAh/g, respectively, indicating a low ICE of only 71.2%. A voltage ‘‘dip’’ appeared at ~0.35 V during the first lithiation of the control sample, which was caused by the formation of a thick SEI together with volume expansion of SiO. A similar phenomenon was usually observed in the metal anode [117]. The CE of the second cycle of the control sample increased to about 97%, with a reversible capacity of 1034.2 mAh/g.

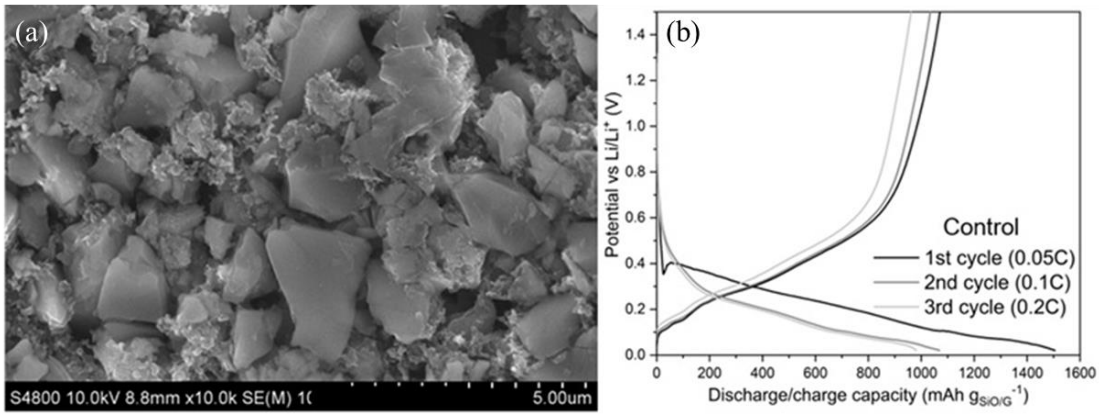

Figure 3-17. (a) SEM image of control electrode; (b) Formation process of control sample in half-cell format.

To verify the prelithiation effectiveness of reagents with lower potential value, a 1.0 M Li−Flr−THF, Li−Bp−THF, and Li−Nap−THF solution were prepared and used for SiO/G anode prelithiation. Figure 3-18(a, c, e) exhibit the first delithiation potential curves of all the prelithiated samples in half-cell format. It is worth emphasizing that during the prelithiation, the SEI forms first, followed by the insertion of reversible Li into SiO. To determine the reversible Li through prelithiation, unlike the pristine SiO electrodes, the prelithiated electrodes were oxidized (delithiated) first. The open circuit potential (OCP) of the prelithiated samples before delithiation was more negative than those of the control sample and decreased with increasing immersion time in each set of prelithiation experiments. The first delithiation capacity (reversible capacity) was inversely related to the OCP. With 10 min immersion time, the first delithiation capacity of the Nap-10min sample was negligible (< 10 mAh/g), indicating almost no reversible Li ions were prelithiated into the SiO/G anode. The first delithiation capacity of the Bp-10min and Flr-10min samples was ~40 and ~130 mAh/g, respectively, indicating that more reversible Li ions were chemically prelithiated into the SiO/G electrode with the same immersion time. The prelithiation effectiveness of the three reagents clearly increased in the order of Li−Nap−THF < Li−Bp−THF < Li−Flr−THF.

After the first delithiation, all the samples were subjected to the first lithiation and the second delithiation. As shown in Figure 3-18(b, d, f), the second delithiation capacities of all the samples are almost similar to that of the control sample (~1050 mAh/g). The first lithiation capacities after the first delithiation decreased as the increase of the immersion time for the SiO/G samples prelithiated with Nap and Bp, while the first lithiation capacities of

both Flr-5min and Flr-10 min are about 1200 mAh/g as shown in Figure 3-18(f). It is interesting to notice that the first lithiation capacity of Bp-1h is slightly higher than 1200 mA/g as shown in Figure 3-18(d). The coulombic efficiency (CE) (second delithiation to the first lithiation ratio) of all the prelithiated samples increased. The CE of Nap-1h, Bp-1h and Flr-10min were 82.9%, 85.8% and 87.1%, respectively. The OCP of the Flr-10min sample was ~0.47 V, and no obvious voltage “dip” was observed with further lithiation to 0.02 V.

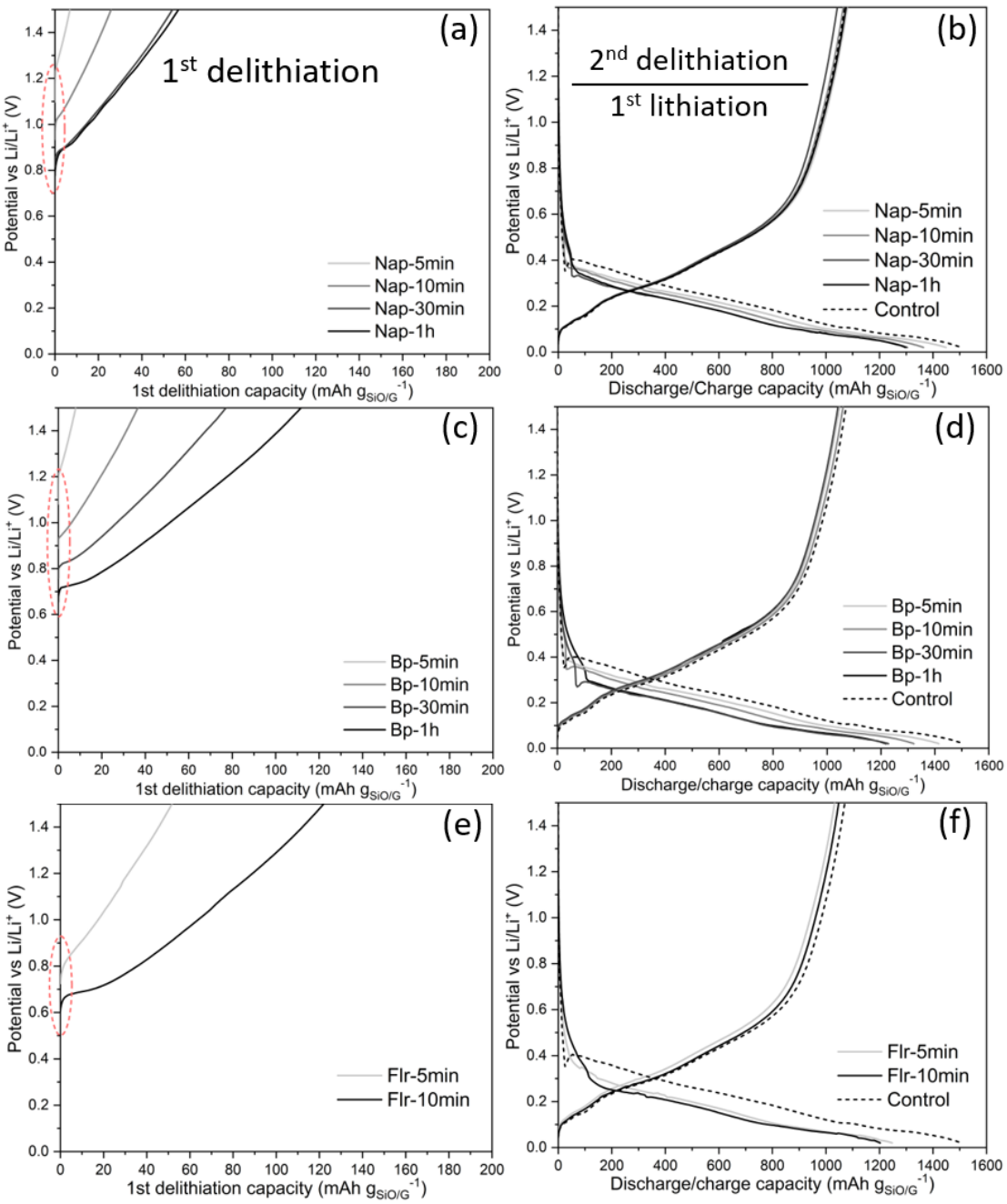

Figure 3-18. 1st delithiation and following lithiation/delithiation curves of SiO/G electrodes in half-cell format prelithiated using Li−Nap−THF (a, b), Li−Bp−THF (c, d), and Li−Flr−THF (e, f) with different immersion time. 1st lithiation/delithiation curves of control sample are shown in b, d, and f for comparison. The OCPs are circled with a dashedline in a, c and e.

Apparently, owing to their more positive redox potentials against Li, it not only took Nap and Bp a long time to form an SEI layer, but also the SEI layer formation was less complete. The slow forming and less complete SEI layer explained the progressive decrease of the first lithiation capacity as the prelithiation time increased, since some Li will be irreversibly consumed to build the incomplete SEI layer. However, a relatively complete SEI layer can be established with Li−Flr prelithiation. In addition, the volume expansion of SiO materials, the resulting pulverization and the formation of an SEI layer on the newly created surface during prelithiation all contributed to the consumption of Li during the subsequent electrochemical lithiation processes. It should be noted that the longer immersion time and the faster lithiation rate caused more deformation of SiO/G electrode due to the larger volume expansion. In this study, 10 min time was optimal for SiO/G electrode prelithiation using Li−Flr−THF reagent.

In the electrochemical formation of a Li-ion full cell, the cell is always charged first, then followed with discharge. In other words, unlike the prelithiated half-cell, the prelithiated SiO/G anode undergoes lithiation first. In order to determine the intrinsic capacity of the Flr-10min anode and the NMC 622 cathode, Figure 3-19 shows the half-cell results for Flr-10min and NMC 622. The full cell balance was determined based on the determined capacity. Figure 3-19(a) shown the first lithiation and subsequent first delithiation capacities of Flr-10min in a half-cell. The capacity was 1124.7 and 1018.7 mAh/g, respectively. The CE increased greatly to 90.6% compared with the control sample of 71.5%. Figure 3-19(b) shows the comparison of the cycling performance at 0.5C rate of the prelithiated samples and the control sample. No

obvious difference can be seen, and the reversible capacity was ~630 mAh/g and a high-capacity retention ratio of 97% after 100 cycles at 0.5C. The electrochemical results of the Flr-10min sample verified the positive impact of prelithiation on the reversible lithium consumption during the formation process and indicated that the prelithiation has little adverse impact on the reversible capacity and cycling performance.

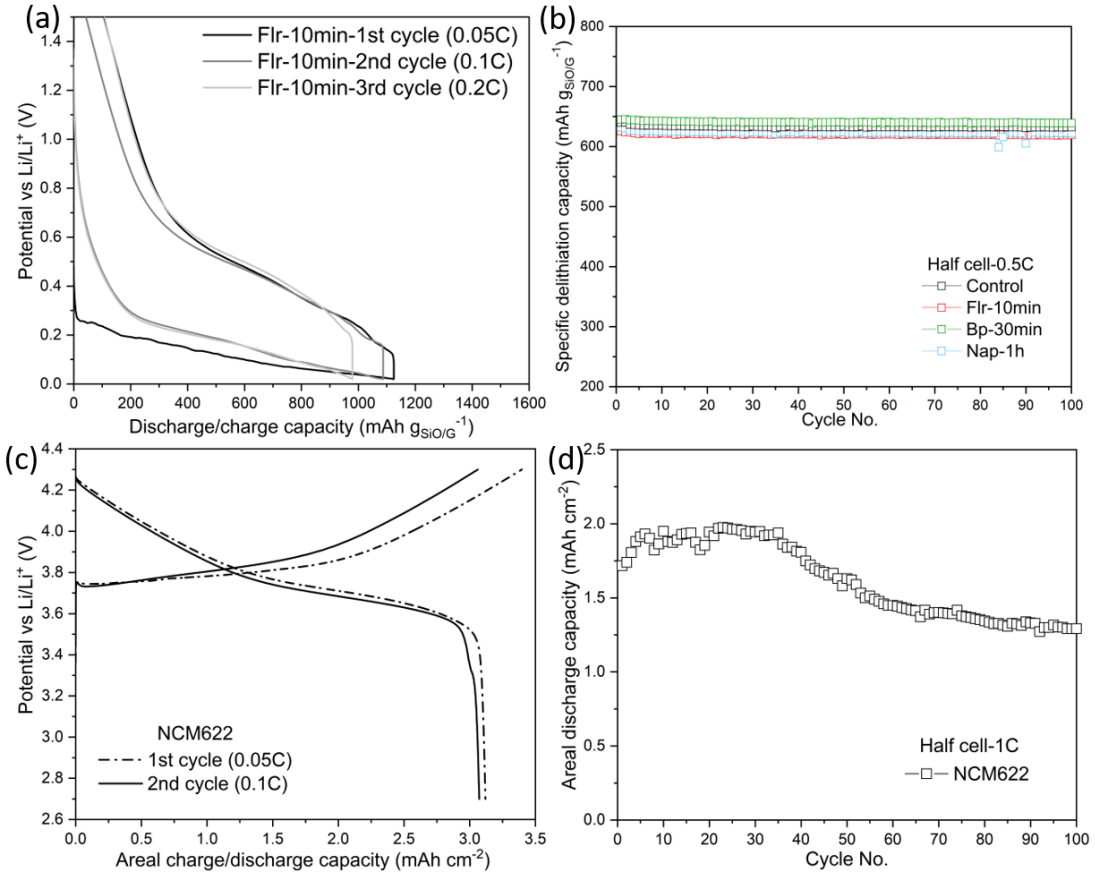

Figure 3-19. (a) Lithiation/delithiation curves of the cell made with Flr-10min half-cell during formation process; (b) Cycling performance of different samples at 0.5C in half-cell format; (c) 1st and 2nd cycles of NMC 622 electrode in half-cell format; (d) Cycling performance of NMC 622 electrode at 1C in half-cell format.

In a Li-ion full-cell, commercial NMC 622 cathodes were paired with the SiO/G anodes. Since there were different SEI completion and pre-loaded reversible Li in different SiO/G anodes, the cell balance was different. Therefore, the retention of cathode capacity is a better indicator than that of the cell capacity, since the NMC 622 cathode served as a control component in the experiment. At least it was a better indicator for cells that were not carefully optimized. Figure 3-19(c) shows that the intrinsic first areal charge and discharge capacities of the NMC 622 cathode were ~3.4 and ~3.1 mAh/cm^2, respectively. When cycled at 1C, the NMC 622 cathode exhibited a reversible discharge capacity of 1.75 mAh/cm^2 as shown in Figure 3-19(d). In the full cell paired with the control SiO/G anode, the initial areal charge capacity of 3.6 mAh/cm^2 and the discharge capacity of 2.2 mAh/cm^2 of the NMC 622 cathode at 0.05C are shown in Figure 3-20(a). The ICE was only 61.1%, indicating that almost 40% active Li in the cathode was consumed. The slightly higher charge capacity of the NMC 622 electrode in the full cell vs. that in the half-cell (3.6 vs. 3.4 mAh/cm^2) revealed that the NMC 622 cathode may be overcharged during the formation. This result was ascribed to the low ICE of the SiO/G anode and balancing of negative and positive active materials [118].

In contrast, as shown in Figure 3-20(a), when paired with the Flr-10min anode, the first areal charge capacity of the NMC 622 cathode is 3.4 mAh/cm^2 and the subsequent discharge capacity is about 3 mAh/cm^2, with a high ICE of 87.1%. When the Flr-5min anode was used as the anode, the first areal discharge capacity of the NMC 611 cathode was about 2.64 mAh/cm^2, and the ICE was 74.8%, as shown in Figure 3-20(b). It is clearly demonstrated that

adequate prelithiation can significantly increase retention of reversible Li from the cathode, and thus increase the overall cell capacity. Indeed, as shown in Figure 3-20(c), in the full-cell with the Flr-10min anode, the NMC 622 cathode delivered an initial discharge capacity of 2.27 mAh/cm^2 and maintained at 1.81 mAh/cm^2 after 100 cycles, while in the full cell with the pristine SiO/G anode, the discharge capacity of the NMC 622 cathode was only 1.38 mAh/cm^2 after 100 cycles. With less degree of prelithiation, the gain on the reversible capacity decreased. In the full-cell with the Flr-5min anode, the NMC 622 cathode delivered an initial discharge capacity of 1.89 mAh/cm^2 and maintained at 1.63 mAh/cm^2 after 100 cycles. The rate performance of the full-cells is shown in Figure 3-20(d). As the discharge rate increased, the cell impedance played a major role. When the rate returned to 0.1C, the discharge capacities of both samples restored to the previous level, indicating that the structure of prelithiated SiO/G was not changed in a fast charging and discharging.

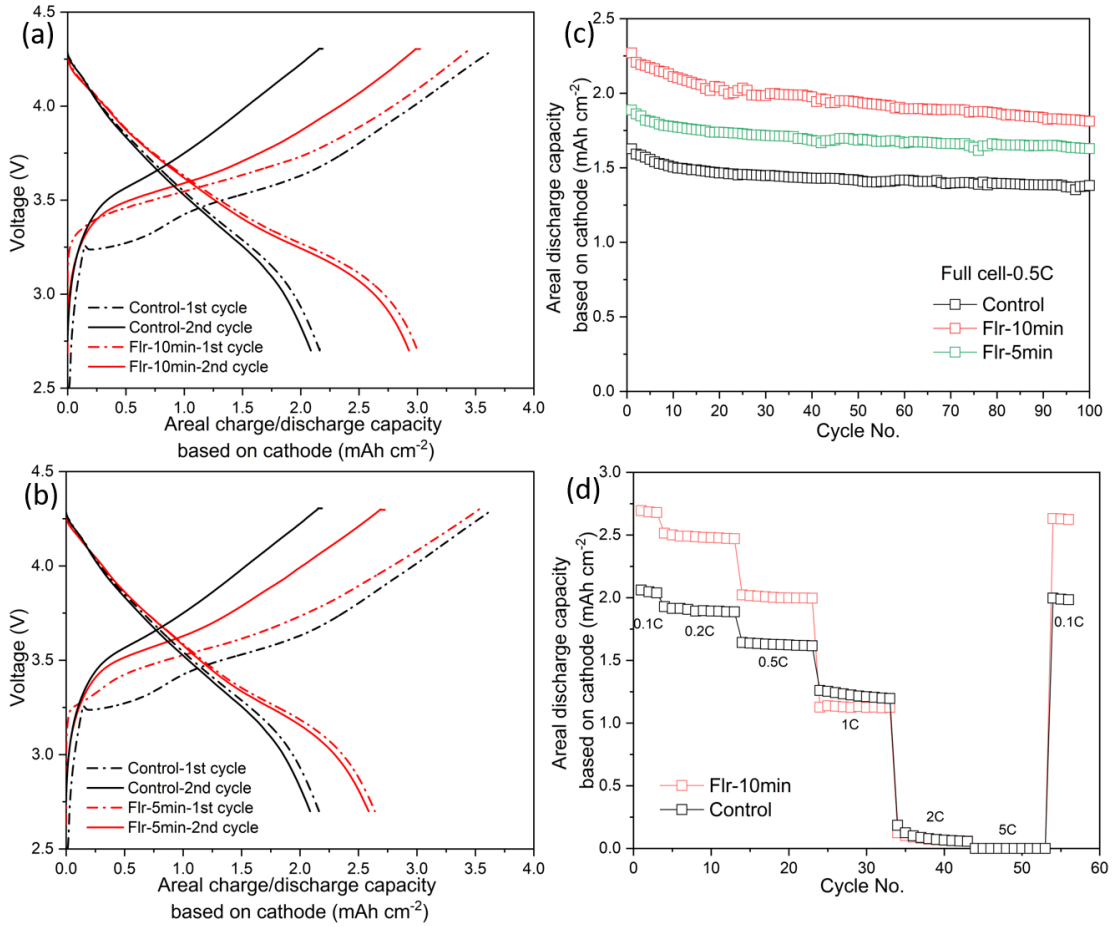

Figure 3-20. Li-ion full-cell tests. All cathodes are NMC 622. (a) 1st and 2nd charge/discharge voltage curves of control and Flr-10min anode in full-cells; (b) 1st and 2nd charge/discharge voltage curves of control and Flr-5min samples in full-cell format; (c) Cycling performance of control, Flr-5min, and Flr-10min samples at 0.5C in full-cell format; (d) Rate performance of control and Flr-10min samples in full-cell format.

In the analysis of EIS results, the DRT method calculated using a universal transmission line model offers direct determination of the number of electrochemical processes from the impedance spectrum. In Figure 3-21(b, d), the three main peaks in the DRT curves indicated three R/C (CPE) components in the equivalent circuit. Based on the possible reactions occurred in the cell, R_0 in the proposed circuit represents ohmic resistance of the electrolyte and the contact resistance; the first, second, and last R/CPE components simulate the capacitance and resistance of Li ions across the SEI layer, the capacitance and resistance of Li ions across the interface with the bulk electrode, and the diffusion of Li ions in the bulk, respectively. The fitting results in Table 3-3 showed that the R_1 value of the prelithiated electrode after rest was higher than that of before rest, which may be attributed to the pre-formation of SEI after contact with electrolyte. After lithiation to 0.02 V, the R_1 value of prelithiated electrode decreased, indicating a complete and better SEI formed electrochemically. The trend was also observed with the control electrode. The similar R_1 values of control and prelithiated electrodes demonstrated that the SEI formed by electrochemical lithiation is comparable with that formed by the combination of chemical and electrochemical lithiation.

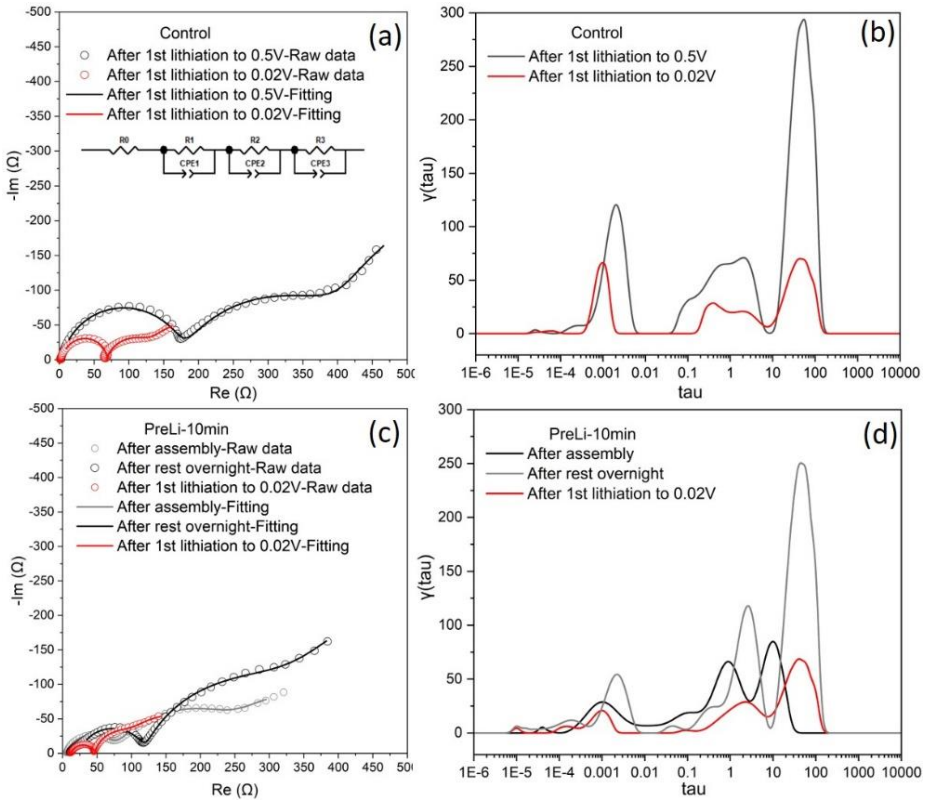

Figure 3-21. Nyquist and DRT plots of control (a, b) and Flr-10min samples (c, d).

Table 3-3. Data summary of the EIS fitting results.

Sample	Status	R_0	R_1	R_2	R_3
Control	**After 1st lithiation to 0.5V**	3.298	171.3	255.5	421
	After 1st lithiation to 0.02V	4.666	63.61	65.41	118.4
Flr-10min	**After assembly**	5.21	69.27	209.1	135.7
	After rest overnight	23.62	95.46	218.1	750
	After 1st lithiation to 0.02V	11.98	47.56	35.46	141

Based on the above results, the newly developed organolithium compound (Li–Flr–THF) can realize fast prelithiation of the SiO/G anode. The lower redox potential than that of Bp and Nap is related to its molecular structure, where the electron and Li ions are more easily transferred to reduce the SiO/G anode. The ICE of a Flr-10min sample in half and full cell formats were increased to 90.7% and 87.1%, respectively. The whole prelithiaiton process was described as: First, the SiO/G materials were chemically reduced by the Li-Flr reagent, transferring the Li ions into the SiO/G and formed $LiSi_xO_y/Li_2O$ and Li_xSi component. This corresponded to the irreversible reaction of Li ions with SiO_2 and reversible reaction with Si in electrochemical way, which effectively compensated for the lithium loss during the electrochemical formation process. Then, an incomplete SEI was formed after contact with electrolyte. Finally, a complete SEI was formed after further lithiation to lower potential electrochemically. We can conclusively state that the SEI formed on SiO/G through the prelithation was effective. However, because the ICE of the Flr-10min anode did not reach 100%, the SEI layer could go through restructuring during the electrochemical formation. We are in the process of investigating the difference between the SEI formed through prelithation, electrochemical formation and a hybrid. Of course, further investigation of the prelithiation impact on the cycling and rate performances is needed to optimize the prelithiation process.

3.3.3. Conclusions

In this study, a new chemical prelithiation reagent, Li−9,9-dimethyl-9H-fluorene−tetrahydrofuran, was reported to lithiate the SiO/G anode. Compared with other

prelithiation reagents, the lower potential of 9,9-dimethyl-9H-fluorene (~0.18 V) realized a faster prelithiation process, with a high ICE of ~90.7% in half-cell after 10 min prelithiation time. When paired with the NMC 622 cathode, the ICE of the full cell with the prelithiated SiO/G anode is increased to 87.1%, compared with 61.1% of the control full cell. A high-capacity retention of 80% was obtained after 100 cycles at 0.5C. The prelithiation process involved the irreversible reaction of Li with SiO_2 component in the matrix, as well as an incomplete SEI formation after contact with electrolyte, which are responsible for the improvement of ICE. This fast and simple prelithiation method for a SiO-based anode shows great potential in industrial application.

3.4. Summary

This chapter provided two examples of lithium containing solution prelithiation. By selecting the prelithiation regent with appropriate redox potential, HC and SiO anode were efficiently prelithiated. As a result, the ICE and the reversible capacity were significantly increased for both the anodes without losing the cycling stability.

In the future, the prelithiation with lithium containing solution method can be further optimized by varying the concentration of the reagent and the temperature of the reaction. Other than switching the aromatic hydrocarbon, the solvent of the prelithiation reagent also affects the redox potential, such as 2-methyltetrahydrofuran and dimethoxyethane. Those combinations provide more choices for prelithiating other electrode materials such as graphite, Si, SnO_2 and etc.

REFERENCES

[1] D. Linden, T. B. Reddy, *Handbook of batteries*, 3rd ed. New York: McGraw-Hill, 2002.

[2] "Electric vehicles," *Deloitte Insights*. [Online]. Available: https://www2.deloitte.com/us/en/insights/focus/future-of-mobility/electric-vehicle-trends-2030.html. [Accessed Jun. 29, 2022].

[3] X. Luo, J. Wang, M. Dooner, J. Clarke, "Overview of current development in electrical energy storage technologies and the application potential in power system operation," *Applied Energy*, vol. 137, pp. 511–536, 2015.

[4] J.-M. Tarascon, M. Armand, "Issues and challenges facing rechargeable lithium batteries," in *Materials for Sustainable Energy*, Co-Published with Macmillan Publishers Ltd, UK, 2010, pp. 171–179.

[5] S. Basu, C. Zeller, P. J. Flanders, C. D. Fuerst, W. D. Johnson, J. E. Fischer, "Synthesis and properties of lithium-graphite intercalation compounds," *Materials Science and Engineering*, vol. 38, no. 3, pp. 275–283, 1979.

[6] N. A. Godshall, I. D. Raistrick, R. A. Huggins, "Thermodynamic investigations of ternary lithium-transition metal-oxygen cathode materials," *Materials Research Bulletin*, vol. 15, no. 5, pp. 561–570, 1980.

[7] G. Zubi, R. Dufo-López, M. Carvalho, G. Pasaoglu, "The lithium-ion battery: State of the art and future perspectives," *Renewable and Sustainable Energy Reviews*, vol. 89, pp. 292–308, 2018.

[8] L.-F. Zhao, Z. Hu, W.-H. Lai, Y. Tao, J. Peng, Z.-C. Miao, Y.-X. Wang, S.-L. Chou, H.-K. Liu, S.-X. Dou, "Hard Carbon Anodes: Fundamental Understanding and Commercial Perspectives for Na-Ion Batteries beyond Li-Ion and K-Ion Counterparts," *Advanced Energy Materials*, vol. 11, no. 1, p. 2002704, 2021.

[9] G. G. Eshetu, E. Figgemeier, "Confronting the Challenges of Next-Generation Silicon Anode-Based Lithium-Ion Batteries: Role of Designer Electrolyte Additives and Polymeric Binders," *ChemSusChem*, vol. 12, no. 12, pp. 2515–2539, 2019.

[10] M. Yamada, K. Uchitomi, A. Ueda, K. Matsumoto, T. Ohzuku, "Performance of the 'SiO'–carbon composite-negative electrodes for high-capacity lithium-ion batteries; prototype 14500 batteries," *Journal of Power Sources*, vol. 225, pp. 221–225, 2013.

[11] Y. Hwa, C.-M. Park, H.-J. Sohn, "Modified SiO as a high performance anode for Li-ion batteries," *Journal of Power Sources*, vol. 222, pp. 129–134, 2013.

[12] S. Böhme, K. Edström, L. Nyholm, "Overlapping and rate controlling electrochemical reactions for tin(IV) oxide electrodes in lithium-ion batteries," *Journal of*

Electroanalytical Chemistry, vol. 797, pp. 47–60, 2017.

[13] Y. Ma, Y. Ma, G. Giuli, T. Diemant, R. J. Behm, D. Geiger, U. Kaiser, U. Ulissi, S. Passerini, D. Bresser, "Conversion/alloying lithium-ion anodes – enhancing the energy density by transition metal doping," *Sustainable Energy Fuels*, vol. 2, no. 12, pp. 2601–2608, 2018.

[14] L. Xie, C. Tang, Z. Bi, M. Song, Y. Fan, C. Yan, X. Li, F. Su, Q. Zhang, C. Chen, "Hard Carbon Anodes for Next-Generation Li-Ion Batteries: Review and Perspective," *Adv. Energy Mater.*, vol. 11, no. 38, p. 2101650, 2021.

[15] K. Xu, "Nonaqueous Liquid Electrolytes for Lithium-Based Rechargeable Batteries," *Chem. Rev.*, vol. 104, no. 10, pp. 4303–4418, 2004.

[16] G. J. Janz, *Nonaqueous electrolytes handbook*, vol. 1. Elsevier, 2012.

[17] M. Ue, "Mobility and Ionic Association of Lithium and Quaternary Ammonium Salts in Propylene Carbonate and γ-Butyrolactone," *J. Electrochem. Soc.*, vol. 141, no. 12, p. 3336, 1994.

[18] K. Naoi, M. Mori, Y. Naruoka, W. M. Lamanna, R. Atanasoski, "The Surface Film Formed on a Lithium Metal Electrode in a New Imide Electrolyte, Lithium Bis(perfluoroethylsulfonylimide) [LiN(C2F5SO2)2]," *J. Electrochem. Soc.*, vol. 146, no. 2, p. 462, 1999.

[19] H. Yang, K. Kwon, T. M. Devine, J. W. Evans, "Aluminum Corrosion in Lithium Batteries An Investigation Using the Electrochemical Quartz Crystal Microbalance," *J. Electrochem. Soc.*, vol. 147, no. 12, p. 4399, 2000.

[20] G. Pistoia, M. D. Rossi, B. Scrosati, "Study of the Behavior of Ethylene Carbonate as a Nonaqueous Battery Solvent," *J. Electrochem. Soc.*, vol. 117, no. 4, p. 500, 1970.

[21] R. Fong, U. von Sacken, J. R. Dahn, "Studies of Lithium Intercalation into Carbons Using Nonaqueous Electrochemical Cells," *J. Electrochem. Soc.*, vol. 137, no. 7, p. 2009, 1990.

[22] J. M. Tarascon, D. Guyomard, "New electrolyte compositions stable over the 0 to 5 V voltage range and compatible with the Li1+xMn2O4/carbon Li-ion cells," *Solid State Ionics*, vol. 69, no. 3, pp. 293–305, 1994.

[23] D. Aurbach, Y. Ein-Eli. B. Markovsky, A. Zaban, S. Luski, Y. Carmeli, H. Yamin, "The Study of Electrolyte Solutions Based on Ethylene and Diethyl Carbonates for Rechargeable Li Batteries: II . Graphite Electrodes," *J. Electrochem. Soc.*, vol. 142, no. 9, p. 2882, 1995.

[24] Y. Ein-Eli, S. R. Thomas, V. Koch, D. Aurbach, B. Markovsky, A. Schechter, "Ethylmethylcarbonate, a Promising Solvent for Li-Ion Rechargeable Batteries," *J. Electrochem. Soc.*, vol. 143, no. 12, p. L273, 1996.

[25] J. Kafle, J. Harris, J. Chang, J. Koshina, D. Boone, D. Qu, “Development of wide temperature electrolyte for graphite/ LiNiMnCoO2 Li-ion cells: High throughput screening,” *Journal of Power Sources*, vol. 392, pp. 60–68, 2018.

[26] Y. Matsuda, “Behavior of lithium/electrolyte interface in organic solutions,” *Journal of Power Sources*, vol. 43, no. 1, pp. 1–7, 1993.

[27] D. Xiong, J. C. Burns, A. J. Smith, N. Sinha, J. R. Dahn, “A High Precision Study of the Effect of Vinylene Carbonate (VC) Additive in Li/Graphite Cells,” *J. Electrochem. Soc.*, vol. 158, no. 12, p. A1431, 2011.

[28] N.-S. Choi, Y. Lee, S.-S. Kim, S.-C. Shin, Y.-M. Kang, “Improving the electrochemical properties of graphite/LiCoO2 cells in ionic liquid-containing electrolytes,” *Journal of Power Sources*, vol. 195, no. 8, pp. 2368–2371, 2010.

[29] H. Nakai, T. Kubota, A. Kita, A. Kawashima, “Investigation of the Solid Electrolyte Interphase Formed by Fluoroethylene Carbonate on Si Electrodes,” *J. Electrochem. Soc.*, vol. 158, no. 7, pp. A798–A801, 2011.

[30] K. Xu, S. Zhang, T. R. Jow, W. Xu, C. A. Angell, “LiBOB as Salt for Lithium-Ion Batteries:A Possible Solution for High Temperature Operation,” *Electrochem. Solid-State Lett.*, vol. 5, no. 1, p. A26, 2001.

[31] K. Xu, S. Zhang, B. A. Poese, T. R. Jow, “Lithium Bis(oxalato)borate Stabilizes Graphite Anode in Propylene Carbonate,” *Electrochem. Solid-State Lett.*, vol. 5, no. 11, p. A259, 2002.

[32] K. Xu, S. Zhang, T. R. Jow, “Formation of the Graphite/Electrolyte Interface by Lithium Bis(oxalato)borate,” *Electrochem. Solid-State Lett.*, vol. 6, no. 6, p. A117, 2003.

[33] M. Gauthier, T. J. Carney, A. Grimaud, L. Giordano, N. Pour, H.-H. Chang, D. P. Fenning, S. F. Lux, O. Paschos, C. Bauer, F. Maglia, S. Lupart, P. Lamp, Y. Shao-Horn, “Electrode–Electrolyte Interface in Li-Ion Batteries: Current Understanding and New Insights,” *J. Phys. Chem. Lett.*, vol. 6, no. 22, pp. 4653–4672, 2015.

[34] A. N. Dey, B. P. Sullivan, “The Electrochemical Decomposition of Propylene Carbonate on Graphite,” *J. Electrochem. Soc.*, vol. 117, no. 2, p. 222, 1970.

[35] E. Peled, “The Electrochemical Behavior of Alkali and Alkaline Earth Metals in Nonaqueous Battery Systems—The Solid Electrolyte Interphase Model,” *J. Electrochem. Soc.*, vol. 126, no. 12, p. 2047, 1979.

[36] J. O. Besenhard, M. Winter, J. Yang, W. Biberacher, “Filming mechanism of lithium-carbon anodes in organic and inorganic electrolytes,” *Journal of Power Sources*, vol. 54, no. 2, pp. 228–231, 1995.

[37] K. Kanamura, S. Shiraishi, Z. Takehara, “Electrochemical Deposition of Very Smooth Lithium Using Nonaqueous Electrolytes Containing HF,” *J. Electrochem. Soc.*, vol.

143, no. 7, p. 2187, 1996.

[38] E. Peled, D. Golodnitsky, G. Ardel, “Advanced Model for Solid Electrolyte Interphase Electrodes in Liquid and Polymer Electrolytes,” *J. Electrochem. Soc.*, vol. 144, no. 8, pp. L208–L210, 1997.

[39] K. Edström, M. Herstedt, D. P. Abraham, “A new look at the solid electrolyte interphase on graphite anodes in Li-ion batteries,” *Journal of Power Sources*, vol. 153, no. 2, pp. 380–384, 2006.

[40] S. Malmgren, K. Ciosek, M. Hahlin, T. Gustafsson, M. Gorgoi, H. Rensmo, K. Edström, “Comparing anode and cathode electrode/electrolyte interface composition and morphology using soft and hard X-ray photoelectron spectroscopy,” *Electrochimica Acta*, vol. 97, pp. 23–32, 2013.

[41] C. K. Chan, R. Ruffo, S. S. Hong, Y. Cui, “Surface chemistry and morphology of the solid electrolyte interphase on silicon nanowire lithium-ion battery anodes,” *Journal of Power Sources*, vol. 189, no. 2, pp. 1132–1140, 2009.

[42] Y.-C. Yen, S.-C. Chao, H.-C. Wu, N.-L. Wu, “Study on Solid-Electrolyte-Interphase of Si and C-Coated Si Electrodes in Lithium Cells,” *J. Electrochem. Soc.*, vol. 156, no. 2, p. A95, 2009.

[43] C. Pereira-Nabais, J. Światowska, A. Chagnes, A. Gohier, S. Zanna, A. Seyeux, P. Tran-Van, C.-S. Cojocaru, M. Cassir, P. Marcus, “Insight into the Solid Electrolyte Interphase on Si Nanowires in Lithium-Ion Battery: Chemical and Morphological Modifications upon Cycling,” *J. Phys. Chem. C*, vol. 118, no. 6, pp. 2919–2928, 2014.

[44] M. G. S. R. Thomas, P. G. Bruce, J. B. Goodenough, “AC Impedance Analysis of Polycrystalline Insertion Electrodes: Application to Li1 − x CoO2,” *J. Electrochem. Soc.*, vol. 132, no. 7, p. 1521, 1985.

[45] K. Edström, T. Gustafsson, J. O. Thomas, “The cathode–electrolyte interface in the Li-ion battery,” *Electrochimica Acta*, vol. 50, no. 2–3, pp. 397–403, 2004.

[46] J. F. Browning, L. Baggetto, K. L. Jungjohann, Y. Wang, W. E. Tenhaeff, J. K. Keum, D. L. Wood, III, G. M. Veith, “In Situ Determination of the Liquid/Solid Interface Thickness and Composition for the Li Ion Cathode LiMn $_{1.5}$ Ni $_{0.5}$ O $_{4}$,” *ACS Appl. Mater. Interfaces*, vol. 6, no. 21, pp. 18569–18576, 2014.

[47] G.-C. Chung, H.-J. Kim, S.-I. Yu, S.-H. Jun, J. Choi, M.-H. Kim, “Origin of Graphite Exfoliation An Investigation of the Important Role of Solvent Cointercalation,” *J. Electrochem. Soc.*, vol. 147, no. 12, p. 4391, 2000.

[48] D. Qu, G. Wang, J. Kafle, J. Harris, L. Crain, Z. Jin, D. Zheng, “Electrochemical Impedance and its Applications in Energy-Storage Systems,” *Small Methods*, vol. 2, no. 8, p. 1700342, 2018.

[49] H. Fricke, “XXXIII. The theory of electrolytic polarization,” *The London, Edinburgh,*

and Dublin Philosophical Magazine and Journal of Science, vol. 14, no. 90, pp. 310–318, 1932.

[50] T. Pajkossy, "Impedance of rough capacitive electrodes," *Journal of Electroanalytical Chemistry*, vol. 364, no. 1, pp. 111–125, 1994.

[51] J. R. Macdonald, E. Barsoukov, *Impedance Spectroscopy: Theory, Experiment, and Applications*. John Wiley & Sons, 2018.

[52] G. Nagasubramanian, "Two- and three-electrode impedance studies on 18650 Li-ion cells," *Journal of Power Sources*, vol. 87, no. 1, pp. 226–229, 2000.

[53] T. Osaka, T. Momma, D. Mukoyama, H. Nara, "Proposal of novel equivalent circuit for electrochemical impedance analysis of commercially available lithium ion battery," *Journal of Power Sources*, vol. 205, pp. 483–486, 2012.

[54] T. Momma, M. Matsunaga, D. Mukoyama, T. Osaka, "Ac impedance analysis of lithium ion battery under temperature control," *Journal of Power Sources*, vol. 216, pp. 304–307, 2012.

[55] M. Steinhauer, S. Risse, N. Wagner, K. A. Friedrich, "Investigation of the Solid Electrolyte Interphase Formation at Graphite Anodes in Lithium-Ion Batteries with Electrochemical Impedance Spectroscopy," *Electrochimica Acta*, vol. 228, pp. 652–658, 2017.

[56] H. Schichlein, A. C. Müller, M. Voigts, A. Krügel, E. Ivers-Tiffée, "Deconvolution of electrochemical impedance spectra for the identification of electrode reaction mechanisms in solid oxide fuel cells," *Journal of Applied Electrochemistry*, vol. 32, no. 8, pp. 875–882, 2002.

[57] P. Agarwal, M. E. Orazem, L. H. Garcia-Rubio, "Measurement Models for Electrochemical Impedance Spectroscopy: I . Demonstration of Applicability," *J. Electrochem. Soc.*, vol. 139, no. 7, p. 1917, 1992.

[58] R. M. Fuoss, J. G. Kirkwood, "Electrical Properties of Solids. VIII. Dipole Moments in Polyvinyl Chloride-Diphenyl Systems," *ACS Publications*, vol. 63, pp. 385–394, 1941.

[59] T. Feng, Y. Xu, Z. Zhang, X. Du, X. Sun, L. Xiong, R. Rodriguez, R. Holze, "Low-Cost Al_2O_3 Coating Layer As a Preformed SEI on Natural Graphite Powder To Improve Coulombic Efficiency and High-Rate Cycling Stability of Lithium-Ion Batteries," *ACS Appl. Mater. Interfaces*, vol. 8, no. 10, pp. 6512–6519, 2016.

[60] Y. He, X. Yu, Y. Wang, H. Li, X. Huang, "Alumina-Coated Patterned Amorphous Silicon as the Anode for a Lithium-Ion Battery with High Coulombic Efficiency," *Adv. Mater.*, vol. 23, no. 42, pp. 4938–4941, 2011.

[61] Y. Abe, T. Saito, S. Kumagai, "Effect of Prelithiation Process for Hard Carbon Negative Electrode on the Rate and Cycling Behaviors of Lithium-Ion Batteries,"

Batteries, vol. 4, no. 4, p. 71, 2018.

[62] F. Holtstiege, T. Koç, T. Hundehege, V. Siozios, M. Winter, T. Placke, "Toward High Power Batteries: Pre-lithiated Carbon Nanospheres as High Rate Anode Material for Lithium Ion Batteries," *ACS Appl. Energy Mater.*, vol. 1, no. 8, pp. 4321–4331, 2018.

[63] G. Ai, Z. Wang, H. Zhao, W. Mao, Y. Fu, R. Yi, Y. Gao, V. Battaglia, D. Wang, S. Lopatin, G. Liu, "Scalable process for application of stabilized lithium metal powder in Li-ion batteries," *Journal of Power Sources*, vol. 309, pp. 33–41, 2016.

[64] H. Sun, X. He, J. Li, J. Ren, C. Jiang, C. Wan, "Hard carbon/Li2.6Co0.4N composite anode materials for Li-ion batteries," *Solid State Ionics*, vol. 177, no. 15–16, pp. 1331–1334, 2006.

[65] J. Zhao, Z. Lu, N. Liu, H.-W. Lee, M. T. McDowell, Y. Cui, "Dry-air-stable lithium silicide–lithium oxide core–shell nanoparticles as high-capacity prelithiation reagents," *Nat Commun*, vol. 5, no. 1, p. 5088, 2014.

[66] G. Wang, F. Li, D. Liu, D. Zheng, C. J. Abeggien, Y. Luo, X.-Q. Yang, T. Ding, D. Qu, "High performance lithium-ion and lithium–sulfur batteries using prelithiated phosphorus/carbon composite anode," *Energy Storage Materials*, vol. 24, pp. 147–152, 2020.

[67] F. Li, G. Wang, D. Zheng, X. Zhang, C. J. Abegglen, H. Qu, D. Qu, "Controlled Prelithiation of SnO_2 /C Nanocomposite Anodes for Building Full Lithium-Ion Batteries," *ACS Appl. Mater. Interfaces*, vol. 12, no. 17, pp. 19423–19430, 2020.

[68] D. Aurbach, M. Moshkovich, Y. Cohen, A. Schechter, "The Study of Surface Film Formation on Noble-Metal Electrodes in Alkyl Carbonates/Li Salt Solutions, Using Simultaneous in Situ AFM, EQCM, FTIR, and EIS," *Langmuir*, vol. 15, no. 8, pp. 2947–2960, 1999.

[69] I. A. J. Gordon, S. Grugeon, H. Takenouti, B. Tribollet, M. Armand, C. Davoisne, A. Débart, S. Laruelle, "Electrochemical Impedance Spectroscopy response study of a commercial graphite-based negative electrode for Li-ion batteries as function of the cell state of charge and ageing," *Electrochimica Acta*, vol. 223, pp. 63–73, 2017.

[70] W. Waag, S. Käbitz, D. U. Sauer, "Experimental investigation of the lithium-ion battery impedance characteristic at various conditions and aging states and its influence on the application," *Applied Energy*, vol. 102, pp. 885–897, 2013.

[71] D. Andre, M. Meiler, K. Steiner, Ch. Wimmer, T. Soczka-Guth, D. U. Sauer, "Characterization of high-power lithium-ion batteries by electrochemical impedance spectroscopy. I. Experimental investigation," *Journal of Power Sources*, vol. 196, no. 12, pp. 5334–5341, 2011.

[72] J.-P. Jones, M. C. Smart, F. C. Krause, B. V. Ratnakumar, E. J. Brandon, "The Effect of Electrolyte Composition on Lithium Plating During Low Temperature Charging of

Li-Ion Cells," *ECS Trans.*, vol. 75, no. 21, p. 1, 2017.

[73] C. Bünzli, H. Kaiser, P. Novák, "Important Aspects for Reliable Electrochemical Impedance Spectroscopy Measurements of Li-Ion Battery Electrodes," *J. Electrochem. Soc.*, vol. 162, no. 1, p. A218, 2014.

[74] J. Costard, M. Ender, M. Weiss, E. Ivers-Tiffée, "Three-Electrode Setups for Lithium-Ion Batteries," *J. Electrochem. Soc.*, vol. 164, no. 2, p. A80, 2016.

[75] T. S. Ong, H. Yang, "Symmetrical Cell for Electrochemical AC Impedance Studies of Lithium Intercalation into Graphite," *Electrochem. Solid-State Lett.*, vol. 4, no. 7, p. A89, 2001.

[76] H. A. Kramers, "Die dispersion und absorption von röntgenstrahlen," *Phys. Z*, vol. 30, pp. 522–523, 1929.

[77] R. de L. Kronig, "On the Theory of Dispersion of X-Rays," *J. Opt. Soc. Am., JOSA*, vol. 12, no. 6, pp. 547–557, 1926.

[78] M. Urquidi-Macdonald, S. Real, D. D. Macdonald, "Applications of Kramers—Kronig transforms in the analysis of electrochemical impedance data—III. Stability and linearity," *Electrochimica Acta*, vol. 35, no. 10, pp. 1559–1566, 1990.

[79] P. Agarwal, M. E. Orazem, L. H. Garcia-Rubio, "The influence of error structure on interpretation of impedance spectra," *Electrochimica Acta*, vol. 41, no. 7, pp. 1017–1022, 1996.

[80] J. P. Schmidt, T. Chrobak, M. Ender, J. Illig, D. Klotz, E. Ivers-Tiffée, "Studies on LiFePO4 as cathode material using impedance spectroscopy," *Journal of Power Sources*, vol. 196, no. 12, pp. 5342–5348, 2011.

[81] L. Tan, L. Zhang, Q. Sun, M. Shen, Q. Qu, H. Zheng, "Capacity loss induced by lithium deposition at graphite anode for LiFePO4/graphite cell cycling at different temperatures," *Electrochimica Acta*, vol. 111, pp. 802–808, 2013.

[82] C. Wang, A. J. Appleby, F. E. Little, "Charge–discharge stability of graphite anodes for lithium-ion batteries," *Journal of Electroanalytical Chemistry*, vol. 497, no. 1, pp. 33–46, 2001.

[83] J. Yamaki, H. Takatsuji, T. Kawamura, M. Egashira, "Thermal stability of graphite anode with electrolyte in lithium-ion cells," *Solid State Ionics*, vol. 148, no. 3, pp. 241–245, 2002.

[84] F. Li, Y. Cao, W. Wu, G. Wang, D. Qu, "Prelithiation Bridges the Gap for Developing Next-Generation Lithium-Ion Batteries/Capacitors," *Small Methods*, vol. 6, no. 7, p. 2200411, 2022.

[85] M. Nagao, C. Pitteloud, T. Kamiyama, T. Otomo, K. Itoh, T. Fukunaga, K. Tatsumi, R. Kanno, "Structure Characterization and Lithiation Mechanism of Nongraphitized

Carbon for Lithium Secondary Batteries," *J. Electrochem. Soc.*, vol. 153, no. 5, p. A914, 2006.

[86] E. de la Llave, V. Borgel, E. Zinigrad, F.-F. Chesneau, P. Hartmann, Y.-K. Sun, D. Aurbach, "Study of the Most Relevant Aspects Related to Hard Carbons as Anode Materials for Na-ion Batteries, Compared with Li-ion Systems," *Israel Journal of Chemistry*, vol. 55, no. 11–12, pp. 1260–1274, 2015.

[87] W. Xing, J. R. Dahn, "Study of Irreversible Capacities for Li Insertion in Hard and Graphitic Carbons," *J. Electrochem. Soc.*, vol. 144, no. 4, p. 1195, 1997.

[88] E. Buiel, J. R. Dahn, "Li-insertion in hard carbon anode materials for Li-ion batteries," *Electrochimica Acta*, vol. 45, no. 1, pp. 121–130, 1999.

[89] C. Powell, "X-ray Photoelectron Spectroscopy Database XPS,Version 4.1, NIST Standard Reference Database 20." National Institute of Standards and Technology, 1989.

[90] R. Weber, M. Genovese, A. J. Louli, S. Hames, C. Martin, I. G. Hill, J. R. Dahn, "Long cycle life and dendrite-free lithium morphology in anode-free lithium pouch cells enabled by a dual-salt liquid electrolyte," *Nat Energy*, vol. 4, no. 8, Art. no. 8, 2019.

[91] W. E. Morgan, J. R. Van Wazer, W. J. Stec, "Inner-orbital photoelectron spectroscopy of the alkali metal halides, perchlorates, phosphates, and pyrophosphates," *J. Am. Chem. Soc.*, vol. 95, no. 3, pp. 751–755, 1973.

[92] D. T. Clark, W. J. Feast, D. Kilcast, W. K. R. Musgrave, "Applications of ESCA to polymer chemistry. III. Structures and bonding in homopolymers of ethylene and the fluoroethylenes and determination of the compositions of fluoro copolymers," *Journal of Polymer Science: Polymer Chemistry Edition*, vol. 11, no. 2, pp. 389–411, 1973.

[93] J. S. Gnanaraj, M. D. Levi, E. Levi, G. Salitra, D. Aurbach, J. E. Fischer, A. Claye, "Comparison Between the Electrochemical Behavior of Disordered Carbons and Graphite Electrodes in Connection with Their Structure," *J. Electrochem. Soc.*, vol. 148, no. 6, p. A525, 2001.

[94] I. Mochida, C.-H. Ku, Y. Korai, "Anodic performance and insertion mechanism of hard carbons prepared from synthetic isotropic pitches," *Carbon*, vol. 39, no. 3, pp. 399–410, 2001.

[95] B. A. Boukamp, "Fourier transform distribution function of relaxation times; application and limitations," *Electrochimica Acta*, vol. 154, pp. 35–46, 2015.

[96] J. P. Schmidt, P. Berg, M. Schönleber, A. Weber, E. Ivers-Tiffée, "The distribution of relaxation times as basis for generalized time-domain models for Li-ion batteries," *Journal of Power Sources*, vol. 221, pp. 70–77, 2013.

[97] B. A. Boukamp, "Electrochemical impedance spectroscopy in solid state ionics:

recent advances," *Solid State Ionics*, vol. 169, no. 1, pp. 65–73, 2004.

[98] M. N. Obrovac, V. L. Chevrier, "Alloy Negative Electrodes for Li-Ion Batteries," *Chemical Reviews*, vol. 114, no. 23, pp. 11444–11502, 2014.

[99] F. Luo, B. Liu, J. Zheng, G. Chu, K. Zhong, H. Li, X. Huang, L. Chen, "Review—Nano-Silicon/Carbon Composite Anode Materials Towards Practical Application for Next Generation Li-Ion Batteries," *Journal of The Electrochemical Society*, vol. 162, no. 14, pp. A2509–A2528, 2015.

[100] T. D. Hatchard, J. R. Dahn, "In Situ XRD and Electrochemical Study of the Reaction of Lithium with Amorphous Silicon," *Journal of The Electrochemical Society*, vol. 151, no. 6, pp. A838–A842, 2004.

[101] M. N. Obrovac, L. Christensen, "Structural changes in silicon anodes during lithium insertion/extraction," *Electrochemical and Solid-State Letters*, vol. 7, no. 5, pp. A93–A96, 2004.

[102] L. Y. Beaulieu, T. D. Hatchard, A. Bonakdarpour, M. D. Fleischauer, J. R. Dahn, "Reaction of Li with Alloy Thin Films Studied by In Situ AFM," *Journal of The Electrochemical Society*, vol. 150, no. 11, pp. A1457–A1464, 2003.

[103] Y. H. Wang, Y. He, R. J. Xiao, H. Li, K. E. Aifantis, X. J. Huang, "Investigation of crack patterns and cyclic performance of Ti-Si nanocomposite thin film anodes for lithium ion batteries," *Journal of Power Sources*, vol. 202, pp. 236–245, 2012.

[104] Y. Wang, Y. Liu, J. Zheng, H. Zheng, Z. Mei, X. Du, H. Li "Electrochemical performances and volume variation of nano-textured silicon thin films as anodes for lithium-ion batteries," *Nanotechnology*, vol. 24, no. 42, p. 424011, 2013.

[105] M. T. McDowell, S. W. Lee, W. D. Nix, Y. Cui, "25th anniversary article: Understanding the lithiation of silicon and other alloying anodes for lithium-ion batteries," *Advanced Materials*, vol. 25, no. 36, pp. 4966–4985, 2013.

[106] Y. Oumellal, N. Delpuech, D. Mazouzi, N. Dupré, J. Gaubicher, P. Moreau, P. Soudan, B. Lestriez, D. Guyomard, "The failure mechanism of nano-sized Si-based negative electrodes for lithium ion batteries," *Journal of Materials Chemistry*, vol. 21, no. 17, pp. 6201–6208, 2011.

[107] T. D. Hatchard, J. R. Dahn, S. Trussler, M. Fleischauer, A. Bonakdarpour, J. R. Mueller-Neuhaus, K. C. Hewitt, "The amorphous range in sputtered Si-Al-Sn films," *Thin Solid Films*, vol. 443, no. 1–2, pp. 144–150, 2003.

[108] M. D. Fleischauer, J. R. Dahn, "Combinatorial Investigations of the Si-Al-Mn System for Li-Ion Battery Applications," *Journal of The Electrochemical Society*, vol. 151, no. 8, pp. A1216–A1221, 2004.

[109] M. D. Fleischauer, M. N. Obrovac, J. R. Dahn, "Simple Model for the Capacity of Amorphous Silicon-Aluminum-Transition Metal Negative Electrode Materials,"

Journal of The Electrochemical Society, vol. 153, no. 6, pp. A1201–A1205, 2006.

[110] T. D. Hatchard, M. N. Obrovac, J. R. Dahn, "A Comparison of the Reactions of the SiSn, SiAg, and SiZn Binary Systems with L3i," *Journal of The Electrochemical Society*, vol. 153, no. 2, p. A282, 2006.

[111] B. Liu, A. Abouimrane, Y. Ren, M. Balasubramanian, D. Wang, Z. Z. Fang, K. Amine, "New anode material based on SiO-SnxCoyCz for lithium batteries," *Chemistry of Materials*, vol. 24, no. 24, pp. 4653–4661, 2012.

[112] T. Kim, S. Park, S. M. Oh, "Solid-State NMR and Electrochemical Dilatometry Study on Li + Uptake/Extraction Mechanism in SiO Electrode," *J. Electrochem. Soc.*, vol. 154, no. 12, p. A1112, 2007.

[113] S. C. Jung, H.-J. Kim, J.-H. Kim, Y.-K. Han, "Atomic-Level Understanding toward a High-Capacity and High-Power Silicon Oxide (SiO) Material," *J. Phys. Chem. C*, vol. 120, no. 2, pp. 886–892, 2016.

[114] M. A. Al-Maghrabi, J. Suzuki, R. J. Sanderson, V. L. Chevrier, R. A. Dunlap, J. R. Dahn, "Combinatorial Studies of Si1−xOx as a Potential Negative Electrode Material for Li-Ion Battery Applications," *J. Electrochem. Soc.*, vol. 160, no. 9, p. A1587, 2013.

[115] M. Yamada, A. Inaba, A. Ueda, K. Matsumoto, T. Iwasaki, T. Ohzuku, "Reaction Mechanism of 'SiO'-Carbon Composite-Negative Electrode for High-Capacity Lithium-Ion Batteries," *J. Electrochem. Soc.*, vol. 159, no. 10, p. A1630, 2012.

[116] G. Wang, F. Li, D. Liu, D. Zheng, Y. Luo, D. Qu, T. Ding, D. Qu, "Chemical Prelithiation of Negative Electrodes in Ambient Air for Advanced Lithium-Ion Batteries," *ACS Appl. Mater. Interfaces*, vol. 11, no. 9, pp. 8699–8703, 2019.

[117] D. Qu, "The cause of the voltage 'dip' during the high rate discharge of the primary alkaline MnO2/Zn cells," *Electrochemistry Communications*, vol. 8, no. 9, pp. 1527–1530, 2006.

[118] J. Kasnatscheew, T. Placke, B. Streipert, S. Rothermel, R. Wagner, P. Meister, I. C. Laskovic, M. Winter, "A Tutorial into Practical Capacity and Mass Balancing of Lithium Ion Batteries," *Journal of The Electrochemical Society*, vol. 164, no. 12, pp. A2479–A2486, 2017.